

**Physical and Mathematical Modelling of Sources of Inclusions in a
Tundish for Steel Powder Atomization Operation**

By

Daniel Ricardo Gonzalez Morales

Department of Mining and Material Engineering

McGill University, Montreal

2022

A thesis submitted to McGill University in partial fulfillment of the
requirements of the degree of M.Sc.

Contents

Figures Index	4
List of abbreviations	9
Abstract.....	10
Acknowledgements.....	12
Introduction.....	13
Chapter 1 Literature Review	14
1.1- Inclusions in steels	14
1.2.- Inclusions ‘control	18
1.3.- “Tundish Metallurgy” Literature review	21
1.3.1 Tundish mathematical modelling review of the last 5 years	28
1.4.- Ladle Shroud; an important Tundish flow control device.	43
1.4.1. Ladle Shroud mathematical and physical modelling; a review of the last 5 years.....	46
Chapter 2: Methodology	54
2.1 Mathematical modelling.....	54
2.1.1 Geometry generation	55
2.1.2 Meshing	61
2.1.3 Governing Equations	63
2.1.4 Operating conditions.....	65
2.1.5 ANSYS Fluent© Solution	66
2.1.6 Cases descriptions.....	67
2.1.7 Simplified Case.....	68
2.1.8 Air Suction Case.....	71
2.1.9 Real Case	74
2.2 Physical Modelling.....	77

2.2.1 Real dimensions and details	78
2.2.2 Construction of the full-scale Ladle Shroud system for water modelling research.....	81
2.2.4 Visualization of the filling stage in the water model.....	86
Chapter 3: Results and Discussion.....	89
3.1 Mathematical Modelling Results	89
3.1.1 Simplified case	89
3.1.2 Air suction case	96
3.1.3 Real case	99
3.2 Physical Modelling results	108
Conclusions.....	114
Future Work.....	115
Bibliography	115

Figures Index

Figure 1. Sources of non-metallic inclusions in Steelmaking [5].....	14
Figure 2. Different types of inclusions after Hot Rolling; A1: Al ₂ O ₃ inclusions; A2: Al ₂ O ₃ inclusions cluster; TI1 & TI2: TiO ₂ inclusions; SI1: SiO ₂ inclusions; M1: MnO inclusions. [6]	15
Figure 3. Inclusion-Crack initiation during Hot rolling [7]......	16
Figure 4. Inclusion-physical removing in Tundish [8].	18
Figure 5. Inclusions Chemical Control: A) Silicon Addition to decrease sol. [O] in liquid steel; B) Si-Mn killed steel with slag composition (Right) control in Ladle to promote specific inclusions composition (Left) with low melting point to avoid nozzle clogging [1]......	19
Figure 6. Continuous casting system for SULC Steels with methods for NMI control. Taken from [9]......	20
Figure 7. Summary of Tundish transient and steady state operations [12]......	25
Figure 8. Advancement of the AIM in Tundish mathematical modelling research [12].	27
Figure 9. Tundish with a strong paralleling flow near the surface with weir and dam. Inclusions' trajectories and deposition velocities calculated by Chen et al. [13]......	29
Figure 10. Tundish with gas curtain near the inlet, directing the inclusions towards the surface to be removed. Inclusions' trajectories calculated by Aguilar-Rodriguez et al. [16].	30
Figure 11. Slag phase volume fraction contours at different times with high argon flow rate injection predicted by Chatterjee et al. [17]......	31
Figure 12. Inclusions' (30 μm) trajectories (a) without gas curtain and (b) with gas curtain predicted by de Souza et al. [21]......	33
Figure 13. Bubbles distribution on a Tundish surface. Left 0.5 mm, right 5.0 mm. obtained by Chang et al. [22]......	34
Figure 14. Wall shear stress contours on the tundish walls, (top) without a TIB, (bottom) with an inward draft TIB predicted by Gupta et al. [25].	36
Figure 15. Case 1) Tundish with traditional turbulence inhibitor. Case 2) Tundish with swirling flow system. Taken from [27]......	37
Figure 16. 20 μm particles contours maps on different planes and at different times for different models calculated by Merder et al. [28]......	38
Figure 17. 20 μm particles contours for different mathematical models and the water model at different times (a) 25, (b) 60 and (c) 120 seconds, calculated by Merder et al. [28]].	39

Figure 18. Slag (green) and air (blue) phase distributions at (a) 0.5, (b) 2, (c) 5, and 15 seconds calculated by Xu et al. [30].	40
Figure 19. Schematic of the ladle-LS-Tundish system. Taken from [31].	44
Figure 20. (a) Crevices between lower nozzle and LS. (b) Methods for effective shrouding. Taken and adapted from [31].	45
Figure 21. LS shroud designs. A) CLS. B) TLS type 1. C) TLS type II	45
Figure 22. (a) Geometry configuration and boundary conditions. (b) Flow characteristics observed in water modelling. (c) Flow characteristics in mathematical modelling. Taken and adapted from [33].	47
Figure 23. Velocity profiles for (a) conventional LS and (b) DLS predicted by Zhang et al. [34].	48
Figure 24. Full-scale Ladle Shroud water model for system for (a) bloom casting, (b) slab casting and (c) schematic of the bloom casting system. Taken from [35].	49
Figure 25. Two-phase flow regimes observed a different gas to liquid flow ratios, (a) $Q_g/Q_l=0.02$, bubbly regime, (b) $Q_g/Q_l=0.3$ partial free liquid jet and (c) $Q_g/Q_l=0.42$, complete free liquid jet. Taken from [35].	50
Figure 26. Two phase flows within a Ladle Shroud in (a) a full-scale water model and (b) its corresponding predicted gas volume fraction with $Q_g/Q_l=0.025$; (c) a full-scale water model and (d) its corresponding predicted gas volume fraction with $Q_g/Q_l=0.2$. Taken from [36].	51
Figure 27. Turbulence kinetic energy contours for 3 different Ladle Shrouds designs obtained by Zhang et al. [37].	52
Figure 28. Air volume fraction contour (light blue) during ladle-change over for (a) LS1, (b) LS2, exiting diameter= $1.5 \cdot D_{LS1}$ and (c) LS3, exiting diameter= $2 \cdot D_{LS1}$ obtained by Zhang et al. [37].	53
Figure 29. Process followed for the mathematical modelling	55
Figure 30. Tundish geometry generated in SpaceClaim©. Side view.	55
Figure 31. Tundish geometry generated in SpaceClaim©. Top view.	56
Figure 32. Tundish geometry generated in SpaceClaim©. Isometric view.	56
Figure 33. Ladle Shroud geometry generated in SpaceClaim©.	57
Figure 34. Turnflow geometry generated in SpaceClaim©. Side and Top view.	58
Figure 35. Anti-vortex nozzle geometry generated in SpaceClaim©.	58

Figure 36. Position of the ladle shroud, turnflow and anti-vortex nozzles within the Tundish....	59
Figure 37. Final volume generated of the Ladle Shroud-Tundish system in SpaceClaim©.	59
Figure 38. (a) Ladle Shroud geometry with simplified entry zone; (b) Ladle Shroud geometry without argon injection and 1.2 mm gap; (c) Ladle Shroud geometry with slide gate and actual Tundish entry zone with turnflow walls.	60
Figure 39. Ladle-Tundish system geometry generated in SpaceCalim© and details for the water model construction.....	61
Figure 40. Mesh example with elements refinement examples generated in ANSYS Mesh ©. ..	62
Figure 41. Skewness metric histogram for the Figure 40 mesh.....	62
Figure 42. ANSYS Fluent v19.0 set up tab.	67
Figure 43. Summary of the case descriptions	68
Figure 44. Geometry and Boundary Conditions for the Simplified case.....	70
Figure 45. Mesh used for the Simplified Case.....	71
Figure 46. Geometry and Boundary Conditions for the Air Suction Case.	73
Figure 47. Mesh used for the Air suction case.....	74
Figure 48. Geometry and Boundary Conditions for the Real Case.	76
Figure 49 Mesh used for the Real case.	77
Figure 50. Diagram of the Ladle-Tundish system and close-up of the Ladle-Tundish connection	79
Figure 51. Dimensions of the Ladle-Tundish connection.....	79
Figure 52. Real lower nozzle and Ladle Shroud and detail of overlapping connection and argon injection.....	80
Figure 53. Gasket between the Ladle Shroud and lower nozzle.....	80
Figure 54. Actual Ladle Shroud, schematic, and final water model.....	82
Figure 55. Lower nozzle and Ladle Shroud (A) schematic for model construction.....	83
Figure 56. Parts adaptation for model construction	83
Figure 57. Development and adaptation of Tundish-tank for water model.....	84
Figure 58. Tundish water model diagram at different views for Plexiglas model construction. ..	85
Figure 59. Ladle Shroud physical model attached to slide gate at the MPPC laboratory.....	86
Figure 60. Geometry generated in SpaceClaim © for the water-air mathematical model.....	87
Figure 61. Experimental set-up with water model Ladle Shroud and Tundish-tank	88

Figure 62. Predicted phase volume fraction contours for steel, air, and argon phases at 0.944 and 14.452 seconds on the symmetry plane.	91
Figure 63. Predicted phase volume fraction contours for steel, air, and argon phases at 29.675 and 32.173 seconds on the symmetry plane.	92
Figure 64. Predicted phase volume fraction contours for steel, air, and argon phases at 37.303 and 58.285 seconds on the symmetry plane.	93
Figure 65. Predicted contours for (a) absolute pressure, (b) velocity, and (c) turbulence kinetic energy at 58.285 seconds (quasi-steady state operation) on the symmetry plane.	95
Figure 66. Comparisons between predicted and theoretical absolute pressure along the Ladle Shroud.....	96
Figure 67. Predicted contours for (a) steel volume fraction and (b) absolute pressure at 41.853 seconds on the symmetry plane.	98
Figure 68. Predicted contours for (a) steel volume fraction and (b) absolute pressure at 42.154 seconds, after change of 1.2 mm gap boundary condition from wall to pressure outlet on the symmetry plane.....	98
Figure 69. Predicted velocity contour with vectors and detail at the lower nozzle-Ladle Shroud joint at 42.154 seconds on the symmetry plane.	99
Figure 70. Predicted phase volume fraction contours for steel, air, and argon phases at 0.574 and 4.018 seconds on the symmetry plane.	101
Figure 71. Predicted phase volume fraction contours for steel, air, and argon phases at 13.249 and 30.057 seconds on the symmetry plane.	102
Figure 72. Predicted phase volume fraction contours for steel, air, and argon phases at 35.364 and 77.788 seconds on the symmetry plane.	103
Figure 73. Predicted steel volume fraction 3D contours at different times in isometric view. ..	106
Figure 74. Predicted steel volume fraction 3D contours at different times in isometric view. ..	107
Figure 75. Predicted velocity and turbulence kinetic energy contours at 80.011 seconds on the symmetry plane.....	107
Figure 76. Predicted wall shear stress on the Ladle Shroud walls and Tundish at 80.011 seconds in isometric view.....	108
Figure 77. Filling stages of the Ladle Shroud-Tundish-tank water model at (at different times from an isometric right-hand top view.	109

Figure 78. Filling stages of the Ladle Shroud-Tundish-tank water model at different times from front view..... 109

Figure 79. Air bubbles generated in the liquid in the Tundish-tank surface In (a) front view and (b) isometric view..... 110

Figure 80. Comparison of the filling stage of the ladle shroud-tundish system at the start of the filling stage. (a) Real Case, (b) Mathematical water model and (c) Water model experiment results 111

Figure 81. Comparison of the filling stage of the ladle shroud-tundish system at half the time of the filling stage. (a) Real Case, (b) Mathematical water model and (c) Water model experiment results 111

Figure 82. Comparison of the filling stage of the ladle shroud-tundish system at the end of the filling stage. (a) Real Case, (b) Mathematical water model and (c) Water model experiment results 112

Figure 83. Multi-phase flow development inside a diverging ID ladle shroud in physical and mathematical modelling..... 113

List of abbreviations

ppm= parts per million

RT= Residence time, s

t= time, s

u = velocity, m/s

u_r = Stokes rising velocity, m/s

u_f = fluid velocity, m/s

\vec{u} = velocity vector, m/s

g = gravity acceleration, m/s²

P= pressure, atm or Pa

d= diameter, m

r= radius, m

V= volume, m³

ρ = density kg/m³

μ = dynamic viscosity, Pa s

μ_{eff} = effective viscosity, Pa s

μ_t = turbulent viscosity, Pa s

ν = kinematic viscosity, m²/s

σ = surface tensions, N/m

F_σ = surface tension force, N

κ_i = surface curvature

k= turbulence kinetic energy, m²/s² or kJ/kg

ε = dissipation rate, m²/s³

L= characteristic dimension, m

Re= Reynolds number, $\rho u L / \mu$

Fr= Froude number, $u^2 / g L$

Eu= Euler number, $p / u^2 \rho$

St= Stokes number, $u t / L$

α = volume fraction

\dot{m} = mass flow, kg/m²s

γ = media porosity

Abstract

Non-metallic inclusions (NMI's) are of great concern during liquid steel processing and have several sources, e.g., re-oxidation, slag entrainment, refractories, etc. As the demand for cleaner steels increases, the elimination of NMI's has gained importance. In particular, the elimination of small inclusions ($<50\ \mu\text{m}$) has become of great significance. The objective of the present work is to determine via mathematical and physical modelling the potential sources of inclusions in a real industrial Ladle Shroud (LS)-Tundish system by analyzing the multi-phase flow within a Ladle Shroud. Based on the findings, practical solutions can be proposed to improve the cleanliness of water-atomized steel powders in future projects. It is shown that Computational Fluid Dynamics (CFD) software is a powerful tool for studying liquid steel systems and for visualizing fluid flows within these Ladle Shroud-Tundish systems. Using ANSYS Fluent 19.0 software, three cases were simulated; the first one considers the initial flow of steel within a perfectly sealed Ladle Shroud, using a VOF (volume of fluid) approach to capture the two-phase flow of steel and air. For this, it is shown the initial interaction of steel and air will inevitably lead to re-oxidation of the steel, and generation of inclusions. Second, the possibility of subsequent air ingress of around 300 L/min through a 1.2 mm gap, generated by strong negative pressures at the top of the Ladle Shroud, is very possible with the current LS design. Finally, the modelling of the current Ladle Shroud operation in the presence of an argon shrouding gas, and a turbostop, was visualized, computationally. For this case, argon shrouding as practiced, was found to be insufficient to prevent suction of air into the shroud. Further, the large argon, or air/argon bubbles formed within the Ladle Shroud, will then exit to perturb the layer of slag above the steel in the Tundish. This will likely lead to the formation and entrainment of slag droplets, and further contamination of the final products. Part of the present work focused as well on the construction of a real-scale Ladle Shroud-Tundish physical model for further water modelling research. Some of the mathematical results were validated qualitatively with full-scale water model experiments by obtaining the visualization of the filling stage of the Ladle Shroud-Tundish system.

Résumé

Les inclusions non métalliques (NMI) sont très préoccupantes lors du traitement de l'acier liquide et ont plusieurs sources, par exemple la réoxydation, l'entraînement des scories, les réfractaires, etc. À mesure que la demande d'aciers plus propres augmente, l'élimination des NMI a gagné en importance. En particulier, l'élimination des petites inclusions ($<50 \mu\text{m}$) est devenue d'une grande importance. L'objectif du présent travail est de déterminer via une modélisation mathématique et physique les sources potentielles d'inclusions dans un véritable système industriel Ladle Shroud (LS)-Tundish en analysant l'écoulement multiphase au sein d'un Ladle Shroud. Sur la base des résultats, des solutions pratiques peuvent être proposées pour améliorer la propreté des poudres d'acier atomisées à l'eau dans les projets futurs. Il est démontré que le logiciel Computational Fluid Dynamics (CFD) est un outil puissant pour étudier les systèmes d'acier liquide et pour visualiser les écoulements de fluides dans ces systèmes Ladle Shroud-Tundish. À l'aide du logiciel ANSYS Fluent 19.0, trois cas ont été simulés ; la première considère l'écoulement initial de l'acier dans un tube de poche parfaitement étanche, en utilisant une approche VOF (volume de fluide) pour capter l'écoulement diphasique de l'acier et de l'air. Pour cela, il est démontré que l'interaction initiale de l'acier et de l'air conduira inévitablement à une réoxydation de l'acier et à la génération d'inclusions. Deuxièmement, la possibilité d'une entrée d'air ultérieure d'environ 300 L/min à travers un espace de 1,2 mm, générée par de fortes pressions négatives au sommet du carénage de poche, est tout à fait possible avec la conception du tube de poche actuelle. Enfin, la modélisation du fonctionnement actuel du carénage de la poche de coulée en présence d'un gaz de carénage argon et d'un turbostop a été visualisée par ordinateur. Dans ce cas, l'enveloppe d'argon telle qu'elle est pratiquée s'est avérée insuffisante pour empêcher l'aspiration d'air dans l'enveloppe. En outre, les grosses bulles d'argon ou d'air/argon formées dans le carénage de la poche sortiront alors pour perturber la couche de scories au-dessus de l'acier dans le répartiteur. Cela conduira probablement à la formation et à l'entraînement de gouttelettes de laitier et à une contamination supplémentaire des produits finaux. De plus, une partie du présent travail s'est concentrée sur la construction d'un modèle physique Ladle Shroud-Tundish à échelle réelle pour des recherches ultérieures. Certains des résultats mathématiques ont été validés qualitativement avec des expériences sur modèle d'eau à grande échelle en obtenant la visualisation de l'étape de remplissage du système Ladle Shroud-Tundish.

Acknowledgements

Firstly, and foremost, I would like to thank the guidance and ceaseless support provided by my supervisors Prof. Roderick I.L. Guthrie and Dr. Mihaiela M. Isac, and for giving me the opportunity to be part of a great research experience in conjoint with the industry and to have the opportunity to grow as a researcher, engineer, and person. I would like to also thank Dr. Luis Calzado for the ceaseless practical advice and support. As well I thank Mr. Sam Minter, for all his effort and work put for the construction of the physical models and adaptations. I am also thankful for the support and encouragement provided by the MMPC (McGill Metals Processing Center) students team, Rohit Tiwari, Ajay Panicker and Giacomo Di Silvestro. I would also like to thank the financial support provided by the National Science and Engineering Research Council of Canada and the MPPC's industrial sponsors: ANSYS, Rio Tinto Iron and Titanium, Rio Tinto Metal Powders and Nippon Steel Corporation. I would like to also acknowledge the financial support provided by the Mexican National Council of Science and Technology (CONACyT) for their financial support provided during my studies (CVU:1036046). Finally, I thank greatly my parents, Adriana Morales, and Miguel González back in Mexico, since I owe them everything and thank my dear brother and his wife, Miguel González-Morales and Alejandra Soto, for paving the road and being professional and life examples. Finally, I thank my beloved grandmother Carmen García, for being the kindest and most beautiful human example I have ever known, and to whom this work is dedicated. *(Finalmente, agradezco a mi amada abuelita Carmen García por ser el más bello ejemplo de nobleza y humanidad que jamás he conocido, y a quién dedico este trabajo)*

Introduction

During steel processing, the liquid metal encounters several sources of contamination, generating undesired inclusions in the liquid steel. Non-metallic inclusions (NMI) in steels have become of great concern in the last 50 years since they play an essential role in steel cleanliness. NMI can determine and influence the processing and application of any steel, meaning the material behaviour is intimately connected to the type, size, and distribution of NMI [1]. Important research has been made to eliminate detrimental NMI for the steel quality, and metallurgists have largely succeeded in eliminating “big” inclusions ($>50\ \mu\text{m}$) with process control and geometry modifications, especially in the Tundish, the last opportunity to eliminate NMI before casting. Nevertheless, the problem of eliminating small inclusions ($<50\ \mu\text{m}$) in the Tundish remains relatively unsolved and has become one of the main focuses of steel processing research.

To address the elimination of small inclusions from liquid steel, some alternatives have been considered, and it has been found that small NMI can be attached and removed by micro gas bubbles from the molten steel. Mathematical modelling efforts have concluded that the optimum bubble size for small NMI removal from liquid steel is between 0.5-2.0 mm [2]. As well, recent water modelling results show that small NMI removal is enhanced by the injection of gas micro-bubbles through the Ladle Shroud, resulting in a decrease of around 50% of small NMI leaving the water system. This was confirmed with mathematical modelling [3].

So far, it has been proved that micro-bubbles can effectively eliminate small NMI in mathematical modelling and water physical modelling approximations. However, applying the concept in actual steel processing, where some industrial challenges will surely arise, is still pending. If the industrial implementation of micro-bubbles can be demonstrated to be successful, it will be a breakthrough for the steel industry. The objective of the present work is to summarize recent efforts to model, mathematically and physically, NMI control in the Ladle Shroud and Tundish systems. The intention is to formulate and define the root causes for present levels of NMI, and to apply these findings to resolve present problems facing RTMP (Rio Tinto Metal Powders). This will then hopefully lead to a reduction in the number of NMI's in their steel powder products. During the development of the project, it was noticed that the Ladle Shroud design and operation plays an essential role in the steel cleanliness and the sources of some inclusions can be attributed to its design and operation.

Chapter 1 Literature Review

1.1- Inclusions in steels

Non-metallic inclusions are of great concern in steels, as they can determine many properties of the steel, during processing and in the final application. Inclusions are inherent to steel, due to the complexity of Steelmaking and Steel Processing, where the molten metal interacts with several potential inclusion's sources. There are mainly two types of sources: *indigenous* and *exogenous*. *Indigenous* sources correspond to those generated by the chemical processing like the deoxidation, *Exogenous* sources correspond to those whose origin correspond to external unintended factors, like the slags and refractories. Figure 1 presents the several potential exogenous and indigenous inclusions' sources in Steelmaking. Inclusion' control and Engineering has gain great importance since the 1980s [4] to modify inclusions with desirable properties and improve the steel processing behavior and properties.

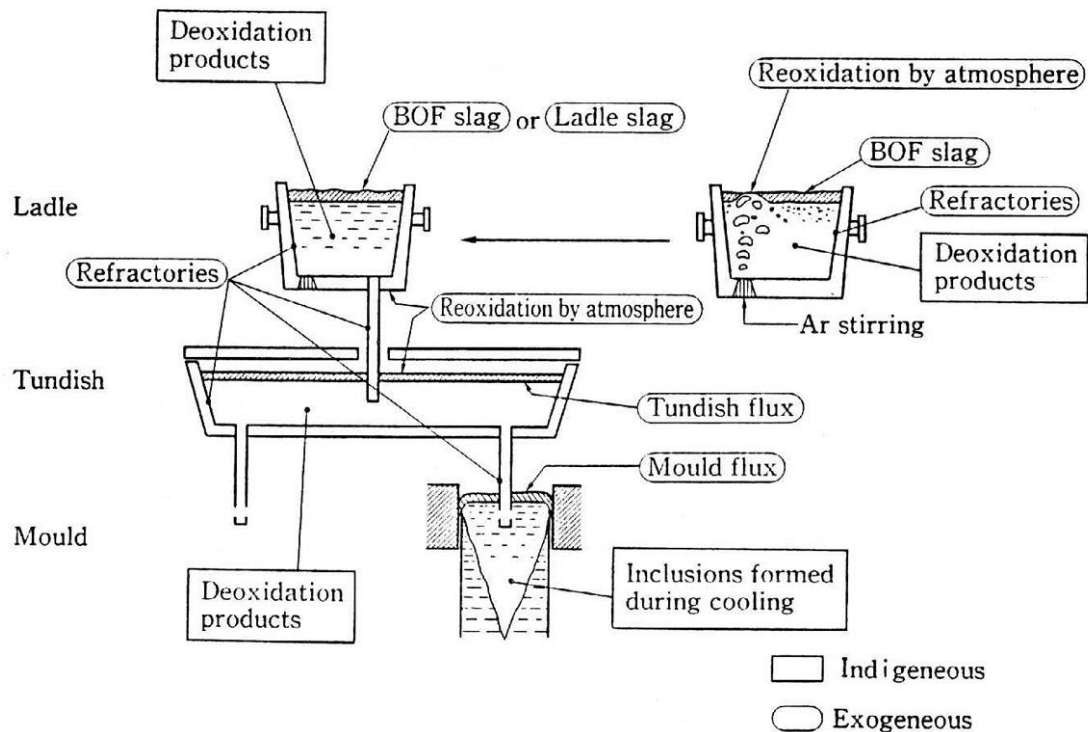


Figure 1. Sources of non-metallic inclusions in Steelmaking [5]

Non-metallic inclusions are mainly conformed of oxides like Al_2O_3 , SiO_2 , TiO_2 , CaO , MgO MnO and some sulphides like CaS and MnS , depending on the steel composition and chemical

treatment during Steelmaking. During Hot Rolling, the inclusions can be deformed or generate cracks depending on the chemical composition, size, and morphology. Figure 2 presents microstructures of different inclusions (Al_2O_3 , SiO_2 , TiO_2 , MnO) after Hot Rolling. Figure 3 shows an example of an inclusion promoted cack during hot rolling.

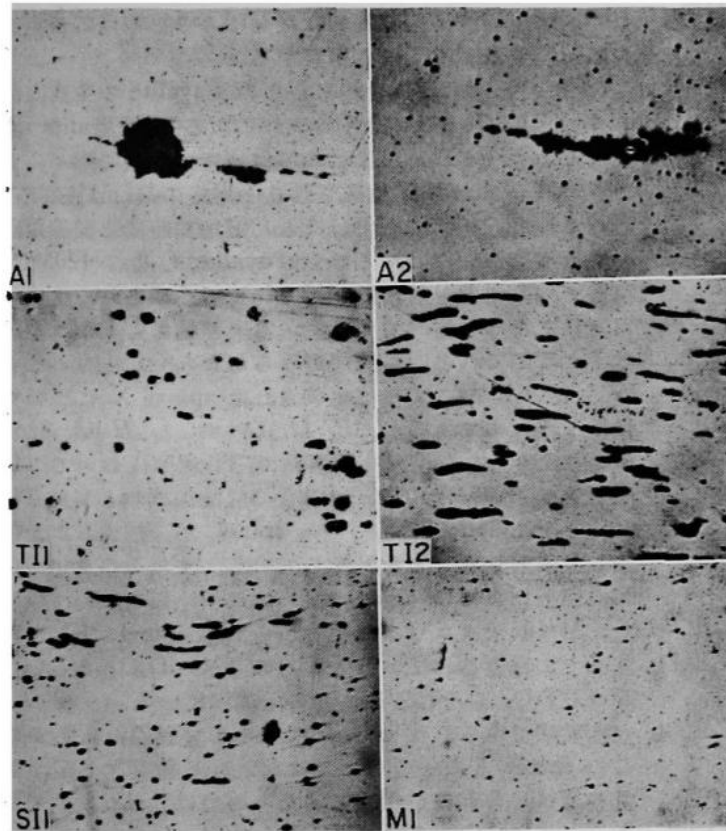


Photo. 2. Microstructure of hot rolled specimens.
×100 (4/5)

Figure 2. Different types of inclusions after Hot Rolling; A1: Al_2O_3 inclusions; A2: Al_2O_3 inclusions cluster; T11 & T12: TiO_2 inclusions; S11: SiO_2 inclusions; M1: MnO inclusions. [6]

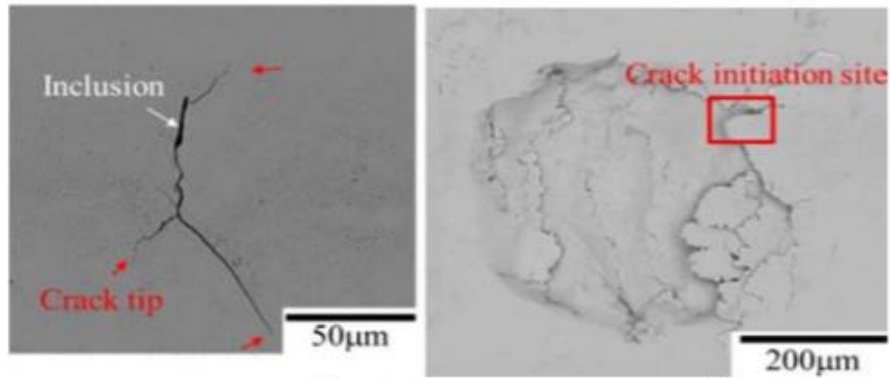


Figure 3. Inclusion-Crack initiation during Hot rolling [7].

In 2002, Zhang & Thomas [8] published a compelling review of the state of the art in the evaluation and control of steel cleanliness. The review focused on LCAK (Low Carbon Aluminum Killed) steels, which are very prone to sliver cracks, generated by aluminates from aluminum de-oxidation. They provide guidelines and concepts that can be applied for a wide range of steels. Each type of final steel product will have a maximum inclusion size and chemical impurities concentration (ppm). Both must be minimized to avoid compromising the steel's quality. Table 1.1 summarizes the cleanliness requirements for each type of steel product.

Table 1.1: Cleanliness requirements for some types of steel products. (Adapted from [8].)

Steel Product	Maximum chemical impurity	Maximum inclusion size
IF Steel	[C]≤30 ppm, [N] ≤40 ppm, T.O.≤40 ppm	
Automotive deep-drawing sheet	[C]≤30 ppm, [N] ≤30 ppm	100 µm
Drawn and ironed cans	[C]≤30 ppm, [N] ≤30 ppm, T.O.≤20 ppm	20 µm
Line pipe	[S]≤30 ppm, [N] ≤35 ppm, T.O.≤30 ppm	100 µm
Ball bearings	T.O.≤10 ppm	15 µm
Tire cord	[H]≤2 ppm, [N] ≤40 ppm, T.O.≤15 ppm	10 µm
Heavy plate steel	[H]≤2 p, [N] 30-40 ppm, T.O.≤20 ppm	Single inclusion 13 µm, Cluster 200 µm
Wire	[N] ≤60 ppm, T.O.≤30 ppm	20 µm
Powder*	T.O.≤50 ppm	100-200 µm

As well, on the same review, the NMI's sources, their general morphology and their chemical compositions are presented:

1. Deoxidation products (Al_2O_3)
2. Reoxidation products (FeO , MnO)
3. Slag entrainment (Spherical)
4. Exogenous (Dirt, sand, refractory irregular shape)
5. Chemical reactions (Ca inclusions)

Additionally, the various methods to evaluate steel cleanliness were comprehensively discussed by Zhang & Thomas [8]. Two types of method are used, direct and indirect; direct methods refer to the detection and quantification of NMI directly on solid steel sections and NMI volumes after solidification and in the liquid steel prior to casting; indirect methods, which are most common due to their practicality, refer to the quantification of chemical components indicative of steel cleanliness, e.g., total oxygen and nitrogen. It is worth mentioning that the LiMCA system, widely used in aluminum smelters around the world, classified as a direct method, was commented as being used on-line, but with the problem that gas-bubbles and inclusions can be hard to differentiate. The authors recommend combining several methods for an accurate and comprehensive evaluation of steel cleanliness.

Zhang & Thomas [8] summarized some general guidelines to control steel cleanliness in the Ladle, where the NMI can be lowered a 65-75%, and in the Tundish, where the NMI can be lowered a 20-25%. Regarding the Ladle operations, tap oxygen content should be controlled according to the quality requirements; FeO and MnO contents should be low in the slag, as these promote Al_2O_3 reoxidation; Ladle stirring promotes NMI flotation until a threshold gas flowrate; Inclusion modification with Ca can be done to “soften” and render liquid NMI as previously commented. Regarding Tundish operations, in general its depth and capacity should be increased to increase τ enhancing NMI removal; special care should be put in casting transitions as they are responsible for most cleanliness defects and air absorption; Tundish flux, stirring and flow control were mentioned as other important points to control NMI in the Tundish. This will be commented on, in detail, later. Furthermore, some recommended transfer operations were summarized, including open pouring and shrouding, ladle opening, argon protection and sealing, nozzle clogging prevention and the selection of shroud material.

1.2.- Inclusions 'control

Additionally, the various methods to evaluate steel cleanliness were comprehensively discussed by Zhang & Thomas [8]. Two types of method are used, direct and indirect; direct methods refer to the detection and quantification of NMI directly on solid steel sections and NMI volumes after solidification and in the liquid steel prior to casting; indirect methods, which are most common due to their practicality, refer to the quantification of chemical components indicative of steel cleanliness, e.g., total oxygen and nitrogen. It is worth mentioning that the LiMCA system, widely used in aluminum smelters around the world, classified as a direct method, was commented as being used on-line in smelters around the world. The authors recommend combining several methods for an accurate and comprehensive evaluation of steel cleanliness and commented that two types of NMI's control are done in practice: Physical removing (Figure 4) and chemical control

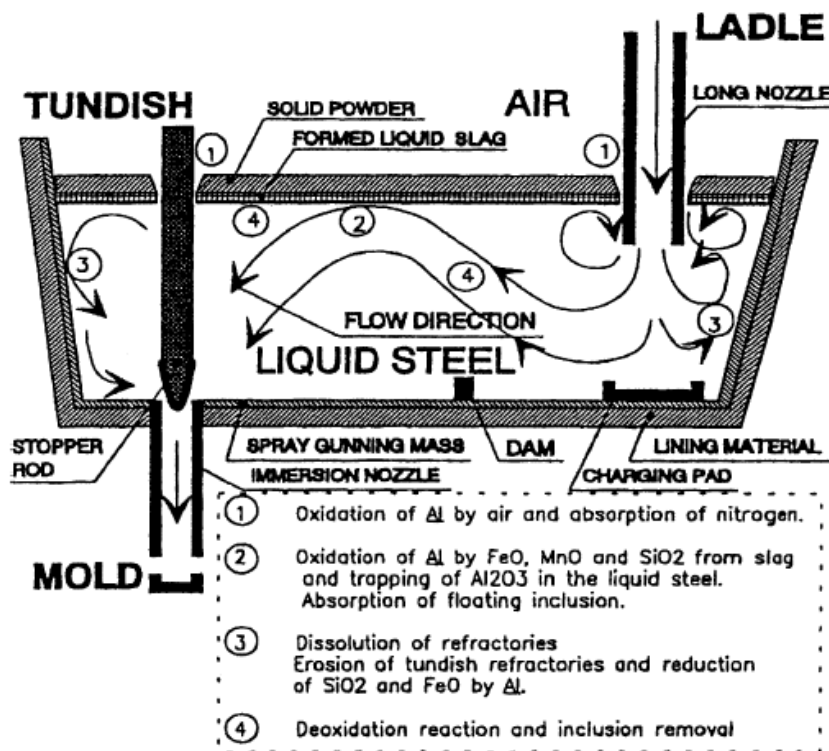


Figure 4. Inclusion-physical removing in Tundish [8].

Chemical control during Steelmaking is applied to decrease the Oxygen content in the steel and therefore minimize the nucleation of oxides, by deoxidizing with Aluminum, Calcium or Silicon

due their strong affinity with Oxygen. Figure 5A shows the decrease with time of sol [O] after Silicon treatment. This chemical control can promote the nucleation of a specific type on inclusions, with desired properties, like CaS or MnS, which show a desired "smooth" behavior during Hot Rolling. Slag chemical control can be applied as well, to have a specific thermodynamic equilibrium and promote the generation of a desired inclusions composition, as depicted in Figure 5B, where a specific $Al_2O_3 - SiO_2 - CaO$ slag composition promotes an inclusion composition, which will be liquid at 1470 °C avoiding nozzle clogging in the Ladle. Additionally, with chemical control the inclusions composition can be modified to obtain inclusions with desirable properties during Hot Rolling like MnS and Anorthite.

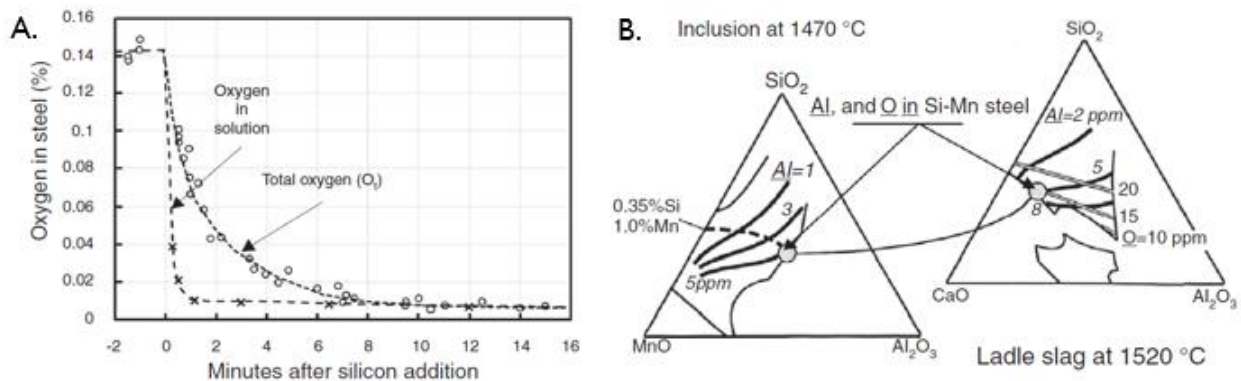


Figure 5. Inclusions Chemical Control: A) Silicon Addition to decrease sol. [O] in liquid steel; B) Si-Mn killed steel with slag composition (Right) control in Ladle to promote specific inclusions composition (Left) with low melting point to avoid nozzle clogging [1].

In 2016 Sahai [9], published the latest review, focusing on steel cleanliness and NMI control in the Tundish. He summarized the latest Tundish technology and revised the types of NMI: Exogenous ($>50 \mu\text{m}$) and Indigenous ($50 < \mu\text{m}$). Re-oxidation during ladle to Tundish transfer and slag entrainment NMI, usually with a size bigger than $100 \mu\text{m}$, can be avoided with adequate use of a SEN (Submerged Entry Nozzle use will be discussed in detail later) or a slag detection device, to stop the melt flow from the ladle. The effect of the Tundish size is revised, being the simplest method to increase τ and enhance NMI removal, as well as increasing steel productivity. Said methods have been widely used by the steel industry. Flow control devices effect is also commented on, impact/pour pads being widely use in the industry, since they delay refractory erosion, reduce incoming flow turbulence, and promote surface directed flow. In general, Sahai [9] comments that flow control devices are effective for the elimination of NMI bigger than $100 \mu\text{m}$.

Some other novel methods are discussed in the same review, like gas injection in the Tundish, where argon gas injection through a porous plug has proved to be successful to eliminate large inclusions. A large Tundish without flow modifiers has been shown to promote big NMI flotation and reduce vortexing phenomena. Melt temperature control is mentioned as well as an important parameter for unsteady state Tundish operations, since low and high superheat can increase the NMI count. For the casting of SULC (Super Ultra Low Carbon) most of the recommendations should be followed due to the high cleanliness requirements for the type of steel. Figure 6 presents a summary of the methods used in controlling the levels of NMI in a modern continuous casting system.

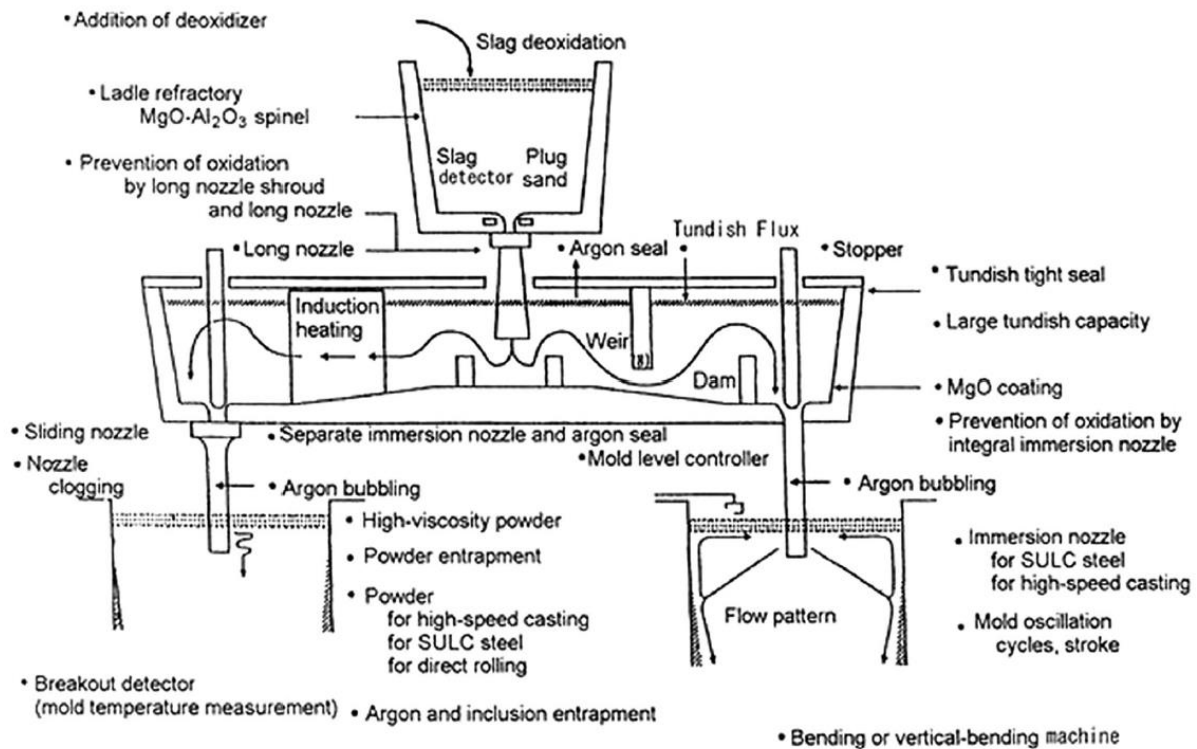


Figure 6. Continuous casting system for SULC Steels with methods for NMI control. Taken from [9].

Sahai [9] comments on some non-traditional technologies, *e.g.*, H-shaped Tundish, centrifugal Tundish with a magnetic field promoting centrifugal force and inclusions separation. These technologies are still on its early stages and have been scarcely applied in the steel industry. Sahai [9] concludes its review with some general recommendations to improve steel cleanliness in a Tundish:

1. Avoid re-oxidation

2. Ladle to Tundish transfer with SEN or Ladle Shroud.
3. Avoid slag entrainment with slag detection system.
4. Use a large deep Tundish. If this is not possible, use flow control devices depending on each specific situation.

The presented steel cleanliness guidelines have proven to be successful for the steel industry, improving steel cleanliness, but the elimination of small inclusions ($<50\ \mu\text{m}$) remains a relative unsolved issue. “Tundish metallurgy” and its main tool mathematical and physical modelling are discussed next.

1.3.- “Tundish Metallurgy” Literature review

A Tundish refers to a metallurgical vessel, located after the ladle in the steelmaking process, in which molten steel flows before poured solidifying in a continuous casting mould, or used in an atomization operation. In a Tundish several metallurgical phenomena occur, such as inclusions separation, flotation, alloy trimming of steel, superheat control and thermal and chemical homogenisation [10] & [11]. This metallurgical vessel plays an essential role in steel quality and has gained more relevance recently, because the quality requirements of steel have increased significantly since 1980. This led to the development of a separate area of secondary steelmaking known as “Tundish metallurgy” [10]. Research on “Tundish metallurgy” has mainly focused on Tundish designs and operations to promote the flotation and elimination of undesired non-metallic inclusions (NMI) from the liquid steel and to avoid further contamination. NMI including oxides, sulphides, nitrides, and carbides, generated by the precipitation of some chemical components of the steel. Large NMI ($> 50\ \mu\text{m}$) are highly detrimental to steel quality generating processing difficulties and degrade the final steel quality [9]. Large NMI can be eliminated by controlling some important Tundish factors, e.g., Tundish depth, Tundish lining refractory, Tundish flux, gas stirring and Tundish flow control [8].

“Tundish metallurgy” main tools are physical and mathematical modelling. Since 1999, three separate reviews have summarized the most relevant Tundish research of each decade (1990s, 2000s and 2010s). Mazumdar & Guthrie [10] introduced the concept of “Tundish metallurgy” and

referred to the relevance of the Nominal Residence Time (NRT) for the study of the Tundish as a refining vessel. NRT is defined as:

$$NRT = \frac{\text{Volume of the Tundish}}{\text{Volumetric flow rate of steel into (or out of) the Tundish}}$$

where V can be considered as comprising; 1) well-mixed, V_{∞} , 2) plug flow, V_{plug} , and 3) dead, V_{Dead} , volumes.

Additionally, the similarity considerations of the water physical modelling were summarized, *e.g.*, the kinematic viscosity of liquid steel ($0.916 \times 10^{-6} \text{ m}^2/\text{s}$) at $1600 \text{ }^{\circ}\text{C}$ being practically equal to the water ($1.0 \times 10^{-6} \text{ m}^2/\text{s}$) at room temperature (20°C):

$$\nu_{\text{Steel}} \approx \nu_{\text{Water}}$$

This similarity allows the physical approximation of liquid steel with water, making Tundish scale water models widely used for the study of the Tundish fluid dynamics phenomena. The geometry similarity should be considered as well, meaning every dimension must have a fixed ratio with the full-scale process, with the scale factor (λ), defined as:

$$\lambda = \frac{L_{\text{model}}}{L_{\text{full scale}}}$$

The dynamic similarity refers to the fixed ratio between the forces acting on the fluid, described by the Navier-Stokes equations, which dimensionless form is represented as:

$$Eu = f(Re, Fr)$$

The previous equation requires the Re (Reynolds Number, molecular viscous forces), and the Fr (Froude Number, inertial and gravitational forces) must be equal in the full-scale process and in the scale model. However, both dimensionless numbers similarity can only be satisfied in full scale models ($\lambda=1$). Mazumdar & Guthrie [10] pointed out that flows in a Tundish are mainly dominated by inertial and gravitational forces due to the generated turbulence and the essential condition for dynamic similarity in a Tundish system should primarily be related to equality of the Fr number, for reduced scale models:

$$Fr_{\text{model}} \approx Fr_{\text{full scale}}$$

In the same review, the metallurgical performance of a Tundish was discussed, emphasizing its role to float out undesired NMI, and proposing some general guidelines to ensure the separation of NMI in the Tundish:

1. To have a minimum spread of Residence Times.
2. To have a minimum dead volume, defined as $RT > 2$ times the Nominal Residence Time τ_0
3. To have a large ratio of plug to dead volume.
4. To promote a surface directed flow.
5. To have a quiescent slag layer.
6. Constrained regions of mixing.

Additional to the mentioned guidelines, the role of “flow control devices (FCD’s)” *e.g.*, dams, weirs, baffles, turbo-stops and anti-vortex nozzles, to aid in respecting one or more of the guidelines to ensure NMI flotation, was commented on, and summarized. Its use, and selection, should be specific for each Tundish. Dams, weirs, and baffles, in general increase the RT and hence probability of the flotation of the NMI; Turbostops, reduce the turbulence on the flow entry region, promote a quiescent bath and direct the entering flow to the surface; anti-vortex nozzles avoid vortexes formation and slag carry over to the subsequent process. Mazumdar & Guthrie [10] also comment on the first applications of gas bubbles to enhance NMI inclusions separation and on the early physical modelling approximations of NMI with hollow glass spheres and its quantification and effect of flow modifiers with APS (Aqueous Particle System)/ESZ (Electric Sensing Zone) sensors.

As well, the first mathematical modelling efforts were summarized in the same review, presenting the first RT empirical equations and the inclusion transport equation with the Stokes rising velocity (u_r):

$$u_r = \sqrt{g d_p^2 \frac{\Delta\rho}{18\mu}}$$

where g , d_p , $\Delta\rho$ and μ correspond to the gravity acceleration, the particle diameter, the fluid and particle density difference and the dynamic viscosity, respectively. Assuming ideal absorption at the upper slag-metal interface, resulted in $NMI > 120 \mu\text{m}$, being entrapped in the slag phase and,

based on the Stokes rising velocity, $NMI < 40 \mu\text{m}$, were unable to be substantially removed from the steel flow through the Tundish.

Chattopadhyay, Isac and Guthrie [11] summarized the Tundish physical modelling advances of the 2000's decade, including the tracking of particles in water scale models with anemometry and Particle Image Velocimetry (PIV). As well, the importance of additional dimensionless numbers was discussed. The Bo (Bond number, buoyancy to surface tension forces ratio) is relevant when simulating a slag phase, usually with oils or emulsions, and the Tu (Tundish Richardson, buoyancy force to inertial force ratio) becomes of importance when non-isothermal conditions are simulated, where buoyancy can contribute significantly to the fluid dynamics of the system. Regarding physical modelling of the inclusions, the following equivalence should be considered:

$$\frac{u_{f,m}}{u_{f,f.s}} = \frac{u_{r,m}}{u_{r,f.s}}$$

where u_f denote the fluid velocity, and u_r denotes the Stokes rising velocity for the model (m) and the full scale (f.s.) systems, respectively. One limitation of the above similarity is that small inclusions ($< 50 \mu\text{m}$) mostly do not follow the Stokes rising velocity regime. Additionally, a physical modelling hierarchy was mentioned, if chemical non-isothermal and chemical transports modelling is desired: First, dynamic similarity, then thermal similarity and last, chemical similarity, should be accomplished.

In the same review by Chattopadhyay *et. al* [11], the differences and the appropriate selection for turbulence models for the mathematical modelling of Tundish systems were discussed, based on the findings of several researchers. The most widely used model remained the RANS (Reynolds Average Navier-Stokes) **standard k-ε model**, but this has the drawback that it overestimates mixing situations. On the other hand, the RNG k-ε model is more accurate for high curvature streamlines and swirling motions and can be easier to converge compared to the standard k-ε. As well, the first applications of the **realizable k-ε model** were commented on. A two-fluid model was proposed as an alternative to the standard k-ε model which overestimates cases where highly turbulent and laminar regions co-exist, being the case for most Tundish systems. The two-fluid model divides the system into two interpenetrating fluids, one being turbulent and the other laminar, which are allowed to interchange mass, heat, and momentum.

Regarding the mathematical modelling of inclusions, the use of the Eulerian-Lagrangian frame was discussed, where first the N-S equations for the fluid are solved and then coupled via the F_d (Drag force), with the Lagrange frame equations for computing inclusions' trajectories. As well, the addition of the F_p (Added mass) to the inclusion's trajectories equation was discussed. All the advances on the effects of FCD's in the 2000 decade were summarized, allowing for a better understanding and improvement of the Tundish as a NMI cleaning vessel. Finally, Chattopadhyay *et. al* [11] concluded that there was a lack of slag entrainment phenomena understanding and modelling, which can be an important source of contamination in the Tundish, and still few non-isothermal mathematical models had been developed.

Mazumdar [12] has presented the most recent review on Tundish research for the 2010 decade, commenting that less research had been done between 2010-2019, compared to the two previous decades. Special emphasis was put on the transient phenomena in the Tundish (Start-up, ladle change over and end of sequence), since the steady-state phenomena had been deeply researched during the preceding decades. In the start-up, severe reoxidation and early slag entrainment can occur, due to the high turbulence and impact of the incoming metal flow with the refractory. During ladle changes, material and thermal mixing and slag emulsification can take place; and at the end of sequence the metal level decreases, generating vortexing and late slag entrainment. The summary discussed by Mazumdar [12] is presented in Figure 7.

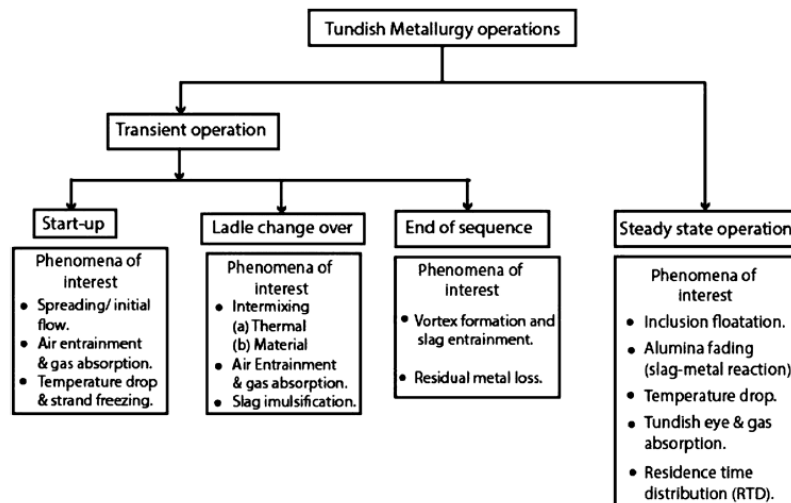


Figure 7. Summary of Tundish transient and steady state operations [12].

The advances in the mathematical multiphase modelling were summarized, the N-S equations coupled with the DPM (Dispersed Phase Model) for bubbles and inclusions trajectories calculations; the TOE (Tundish Open Eye) modelling and the VOF (Volume of Fluid) coupled with the DPM model to simulate gas-metal-slag Tundish systems were all addressed. Furthermore, mathematical models in transient state have been recently successfully applied to study transient state operations e.g., slag entrainment and ladle-change operations. However, some other transient phenomena involving moving solids, such as stopper rod, or nozzle contractions, present the challenge of generating a dynamic mesh accompanied by elevated computer costs. Start-up operations, transient energy flows, and mass transport phenomena simulations, were not reported by Mazumdar [12] in 2019. Most importantly, experimental results and industrial validation of mathematical results have been far less frequent.

The minimum number of partial differential equations (PDE's) required to mathematically formulate different phenomena of interest in Tundish systems were also summarized by Mazumdar [12] and are presented on Table 1.2. In the same review, the importance of the Ladle Shroud as an important Tundish flow controller was mentioned and some physical and mathematical results of a Ladle Shroud simulation were presented and will be commented later.

Table 1.2: Number of PDE's depending on the phenomena of interest in a Tundish system.

(Adapted from [12]).

Phenomena of interest	Modelling configurations	Number of governing Partial Differential Equations'					Total of required pde's
		Flow	Turbulence	DPM	Thermal mixing	Mass Transfer	
Steel flow in a full Tundish	3-D homogeneous turbulent flow	4	2	-	-	-	6
Steel flow and bubble/inclusions motions	3-D homogeneous turbulent flow and particle motion	4	2	3	-	-	9
Steel-gas flow and bubble/inclusions motions	3-D turbulent 2 phase VOF and particle/bubble motion	5	2	3	-	-	10

Steel-gas-slag flows, bubble/inclusion motion, RTD/intermixing, thermal energy distribution ad slag metal transfer	3-D transient turbulent, 3 phase VOF-DPM, thermal energy, bubble/inclusion motion, mixing and mass transfer of species	6	2	3	3	2	17
---	--	---	---	---	---	---	----

To illustrate quantitatively the Tundish mathematical modelling development, Mazumdar [12] introduced the AIM (Advancement index of modelling) parameter, which refers to the ratio of partial differential equations solved to the required to describe a two dimensional, homogeneous, and turbulent flow. The advancement of the AIM parameter throughout the years is presented in Figure 8.

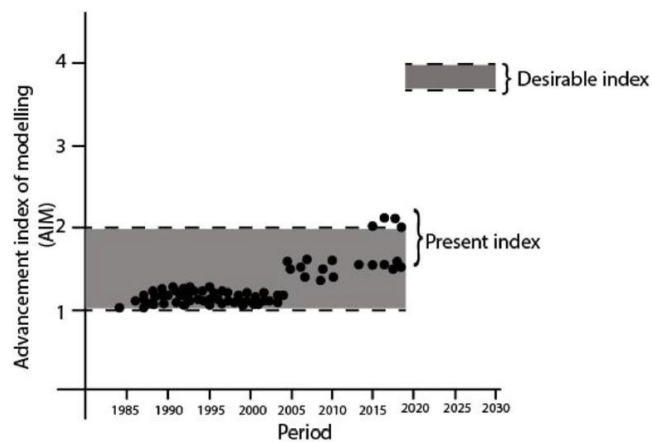


Figure 8. Advancement of the AIM in Tundish mathematical modelling research [12].

On the same review, the importance of the Ladle Shroud as an important Tundish flow controller was mentioned and some physical and mathematical results of a Ladle Shroud simulation were presented and will be commented later. Finally, Mazumdar emphasises the importance of integrating mathematical modelling results with experimental and industrial results for the successful application of “Tundish metallurgy” to solve actual industrial problems, although the integration has diminished over the years.

The previous basic similarity conditions for the water physical modelling of the Tundish have been followed in general by the research done on the last 30 years, has proved to be successful in solving industrial Tundish problems, especially in the flotation and elimination of large Non-metallic Inclusions (NMI), or agglomerates.

1.3.1 Tundish mathematical modelling review of the last 5 years

The previous basic similarity conditions for the water physical modelling of the Tundish have been followed in general by the research done on the last 30 years, has proved to be successful in solving industrial Tundish problems, especially in the flotation and elimination of large Non-metallic Inclusions (NMI), or agglomerates.

In 2016, Chen, Ni, Jonsson *et al.* [13] presented an improved understanding of the deposition of small inclusions through the steel-slag interface, providing a more accurate mathematical model to describe the inclusions removal through the Tundish slag. A “sink term” was added to the slag boundary cells, containing the contribution from the Stokes rising velocity and the liquid steel vertical velocity component. Additionally, the deposition velocity is introduced, calculated via the turbo-phoretic model. Chen *et al.* [13] used the Eulerian framework to calculate the transport of the inclusions, contrary to the usual Lagrangian framework, introducing into the equations the drift velocity (u_p) and the deposition flux (S_C), defined as:

$$u_p = \frac{2(\rho - \rho_p)gr^2}{9\rho\nu}$$

$$S_C = V_{dep} \cdot (\rho C) \cdot \frac{A}{V}$$

where ρ and ν correspond to the density and kinematic viscosity of the liquid phase; ρ_p and r indicate the inclusions' density and radius; V_{dep} , C , A , V indicate the deposition velocity, inclusions concentration and the area and volume of the control volume. The authors evaluated the removal of very small inclusions with a size of 1-9 μm in a Tundish, with and without, weir and dam, for three slag roughness conditions. The authors concluded that the inclusion removal ratio was increased for bigger inclusions and with higher slag roughness values. As well, the use of a weir and a dam, increase the removal ratio of “big” inclusions (9 μm), whereas the Tundish without

flow modifiers showed a better performance at eliminating “small” inclusions (1 μm and a strong paralleling flow near the top surface is essential for the removal of small inclusions (1-9 μm), as shown in Figure 9.

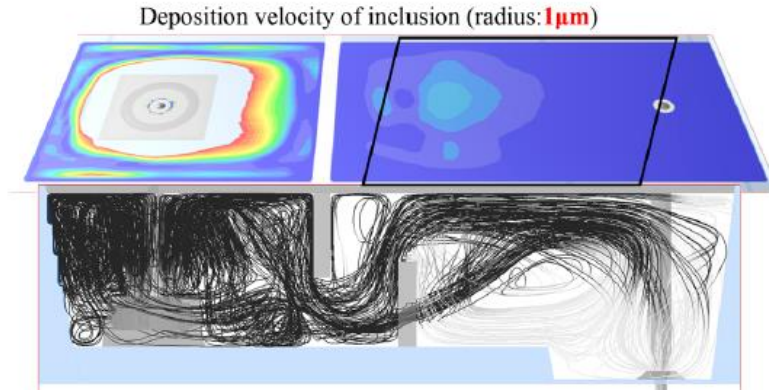


Figure 9. Tundish with a strong paralleling flow near the surface with weir and dam. Inclusions’ trajectories and deposition velocities calculated by Chen et al. [13].

In 2017, Ni, Jonsson, Ersson and Jönsson [14] published a study on an inclusion’s behavior in a Tundish with a swirling flow SEN. The author used the realizable k-ε Turbulence model and DPM for inclusions tracking, introducing two wall boundary conditions “reflect” and “trap”. Slag-inclusion interactions were neglected, and the inclusions were assumed to be removed once they touched the surface. Two types of inclusions were analysed, Ce₂O₃ and Al₂O₃. A Lagrangian Particle tracking model was used, which included the drag force (F_D), buoyancy force (F_g), virtual mass and the Saffman’s lift force. A particle stochastic turbulence model was used to consider the turbulence fluctuations on the inclusions motion due to the strong eddies formed in the swirling SEN. The authors evaluated the removal rate of both types on inclusions with a size range of 1-500 μm. To evaluate the interaction between a particle and a fluid, the author commented on the Stokes number (St), defined as:

$$St = \frac{\tau_p}{\tau_f}; \tau_p = \frac{\rho_p d^2}{18\mu}; \tau_f = \frac{\nu}{u_\tau^2}$$

where τ_p and τ_f are the particle momentum response time and a time characteristic of the flow field respectively; u_p refers to the friction velocity, which depends on the shear stress and fluid density. If $St \ll 1$, the inclusions will have enough time to respond to the flow changes and the inclusion and fluid velocities will be equal, If $St \gg 1$, the inclusions will have not enough time to

follow the fluid flow and will have the opportunity to be separated when encountering a strong velocity gradient.

Cwundzinski [15] presented in 2017 an analysis of the effects of a novel argon gas injection system, located in the middle of the Tundish, on the liquid fluid flow. The author used the realizable $k-\varepsilon$ Turbulence model, validated via water modelling, and the DPM model to calculate the argon injection-liquid interaction and bubbles trajectories under iso-thermal and non-iso-thermal conditions, the mathematical results agreed well with the water-modelling experiments. The author found that a gas barrier is formed, and strong recirculation zones are created, separated by the gas curtain and that the gas flow can significantly reduce the stagnant volume flow. In 2018, Aguilar-Rodriguez, Ramos-Banderas, Torres-Alonso *et al.* [16], analysed the effect of argon bottom feeding on the Tundish flow and inclusions removal. The standard $k-\varepsilon$ Turbulence, DPM and VOF models were used to model mathematically the turbulence flow, the inclusions trajectories and the three phases' interactions (steel-slag-argon) respectively. Three gas curtain positions were evaluated to determine the effect on the inclusions removal rate and the gas curtain closest to the steel inlet with the highest argon input rate, presented the best results for inclusions removal, eliminating 85-95% of the inclusions in a size range of 1-60 μm . The gas curtain near the steel inlet forms an "argon barrier, which promotes the flow recirculation and directs the flow towards the surface, increasing the inclusions removal as being trapped by the slag, shown in Figure 10. As well the slag opening was evaluated, concluding that a high argon flow near the steel outlet generates the biggest slag opening.

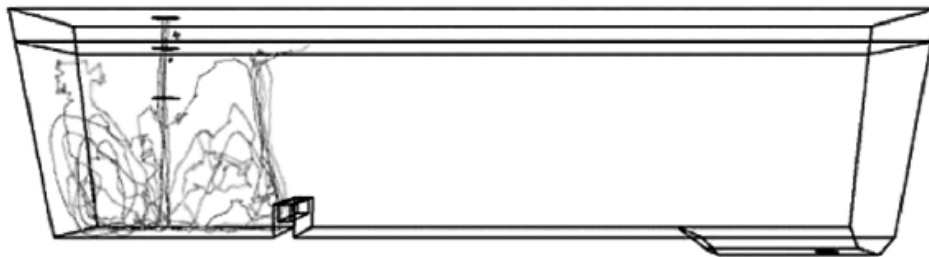


Figure 10. Tundish with gas curtain near the inlet, directing the inclusions towards the surface to be removed. Inclusions' trajectories calculated by Aguilar-Rodriguez et al. [16].

In 2018, Chatterjee, Li and Chattopadhyay [17] performed an analysis of the effect of argon gas bubbles on the Tundish open eye (TOE) by coupling the DPM (bubbles trajectories and interactions) and the VOF (steel-slag interaction) models. The standard $k-\varepsilon$ turbulence model was

used and the virtual mass, pressure force and a two-way turbulence coupling, as the momentum interchange between the bubbles and the liquid phases is significant and will generate the TOE. The author used four different argon flow rates (0, 5, 10 and 20% of the steel volume flow rate) to calculate the injected bubbles diameter and incoming velocity. Time dependant volume fraction contours of the slag phase were obtained to assess the effect of the different argon flow rate on the TOE formation. The development of the TOE with a high argon flow rate (20%) at different times is shown in Figure 11 where slag emulsification and droplets can be observed. It was also found that the TOE is dependent on the shape of the generated plume by the gas bubbles and threshold argon flow ranges were identified to avoid a critical TEO area. The mathematical results were compared with industrial TOE measurements and good correlation was found and an empirical correlation was obtained [17]:

$$A_{TOE} = 0.017Q_{argon\%} - 0.159$$

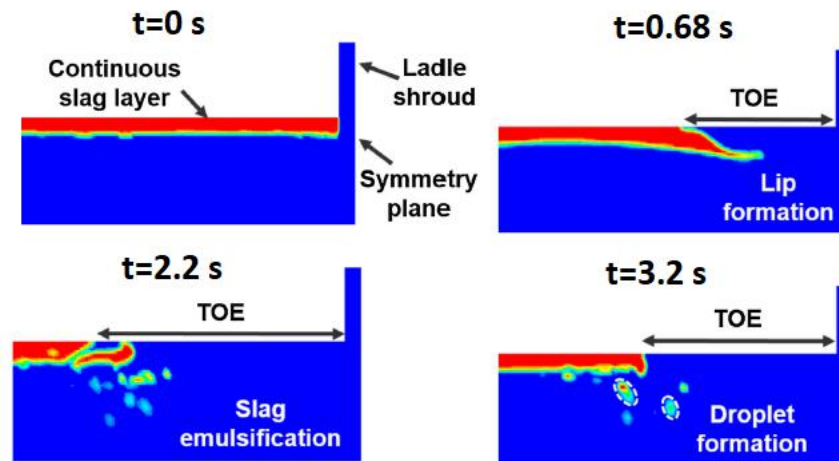


Figure 11. Slag phase volume fraction contours at different times with high argon flow rate injection predicted by Chatterjee et al. [17].

In 2019, Mishra and Mazumdar [18], proposed different designs of turbostops and evaluated their inclusions removal efficiency through RTD analysis in different designs of Tundish (delta, T and rectangular-shaped). The authors used a single-phase steady system with the k-ε Turbulence to model the turbulence and the transient non-reacting species equation to obtain the RTD curves. A vertical and a tapered turbostop wall were compared, resulting in that the vertical one presented turbulent ingress and mixing of incoming and rising streams, whereas the tapered wall, redirected progressively the flow towards the surface without interference. Additionally, a circular-

shaped turbostop presented the best performance, in the three Tundishes shapes, when compared to a rectangular and “similar to the Tundish”-shaped turbostops. As well, the effect of surface modifications in the turbostops were evaluated, finding no significant improvement.

In 2020, Neumann, Asad,, Kasper and Schwarze [19, 20] evaluated the effect of ceramic filters on the steel cleanliness in the Tundish with mathematical modelling. The authors considered two cleaning methods, active filtration, direct deposition of the inclusions on the filter, and reactive cleaning, CO bubbles, generated by the C of the filter and the dissolved oxygen, capture, and lift the inclusions to the slag. A Eulerian-Lagrangian model was used to model the steel-inclusions interaction and the Large Eddy Simulation (LES) model was used for the turbulence. The tracking of the dispersed phase was modelled taking into account the gravitational (F_G), buoyancy (F_B), drag (F_D), virtual mass (F_{VM}) and lift (F_L) forces according to the below equation:

$$m_i \frac{dv}{dt} = F_G + F_B + F_D + F_{VM} + F_L$$

where m_i and v refer to the mass and velocity of an inclusion, only 20 μm inclusions were modelled. Additionally, the effect of 4 different turbostops designs, with and inclined and tapered wall, and two filter’s designs, cubic and paddle, at 6 different positions were considered. A high angle tapered wall turbostop and a close to the inlet filter position showed the best results in inclusion’s removal. Both the active and reactive cleaning efficiencies increased with time, the active one reaching 80-90% efficiencies after 100 seconds, regardless of the turbostop type. These were much higher than the active cleaning efficiencies, showing the potential of CO bubbles generated at the filter to improve steel cleanliness.

In 2020, de Souza, Freitas and Tavares [21] evaluated the effect of a gas curtain in a Tundish and on the inclusions removal rate with physical and mathematical modelling, similarly to Aguilar-Rodriguez *et al.* [16]. The authors used the Aqueous Particle Sensor 3 probe (APS III) to count the inclusions leaving the system in their water physical model. For the mathematical modelling, the Eulerian-Eulerian multi-phase model was used to describe the water-air bubbles (average diameter of 2.75mm) system and the Eulerian-Lagrangian model (DPM) for the inclusion/particles trajectories. The standard k- ϵ turbulence model was applied for the turbulence field calculations and the drag force between the water and bubbles was taken into account via the Grace model. For the inclusions trajectories, only the drag force (F_D) was modelled and coupled with the discrete

random walk model. A novel boundary condition was established for the top free surface of the Tundish volume, not considering that all inclusions reaching the free surface will exit the system, as most of studies consider. A terminal velocity (v_t) is calculated for each particle size, based on a balance of the buoyancy (F_B) and drag (F_D) forces:

$$v_t = \frac{1}{18} d_p^2 g \frac{(\rho_l - \rho_p)}{\mu_l}$$

where d_p and ρ_p represent the particle diameter (ranging from 25-100 μm) and density; μ_l and ρ_l represent the fluid dynamic viscosity and density. If the relative velocity of a particle reaching the free surface is smaller than the terminal velocity, then the particle is trapped and exits the system, otherwise, the particle is then reflected and remains in the system. The mathematical results were in good agreement with the water experiments, proving the importance of an adequate free surface boundary condition for the inclusions elimination. As well, the gas curtain enhanced the inclusions removal index by redirecting the flow towards the surface, as observed by Aguilar-Rodriguez *et al.* [16] and presented in Figure 12.

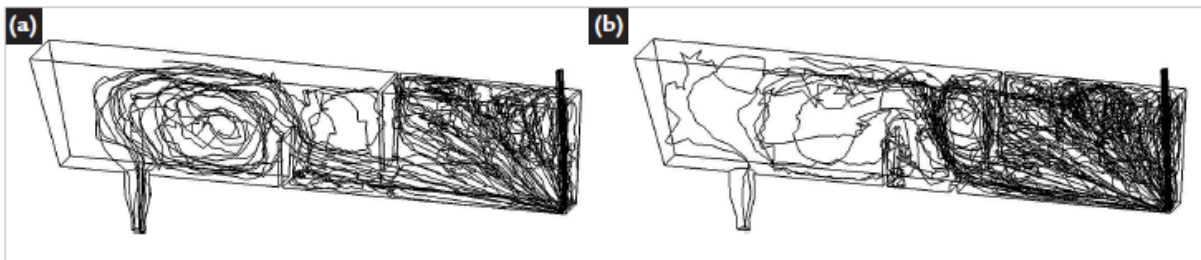


*Figure 12. Inclusions' (30 μm) trajectories (a) without gas curtain and (b) with gas curtain predicted by de Souza *et al.* [21].*

Following the same principle of gas bubbles as cleaning agent in the Tundish and its potential effect on other Tundish parameters (Heat loss, slag eye opening) and its corresponding mathematical modelling, in 2017 and 2021, Chang, Isac, Guthrie *et al.* [22, 23] confirmed the generation of small bubbles in water modelling and industrial tests. A multi-phase mathematical model was developed to study the phase interactions including the bubble size and distribution, namely the effect of the bubbles on the slag. The VOF, Standard k- ϵ Turbulence and DPM models were used to model the slag eye opening generated by the bubbles, the turbulence field, and the bubbles trajectories respectively. For the calculation of the bubbles trajectories, the gravitational (F_G), drag (F_D) and virtual mass (F_{VM}) forces were considered. The bubbles sizes were determined

a priori via water modelling experiments. In addition, the heat transfer equation was included to study the heat losses due to the slag eye opening, including heat radiation and convection. The study concluded that smaller bubble sizes (0.5 mm) disperse better and cover more upper volume of liquid steel in the Tundish (Figure 13), increasing the gases cleaning capacity, whilst lowering slag layer disturbances and attendant heat losses, versus the low dispersion of bigger bubbles, (5.0 mm), with their open eye slags, and higher heat losses, not to mention slag entrainment problems

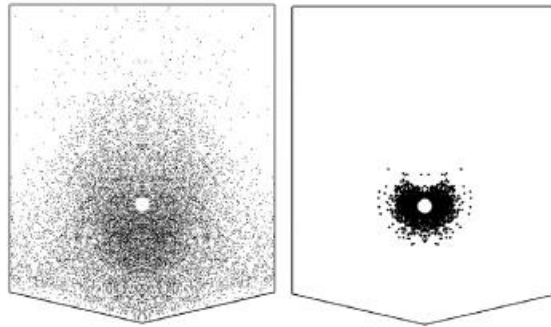


Figure 13. Bubbles distribution on a Tundish surface. Left 0.5 mm, right 5.0 mm. obtained by Chang et al. [22].

In 2021, Sheng and Chen [24] published a comprehensive study of the effect of several flow modifiers (weir, dam, turbostop and gas curtain) on the fluid flow considering heat transfer, as few models recently took into account the effect of FCD's on the temperature distribution. The realizable $k-\varepsilon$ model was used for the turbulence field calculation and the DPM was applied to model the gas curtain bubbles dynamics, including the same forces as Neumann *et al.* [19, 20] plus the turbulent dispersion (F_{TD}). The Boussinesq model was included to predict the natural convection flow. A tracer dispersion transport equation was used to obtain the RTD curves. As well, a half scale plexiglass water model was used to validate the mathematical model by comparing the RTD curves. The authors concluded that a turbostop, weir and gas curtain configuration will present the best inclusions removal rate based on the resulted RTD curve and that replacing the gas curtain with a dam will promote the lowest dead volume fraction. Regarding the heat loss, only around a 5 K temperature difference was found in the Tundish simulations.

A novel inclusion mathematical approach was recently reported by Gupta, Jha and Jain [25], in which they considered the generation of inclusions caused by erosion of the Tundish refractory. This is caused by high wall shear stresses (WSS) and can be controlled via three different designs of a turbulent inhibitor box (TIB). The TIB is similar to a turbo-stop. The author used the realizable

k- ϵ model and the DPM for the inclusion trajectories, including buoyancy (F_B) and drag (F_D) forces, plus the discrete random walk model. A standard trap boundary condition was considered for the inclusions reaching the top surface (slag) and a reflect boundary conditions for those inclusions touching the solid walls. The mathematical model was validated based on previous published experimental data. First, the high shear stress zones (HSSZ) were identified to be located on the system's walls, then the trajectories of inclusions (20-160 μm) generated from those zones were calculated, together with their removal rates. The highest HSSZ was detected to be on the bottom wall, immediately below the Ladle Shroud, making it the zone that was prone to the highest refractory erosion and therefore the most probable site for the generation of these inclusions. Additionally, other relatively HSSZ were detected on the vertical curved walls of the Tundish. Installing a TIB reduced the wall shear stress on the bottom wall, and on the other walls of the Tundish. The best results were for a TIB with an inward draft, but a TIB with a slight wall inclination presented the best removal rate for small inclusions ($<80 \mu\text{m}$). The comparison of the calculated wall shear stresses by Gupta *et al.* [25] without a TIB and with a TIB is presented in Figure 14. It can be observed that the maximum WSS values decreased for all cases with the use of a TIB and the HSSZ location changed for the curve and horizontal walls.

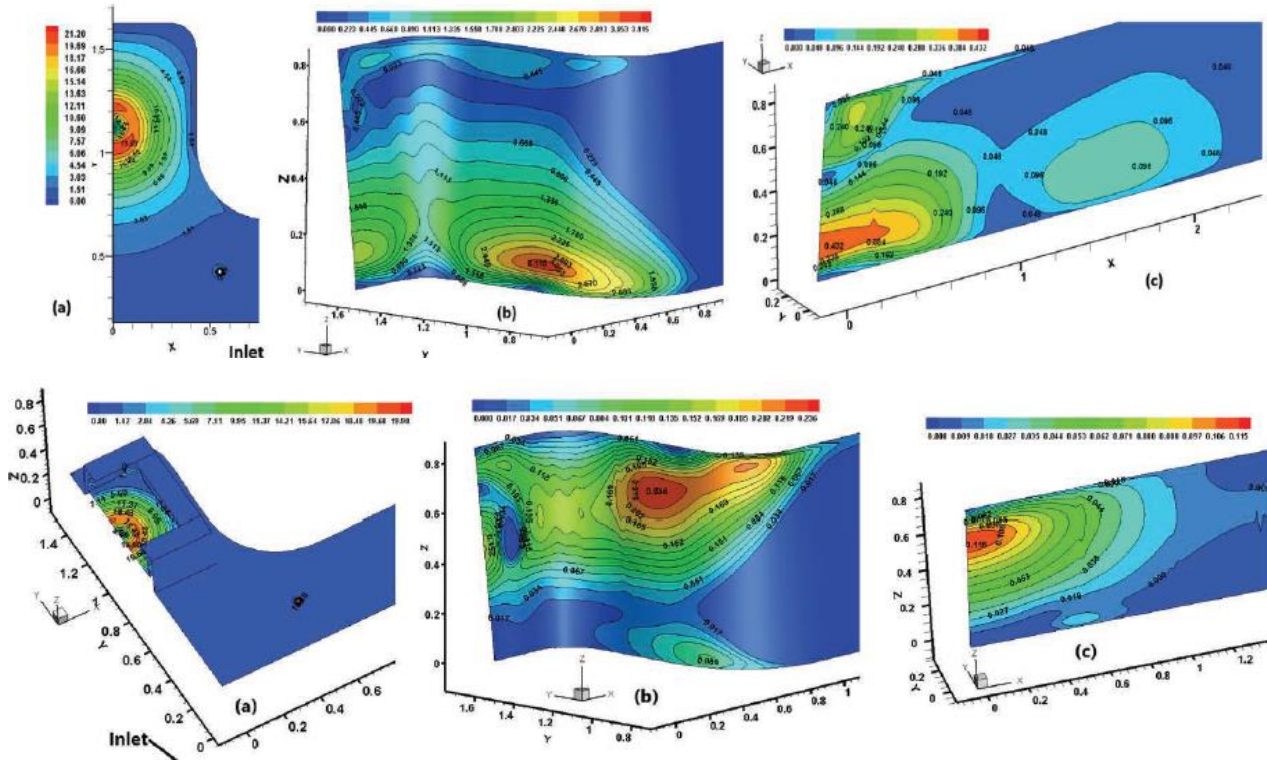


Figure 14. Wall shear stress contours on the tundish walls, (top) without a TIB, (bottom) with an inward draft TIB predicted by Gupta et al. [25].

Recently Gupta, Kumar and Singh [26] studied the effect of the flow variables in the formation of the vortex in the Tundish via physical and mathematical modelling. For the turbulence model, the authors chose the realizable $k-\epsilon$, based on previous research that recommends the realizable model over the standard $k-\epsilon$ since it can capture with more accuracy the fluid vortices and rotation as considers the mean square vorticity fluctuation in the dissipation rate (ϵ). For modelling the phases (water-air) interactions, the authors used the VOF model. 3 variables (inflow and outflow rate, and stagnation point) and its effect on the vortex formation were analysed in terms of the vortex initiation height. A proportional correlation was found mathematically between both the inflow and outflow rates with the vortex initiation height, as by increasing the flows, the height at which the vortex initiated increased too. The mathematical obtained heights were in good agreement with the experimental obtained values. In general, it was concluded that an increase in the turbulence (high inflow and outflow) in the Tundish will lead to an early formation of the vortex, pointing out the need to decrease said turbulence with flow modifiers (anti-vortex nozzles, dams etc.) to increases the Tundish productivity without promoting the vortex generation.

Huang, Chang, Zou *et al.* [27] performed a comparison between a conventional turbulence inhibitor and a swirling flow system in a Tundish, in terms of inclusions removal rates. A comparison of the two system is reproduced from the work of Huang *et al.* [27] in Figure 15. A swirling flow system aims to gather the small inclusions to the center of the swirling flow due to the centripetal force and the can coalesce and form large inclusions which can float up more easily due to its increases buoyancy.

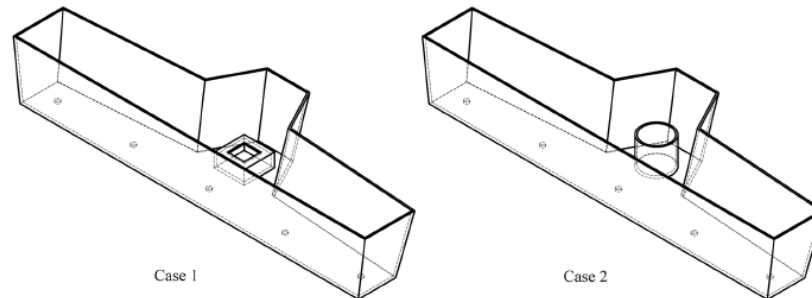
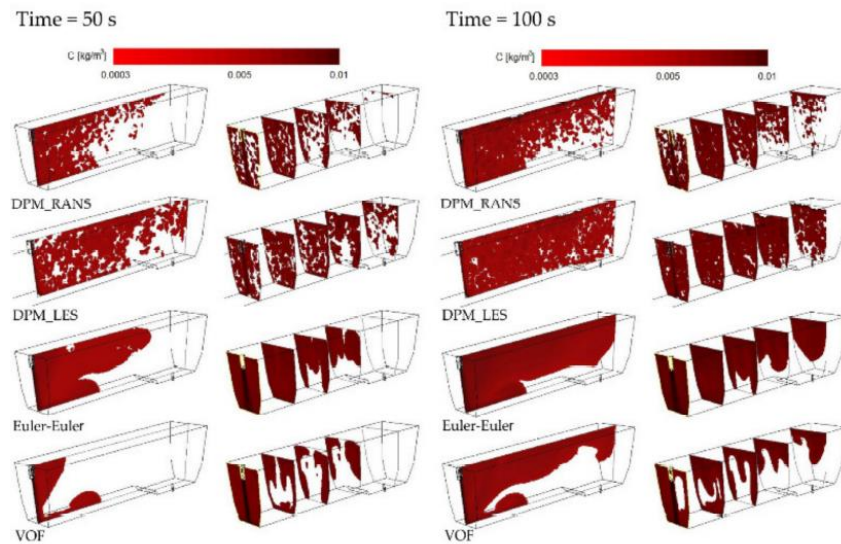


Figure 15. Case 1) Tundish with traditional turbulence inhibitor. Case 2) Tundish with swirling flow system. Taken from [27].

For the mathematical model, the Reynolds Stress Model (RSM) was used to model the turbulence field in the system and the Boussinesq model was taken into account to model the thermal convection effects on the fluid flow. RTD curves were obtained mathematically and confirmed with water model experiments. The authors found that a swirling flow system reduces in around 22% the dead volume in the studied Tundish, compared to the use of the traditional turbulence inhibitor, and similarly generates less variations in the RTD of the 5 strands of the Tundish. From complementary physical modelling experiments, it was found that the slag eye area can be reduced more than 80% by using a swirling flow chamber. However, the effect of the swirling flow chamber on the inclusions removal rate was not directly studied.

Merder, Pieprzyca, Warzecha *et al.* [28] recently published a comprehensive study of the models used to model mathematically a Tundish and inclusions behavior in a water-inclusions system, comparing different multi-phase and turbulence models with physical modelling results in a fourth scale Tundish water model, the inclusions were simulated with hollow glass spheres and counted in different laser planes with the Klotz particle counter. The authors analyzed the DPM-LES, DPM-RANS, VOF and Euler-Euler multiphase models by comparing different particles sizes (20,50, 100 and 140 μm) contours at different planes and times, as shown in Figure 16 for 20 μm particles. Initially, an important difference was noticed on the VOF model, so it was discarded

initially as an accurate model for the fluid-particles interactions. The remaining models presented bigger differences at longer times regarding the particles' distribution on the different planes. The particles distribution contours were compared with the laser particles images at different times to assess the model with the better results qualitatively, a comparison for the 20 μm obtained by Merder *et al.* [28] can be observed in Figure 16. Consistently, the DPM-RANS model presented more similarities with the experimental results for different particles sizes and different times and similarly the Euler-Euler presented the second-best qualitative results. For a quantitatively analysis, the authors compared particles concentration curves obtained mathematically and experimentally, finding good correlation between the results and bigger variations for big (100-120 μm) particles. It was concluded that the DPM-RANS (Standard k- ϵ) model reflects the inclusions empirical distribution with the most accuracy.



*Figure 16. 20 μm particles contours maps on different planes and at different times for different models calculated by Merder *et al.* [28].*

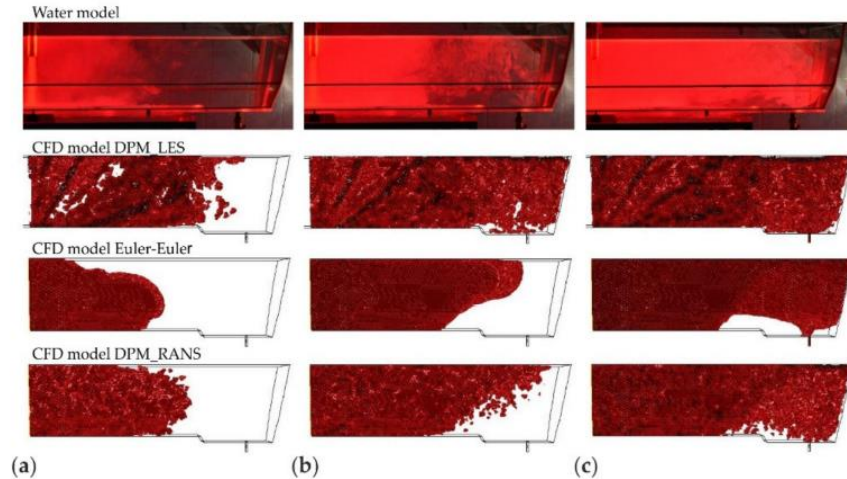


Figure 17. 20 μm particles contours for different mathematical models and the water model at different times (a) 25, (b) 60 and (c) 120 seconds, calculated by Merder *et al.* [28]].

Patil and Viswanathan [29] analyzed the effect of a non-isothermal Tundish on the inclusions transport. The author used the Boussinesq approximation to model the density variations due to temperature gradients, the standard $k-\epsilon$ turbulence model and the DPM to calculate the inclusions trajectories considering the drag (Morsi and Alexander drag coefficient) and buoyancy forces. A stochastic tracking model was included to consider the effect of the particle's dispersion due to the fluid turbulence. RTD curves were calculated via the mass transport equation. The mathematical model was validated with previously published water modelling results finding a good correlation with the RTD curves and the inclusions removal rates. The mathematical model was applied to an industrial Tundish, and the authors analyzed the effect of two weirs on the RTD curves, the inclusions removal rate, and the temperature gradients, reaching to the conclusion that the tall weir (635 mm) enhances the inclusions removal rate, increases the RTD and decreases the heat losses compared to a Tundish without a weir.

Recently, in 2021 Xu, Ling, Wang *et al.* [30] investigated the effects of the Tundish cover powder and the ladle-change over on the Tundish air ingress and TOE (Tundish Open Eye). For the mathematical model, no details of the turbulence model were disclosed by the authors. The VOF model was used to predict the phases interactions and an additional term (\vec{F}) was added to the momentum equation to model the interfacial tensions between the three phases (steel-slag-air) and the superficial force is transformed into a volume force via the divergence theorem resulting in:

$$\vec{F} = \sum_{i < j}^3 2\sigma_{ij} \frac{\alpha_i \rho_i k_i \nabla \alpha_j + \alpha_j \rho_j k_j \nabla \alpha_i}{\rho_i + \rho_j}$$

α_i , ρ_i and k_i correspond to the volume fraction, density, and turbulence kinetic energy of each phase. σ_{ij} is the interfacial tensions between the phases and is defined as below:

$$\sigma_{ij} = (\sigma_i^2 + \sigma_j^2 - 2\sigma_i \sigma_j \cos\theta)^{1/2}$$

σ_i , is the surface tensions of each phase and θ is the contact angle between the phases. The model was validated by comparing the TOE with a half scale water-oil model. The authors calculated time dependent phase contours of the air and slag during ladle change over to assess its effect on the air and slag behaviors, which are presented in Figure 18.

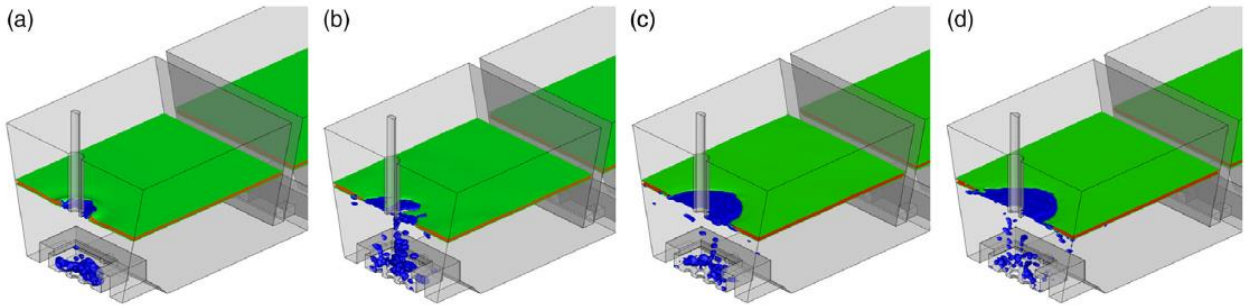


Figure 18. Slag (green) and air (blue) phase distributions at (a) 0.5, (b) 2, (c) 5, and 15 seconds calculated by Xu *et al.* [30].

Based on the results obtained, it was concluded that reoxidation will occur during ladle-change over via the air ingestion through the Ladle Shroud and the exposure of the steel due to the formation of the TOE. Specific times for the mentioned processes were calculated by Xu *et al.* [30]. As well critical velocities of slag entrainment were calculated via the Capillary number (Ca) and the critical Capillary number (Ca*) defined as:

$$Ca = \frac{V_{steel} \mu_{steel}}{\sigma_{steel-slag}}$$

$$Ca^* = 3 \times 10^{-6} \times \frac{v_{slag}}{v_{steel}} + 2.8 \times 10^{-3}$$

where μ_{steel} and $\sigma_{steel-slag}$ correspond to the dynamic viscosity of steel and the surface tension between the phases; v_{phase} correspond to the kinematic viscosity of each phase and V_{steel} indicates

the tangential velocity of the steel at the interface. As a solution, a simulation increasing the refilling time was performed. As conclusion, the authors recommended to increase the refilling/ladle-change over time since it will decrease the TOE area and the V_{steel} thereby minimizing slag entrainment and ultimately, increasing the steel quality.

In Table 1.3, a summary of the main mathematical models for the Tundish is presented. Indicating the main characteristics of each model.

Table 1.3: Summary of the Tundish mathematical models of the past 5 years

	Tundish Type	Multiphase	Thermal	Flow modifier	Turbulence Model	Time	Inclusion tracking
Chen et al. 2016 [13]	1 Strand	Slag as stationary wall	No	Weir and Dam	Chem-Kim k- ϵ	Transient	Yes, Eulerian frame, turoporetic model
Ni et al. 2017 [14]	1 strand, swirling SEN	Slag as stationary wall	No	Weir, dam and swirling SEN	Realizable k- ϵ	Transient	Yes, DPM, Stokes numer
Cwundzinski 2017 [15]	1 strand, gas curtain	No slag, gas bubble trajectories DPM	Yes	Gas curtain middle, argon	Realizable k- ϵ	Transient	No
Aguilar-Rodriguez et al. 2018 [16]	1 strand, gas curtain	VOF (argon-melt-slag)	No	Gas curtain	Standard k- ϵ	Transient	Yes, Lagrangian DPM with radom walk model.
Chattarjee et al. 2018 [17]	2 strands	VOF (melt-slag) DPM (gas bubbles-liquid)	No	Ladle Shroud gas injection	Standard k- ϵ	Transient	No
Mishra and Mazumdar 2019 [18]	1 Strand (delta, T and	Single-phase	No	Turbostop	Standard k- ϵ	Steady	No

	rectangular-shaped)						
Neumann et al. 2020 [19,20]	2 Strand	Single-phase	No	Turbostop	LES	Transient	Yes, Eulerian-Lagrangian with phase interactions
de Souza et al. 2020 [21]	1 Strand	Eulerian (gas-liquid)	No	Weir, Dam and gas curtain	Standard k-ε	Steady	Yes, Eulerian-Lagrangian and terminal velocity
Chang, S. et al. 2021 [22, 23]	4 Strand	VOF (gas-steel-slag)	Yes	Gas injection	Standard k-ε	Steady	Yes, Lagrangian DPM with phase interactions
Sheng and Chen 2021 [24]	1 Strand	Single-phase	Yes	Turbostop, Weir, Dam and gas curtain	Realizable k-ε	Steady	Yes, Lagrangian DPM with phase interactions, including turbulent dispersion.
Gupta et al. 2021 [25]	6 Strand	Single-phase	No	TIM/Turbostop	Realizable k-ε	Steady	Yes, Lagrangian DPM with random walk model.
Gupta et al. 2021 [26]	2 Strand	VOF (water-air)	No	No	Realizable k-ε	Transient	No
Huang et al. 2021 [27]	5 Strand	Single-phase	Yes	Turbostop, swirling flow chamber	Reynolds Stress Model	Steady	No

Merder et al. 2021 [28]	2 Strand	Single fluid phase	No	No	LES and Standard k-ε	Transient	Yes, modeled as DPM, VOF and Euler-Euler
Patil and Viswanathan 2021 [29]	1 Strand	Single-phase	Yes	Weir, dam and turbostop	Standard k-ε	Transient	Yes, DPM, drag and buoyancy forces, stochastic tracking model
Xu et al. 2021 [30]	2 Strands	VOF (steel-slag-air)	No	Weir, dam and turbostop	Not disclosed	Transient	No
Mazumdar 2019 [12]	3 Strand Bloom	VOF (liquid-gas)	Yes	Argon Ladle Shroud	Standard k-ε	Transient	No

1.4.- Ladle Shroud; an important Tundish flow control device.

The importance of the Ladle Shroud (LS) has been commented previously, being a key component to avoid the molten steel re-oxidation and recently has become a multi-function device in “Tundish metallurgy”, besides from only being the connection between the ladle and the Tundish. A general schematic of the ladle-LS-Tundish system is presented in Figure 19.

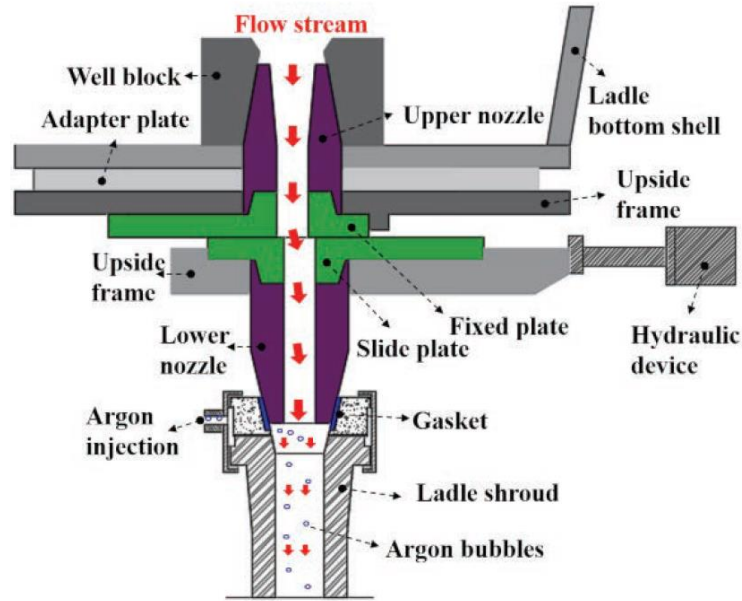


Figure 19. Schematic of the ladle-LS-Tundish system. Taken from [31].

In recent decades, the LS has been studied as a potential flow control device, as the incoming flow from the Ladle determines the fluid dynamics characteristics of the Tundish and several LS designs have been proposed to optimize the incoming flow. Zhang, Qing, Yang *et al.* [31] published in 2019 a review on the LS as a functional device in the Tundish, summarizing the main roles of the LS and its more recent advances:

1. *Shrouding/protecting the incoming steel stream from the ladle.*

Two main ways to shield the ladle incoming stream are commented, inert gas (usually Argon) shrouding and mechanical shrouding with a refractory LS, being the latter the most usual. However, mechanical shrouding not always protects completely the steel stream from the air, due to the potential crevices between the connection of the lower nozzle and the LS, as presented in Figure 20 (a). As result, the use of argon injection or/and a gasket is mandatory to avoid any air leakage into the shroud. Figure 20 (b) shows some methods combinations to ensure effective shrouding.

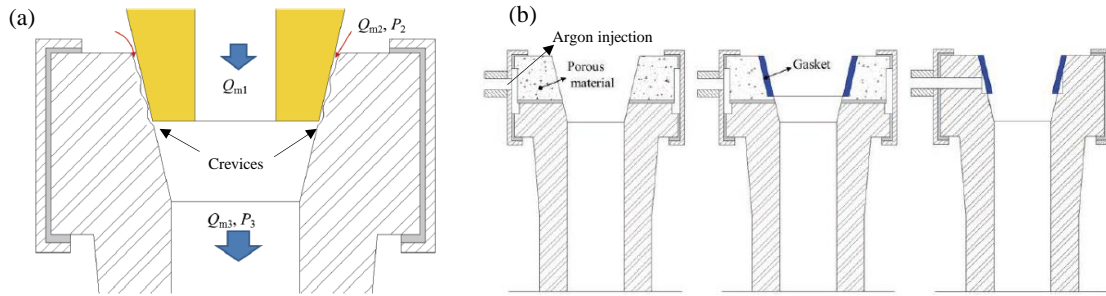


Figure 20. (a) Crevices between lower nozzle and LS. (b) Methods for effective shrouding. Taken and adapted from [31].

As well, Zhang *et al.* [31] comment on the importance of correct LS alignment and maintenance methods to increase LS lifetime.

2. Act as a flow control device (FCD).

The LS has been proposed as an effective FCD, with the possibility to replace the traditional weirs and dams. The LS geometry can determine the fluid dynamics mainly in the entry zone of the Tundish and some innovative designs used in the industry are discussed, CLS (Conic-shaped Ladle Shroud) and TLS (Trumpet-shaped Ladle Shroud) types I and II, shown in Figure 21.

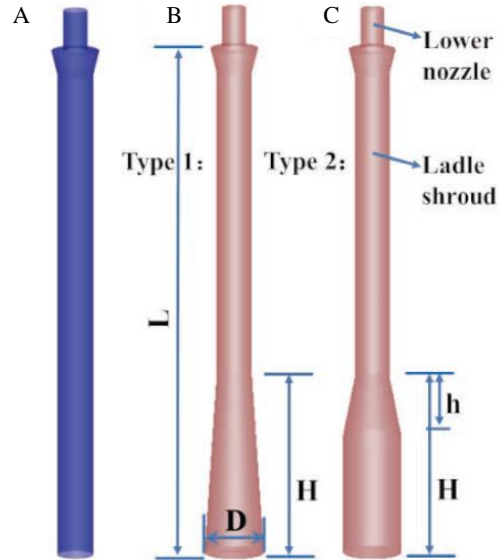


Figure 21. LS shroud designs. A) CLS. B) TLS type I. C) TLS type II

Several advantages of the TLS against the CLS geometries are commented on e.g., the TLS reduces nozzle clogging and production disruptions and decreases incoming turbulence

into the Tundish leading to less slag entrainment. The TLS outlet stream velocity decreases due to the outlet increasing diameter, generating the mentioned improvements. Additionally, the TLS promotes a calm Tundish bath and more stability in transient operations. Some other innovative LS designs under exploration are summarized, but the authors commented that its use is limited to scale without industrial validation.

Argon injection role in the LS is commented on as well, not only as a shrouding agent but also as multi-phase flow modifier. Small bubbles can be generated via Argon injection, and several recent studies have obtained the bubble sizes in some systems, e.g., water-air and steel-argon, ranging in size from 0.5mm to 5.0 mm, depending mainly on the gas inflow rate. Argon injection can be used as a steel cleanliness agent, since small inclusions (<50 μm) can be attached to small gas bubbles and be eliminated. However, its industrial application is still pending. On the other hand, argon injection can promote the formation of a TOE (Tundish Open Eye), which can be detrimental to steel quality, as the exposed steel melt causes re-oxidation. Some mathematical modelling efforts have focused on the effect of the argon injection rate on the TOE in a steel-gas-slag system.

3. *Ladle-slag carry over detection.*

It is essential for steel cleanliness to avoid the carry-over of ladle-slag through the LS, and some slag detection methods in the LS are mentioned by Zhang *et al.* [31] e.g., electromagnetic detection, weight monitoring, optical and supersonic detection.

1.4.1. Ladle Shroud mathematical and physical modelling; a review of the last 5 years

Over the last five years, some research efforts have focused on a better understanding of the two-phase (argon-steel) flow generated in the Ladle Shroud via mathematical and physical modelling. In 2018, Mazumdar, Singh and Tiwari [32], addressed the use of the DPM model approach to model correctly the two-phase flow within the Ladle Shroud. The DPM model initially assumes a bubbly flow with a gas volume fraction of around 10%. However, based on usual industrial argon flows, the volume fraction can be up to 25% [31]. Therefore, the DPM model can underestimate the effect of a gas phase in the Ladle Shroud. To evaluate the effect of a low (5%) and high (15%) gas flow rate ratio (Q_g/Q_l) in the Ladle Shroud flow, water physical modelling was done, finding

that a low one, generates a bubbly liquid flow, in contrast a high gas flow rate which causes a liquid free jet to eventually collapse into a turbulent gas-liquid mixing zone, proving the limitation of the DPM approach in predicting the biphasic fluid flow except for very low gas flow rates, rarely found in industry. Additionally, the oversimplification of the gas injection configuration in most physical models was discussed, as it is necessary to accurately capture the shroud gas distribution. An alternative approach to the DPM was presented by Singh, Mazumdar, Tiwari and Dutta [33], using instead the VOF model and the results were validated with water model experiments. The standard $k-\epsilon$ turbulence model was used to model the fluid flow in transient state (until reaching a quasi-steady state) with velocity boundary condition at the gas and liquid inlets and a pressure outlet condition at the free surface. The experimental and mathematically predicted free liquid jet lengths, presented good agreement, validating the developed mathematical model.

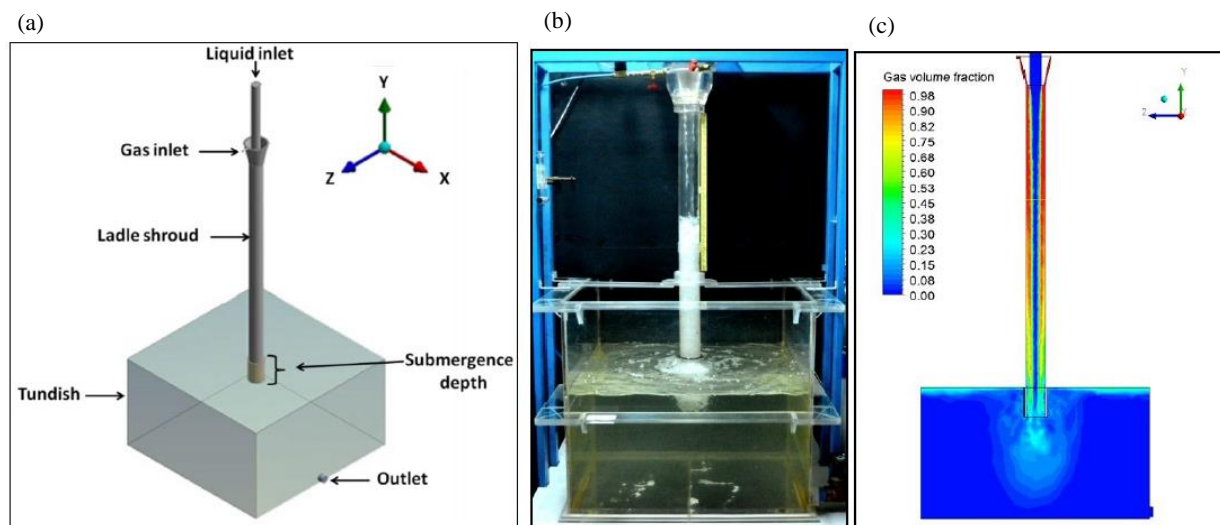


Figure 22. (a) Geometry configuration and boundary conditions. (b) Flow characteristics observed in water modelling. (c) Flow characteristics in mathematical modelling. Taken and adapted from [33].

In 2018, Zhang, Yang, Li *et al.* [34] studied the effects of a dissipative Ladle Shroud (DLS) in a Tundish with mathematical and experimental modelling. The objective of the DLS is to decrease turbulence in the entering flow, and thereby reduce turbulence within the complete LS-Tundish system. The effects of said shroud on the mixing phenomena in a Tundish were studied in detail. For the mathematical modelling, the authors used the LES model to predict turbulence within the DLS with a special treatment near the walls using the Wall-Adapting local Eddy-Viscosity (WALE) approach, suitable for complex geometries as in the DLS. The transient mass transport equation was used in order to predict transient tracer concentrations at each time step and location.

The mathematical model was validated with a 1:1 scale water model of the DLS. Simulation results were in good agreement with the ink tracer images obtained experimentally. A comparison between a conventional LS and the DLS was made mathematically. The DLS generates more vortices and velocity variations in the radial and longitudinal directions, which can greatly enhance mass transfer and intermixing within the Ladle Shroud, prior to entry into the Tundish. The effect of the DLS was analyzed experimentally using a one third scale and also for a full scale Tundish via RTD. It was found that the fluid mixing is improved better in the small Tundish, compared with that for a full scale Tundish.

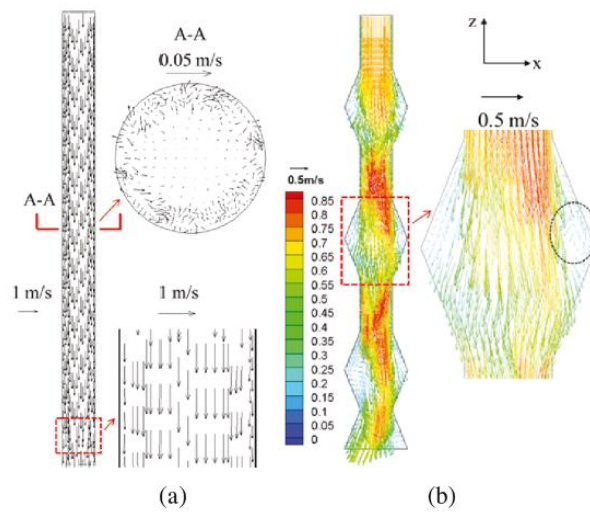


Figure 23. Velocity profiles for (a) conventional LS and (b) DLS predicted by Zhang et al. [34].

In 2018, Singh and Mazumdar [35] published a comprehensive water modelling analysis of the two-phase Ladle Shroud systems and the effect of several variables e.g., nozzle and shroud diameters, shroud gas flow, and specially the gas to liquid flow ratio (Q_g/Q_l), on the flow characteristic within the Ladle Shroud. Two full-scale water models (for bloom and slab casting) were used for the experiments. The flow rates for the steel-water were equal and for the air-argon flow the rate was equal to the specified argon flow at 1873 K and 1 atm and the slide gate was fully opened in all experiments. The used water models and the schematic for the bloom casting system can be seen in Figure 24.

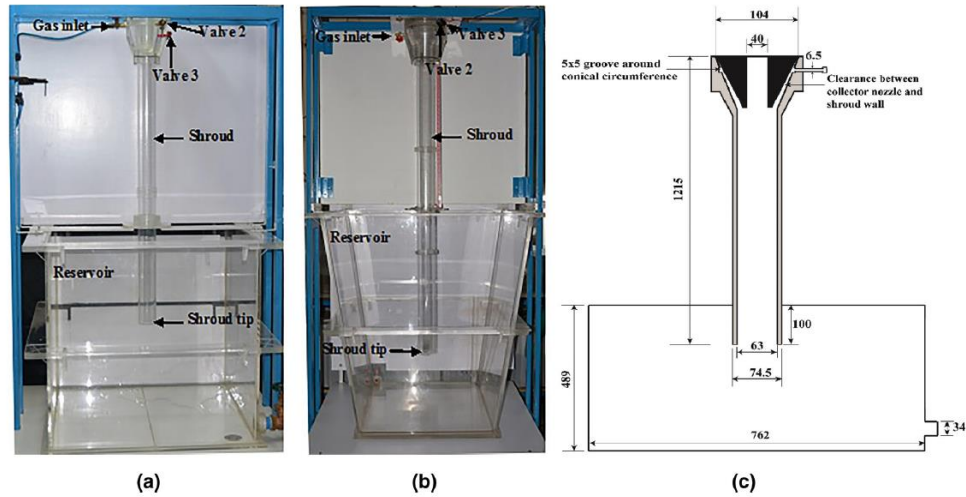


Figure 24. Full-scale Ladle Shroud water model for system for (a) bloom casting, (b) slab casting and (c) schematic of the bloom casting system. Taken from [35].

Depending on the gas to liquid flow ratio (Q_g/Q_l) three general flow regimes were observed experimentally by Singh and Mazumdar [35]. These are summarized in Figure 25. For $Q_g/Q_l=0.02$, Fig. 25 (a), a bubbly flow regime between the gas and the liquid is developed, then for a $Q_g/Q_l=0.3$, Fig. 25 (b), two distinctive regions are generated, a free liquid jet in the upper Ladle Shroud part and a bubbly mixing zone in the lower part. Finally, with a $Q_g/Q_l=0.42$, Fig. 25 (c), the free jet extends complete within the Ladle Shroud and the turbulent mixing zone initiates at the entrance to the Tundish.

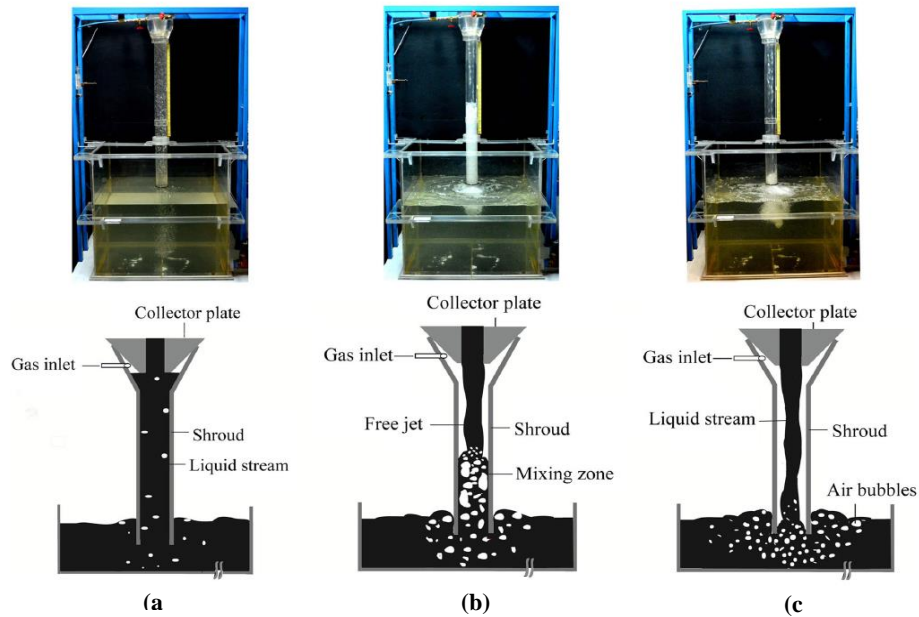


Figure 25. Two-phase flow regimes observed at different gas to liquid flow ratios, (a) $Q_g/Q_l = 0.02$, bubbly regime, (b) $Q_g/Q_l = 0.3$ partial free liquid jet and (c) $Q_g/Q_l = 0.42$, complete free liquid jet. Taken from [35].

Additionally, the authors simulated potential air ingress on the collector nozzle-shroud wall connection, see Figure 24 (c), by connecting two of the three valves to manometers at ambient pressure under the different operating conditions and measuring the manometer arm differences ($+\Delta h$: air ingress; $-\Delta h$: air egression). For the different simulated gas to liquid flow ratios, it was found that air ingress can be avoided provided $Q_g/Q_l > 0.30$ for a submerged Ladle Shroud and $Q_g/Q_l > 0.42$ for a non-submerged Ladle Shroud. As such, the need to effectively shroud the ladle incoming steel flow with sufficient inert gas flow rate was confirmed and a threshold ratio was determined experimentally.

In 2019, Singh and Mazumdar [36] used the VOF multi-phase model, similarly to the work presented in [33] to predict the steel-argon flow within the Ladle Shroud and compare with the previously published experimental results [35]. The model was validated extensively with experimental measurements and the authors were able to present a correlation to predict the free jet length and the required gas flow rate to prevent air ingress. To model the turbulence flow field, the realizable $k-\epsilon$ model was used and the surface tension force (F_σ) was added into the momentum equation as an extra term. The mathematical model results were compared with the water modelling experiments, shown on Figure 26, where two regimes were observed. In Figure 26 (a) and (b), with a low gas to liquid flow ($Q_g/Q_l = 0.025$) a bubbly regime is observed, whereas

in Figure 26 (c) and (d), where a higher gas to liquid flow ($Q_g/Q_l=0.2$) is achieved, the free steel jet regime is achieved. A gas liquid flow ratio of around $Q_g/Q_l=0.4$ is needed to prevent any air ingestion, as found by the same authors in reference [35], where a full free jet will be achieved within the Ladle Shroud.

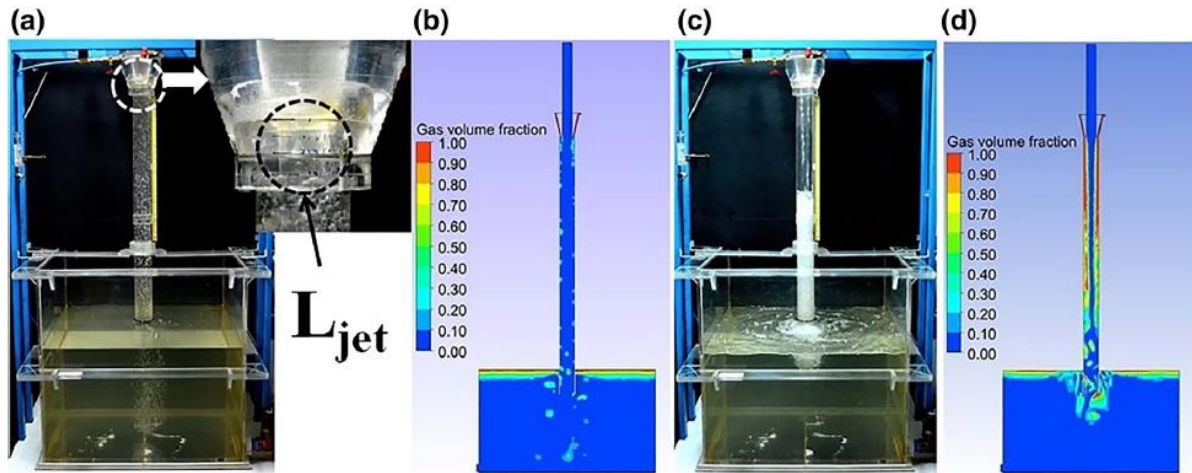


Figure 26. Two phase flows within a Ladle Shroud in (a) a full-scale water model and (b) its corresponding predicted gas volume fraction with $Q_g/Q_l=0.025$; (c) a full-scale water model and (d) its corresponding predicted gas volume fraction with $Q_g/Q_l=0.2$. Taken from [36].

In 2019 Zhang, Fang, Deng *et al.* [37] published an analysis of the effect of two different trumpet shaped Ladle Shrouds (LS2 and LS3) on the multi-phase fluid flow of a five-strand Tundish through mathematical and physical modelling. A conventional Ladle Shroud (LS1) was taken into account too for comparison. The analysis was made considering steady state casting and ladle change over, namely transient state. Additionally, the effect of two types of turbostops on the flow behavior was addressed. The authors used the standard $k-\epsilon$ turbulence model to predict the turbulence in the Tundish and the VOF model was applied to model the steel-slag-air interactions. An additional term (\vec{F}) was added to the momentum equation to model the interfacial tensions between the three phases similarly as in [30]. The mathematical results were validated with a one third scale water model. It was found, that by increasing the inner exit diameter of the Ladle Shroud, the turbulence near the slag-steel interface was reduced, meaning that less slag entrainment will be possible. Turbulence contours of the three cases from [37] are presented in Figure 27.

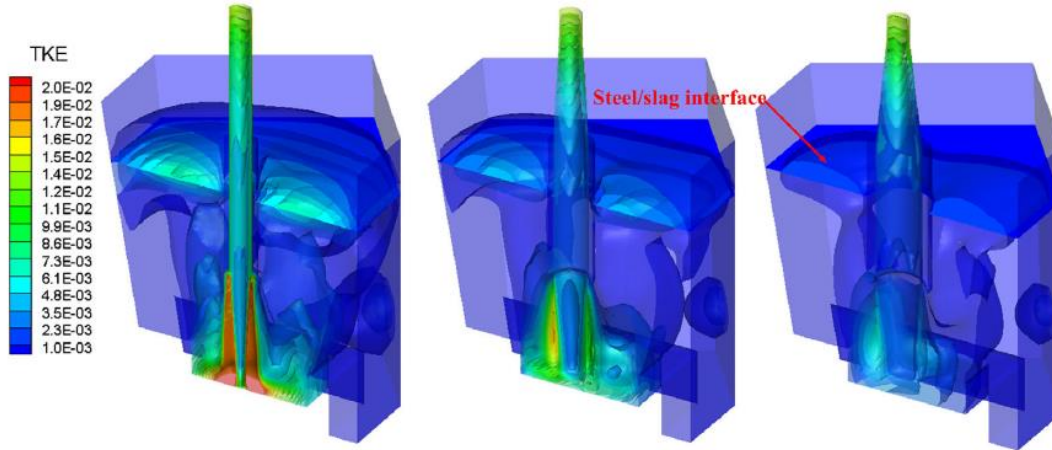


Figure 27. Turbulence kinetic energy contours for 3 different Ladle Shrouds designs obtained by Zhang et al. [37].

The effect of the Ladle Shroud design during ladle-change over, meaning the inlet flow is twice the steady state flow, was analyzed by obtaining air volume fraction contours of the air displaced by the incoming steel. The results can be observed in Figure 28, where the air exits the Ladle Shroud-Tundish system sooner in the conventional Ladle Shroud compared to both trumpet shaped Ladle Shrouds, since the inner volume of the trumpet Ladle Shrouds is bigger and will contain more air when empty.

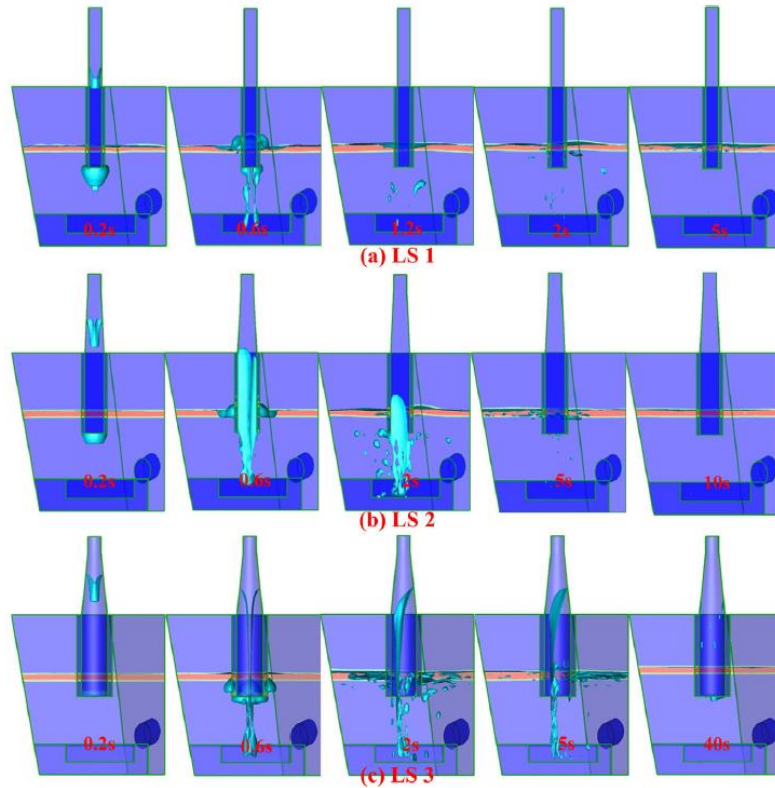


Figure 28. Air volume fraction contour (light blue) during ladle-change over for (a) LS1, (b) LS2, exiting diameter= $1.5 \cdot DLS1$ and (c) LS3, exiting diameter= $2 \cdot DLS1$ obtained by Zhang et al. [37].

Additionally, the effect of each Ladle Shroud on the Tundish Open Eye (TOE) was discussed, resulting in the greatest TOE with LS1 and in the smallest with LS3. The authors concluded that a trumpet shaped Ladle Shroud will decrease the incoming turbulence into the Tundish reducing the potential slag entrainment and the TOE area during steady state and ladle-change over stages. As well the authors recommended a circular shaped Turbostop since it reduced more the turbulence in the system with LS2 and LS3 compared the use of a quadratic Turbostop, since it reduced more turbulence in the system with LS2 and LS3 as compared with the use of a rectangular Turbostop,

Chapter 2: Methodology

2.1 Mathematical modelling

Based on the presented literature review, a novel 3D transient-state multiphase model was developed and improved in comparison to others presented, to predict and analyze for the first time some transient phenomena in the Ladle Shroud-Tundish system e.g., start-up operation, steel-air-argon interactions, and air suction. Mathematical modelling, being and discussed to be a useful tool to study the Ladle Shroud-Tundish system, was performed to analyze firstly the current Ladle Shroud used in real industrial process to produce steel powders. The CFD ANSYS-Fluent version 19.0 was used to solve the mathematical model. All the process parameters and details and sketches of the process were provided by the industrial company during private communications and meetings following a non-disclosure policy and agreement. To develop a tailored mathematical modeling the ANSYS Workbench© [38] software package was used, and the general steps are depicted in Figure 29 and summarized below, a detail description of each step will be presented in the following subchapters:

1. Geometry generation in SpaceClaim©: SpaceClaim© is a CAD software part of the ANSYS Workbench software package and it was used to generate the detailed geometries and volumes to discretize and then solve the transport equations further on. SpaceClaim© geometries were generated for the Tundish, Ladle Shroud, turnflow and for the anti-vortex nozzles.
2. Meshing in ANSYS Mesh©: After the generating the CAD geometries, the files are exported to the software ANSYS Mesh©, part of the ANSYS Workbench software package, to perform the media discretization in finite elements for tis subsequent solution via the Volume of Fluid numerical method. Additionally, the boundary conditions surfaces are named and defined, e.g., inlet, outlet, walls, which details will be discussed further on.
3. Set up equations, materials properties, and boundary conditions in ANSYS Fluent©: In ANSYS Fluent version 19.0, the details of the mathematical model are specified, namely, transient state, multi-phase, turbulence models, etc. As well the materials are selected from an including database with all required properties, e.g., viscosity, density, etc. or these can be defined to create materials not included. The boundary conditions are defined by type, like velocity inlet, pressure outlet, etc. After setting up all the required parameters, the

solution is initialized, and the calculations are performed by the CFD to solve the predicted flow field.

4. Results visualization: After calculating the solution and reach convergence, the results can be visualized directly in ANSYS Fluent© or export the resulted files to ANSYS Results© to generate magnitudes contours, vectors maps, flow trajectories or animations for analysis.

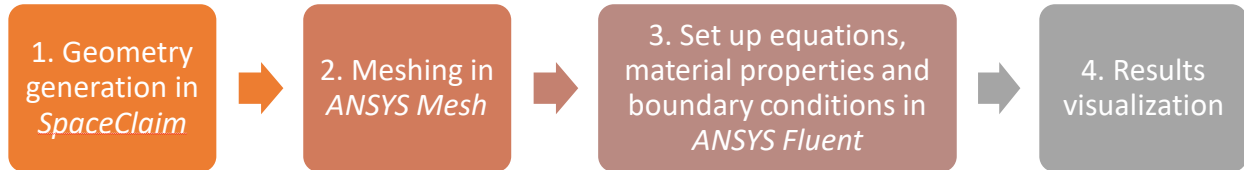


Figure 29. Process followed for the mathematical modelling

2.1.1 Geometry generation

All the detailed technical sketches of all the involved parts for the mathematical study, were provided by RTMP and several revisions of the sketches were done to generate an accurate representation of the Ladle Shroud-Tundish system. The CAD geometries were generated in SpaceClaim©, firstly drawing two dimensions sketches, an example of the Tundish is presented in Figure 31, for then perform the three-dimension Boolean operations, e.g., pull, match, chamfer, etc. [38]. The side, top and isometric view of the Tundish geometry generated in SpaceClaim are show in Figures 30, 31 and 32 respectively.

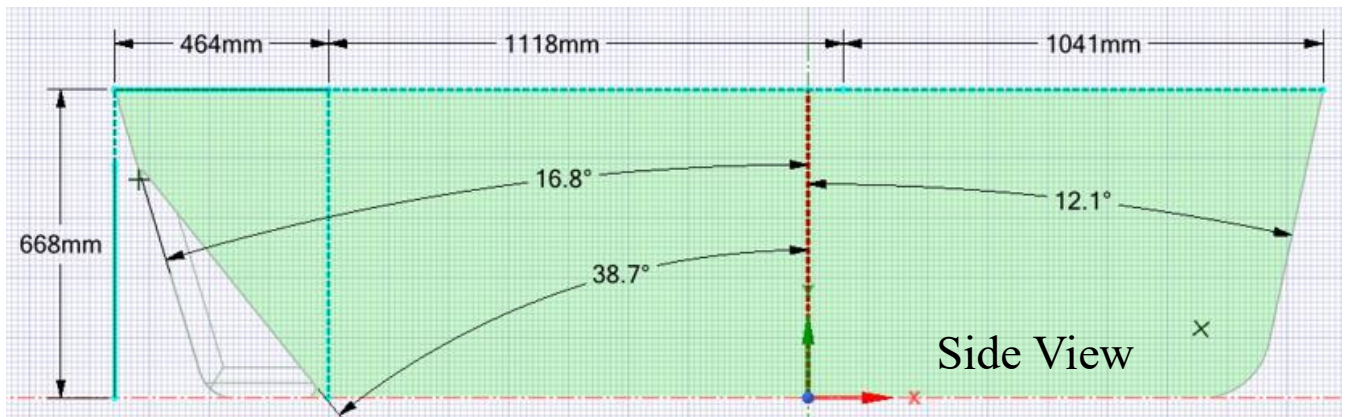


Figure 30. Tundish geometry generated in SpaceClaim©. Side view.

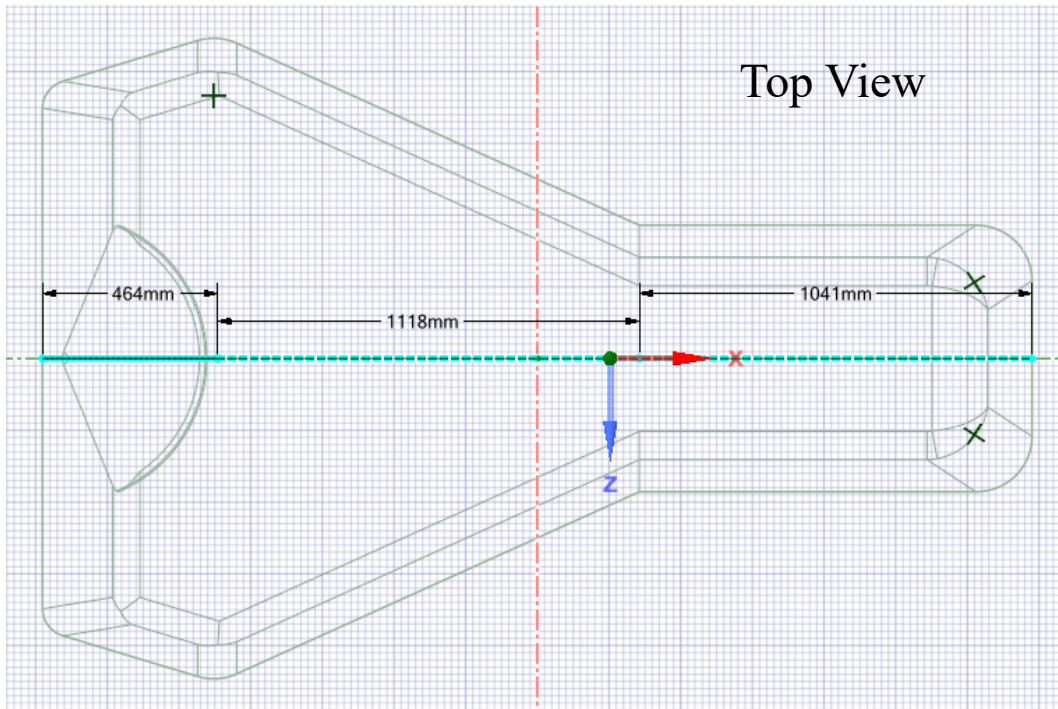


Figure 31. Tundish geometry generated in SpaceClaim©. Top view.

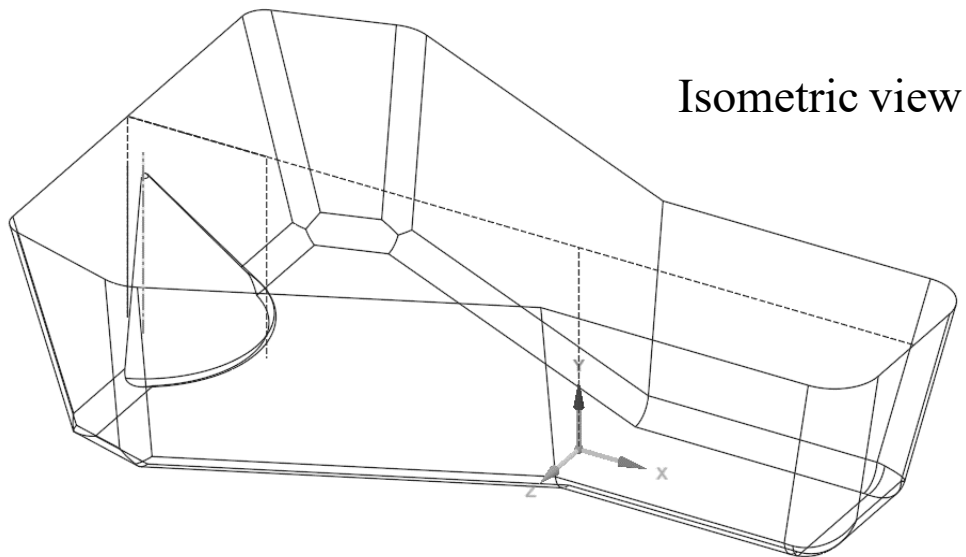


Figure 32. Tundish geometry generated in SpaceClaim©. Isometric view.

For the Ladle Shroud, a detailed interpretation and consultation with RTMP had to be done for the ladle upper nozzle and Ladle Shroud connection, as well as for the argon injection configuration. A summary of the most important dimensions and the geometry development can be observed in

Figure 33. One of the two main features of the Ladle Shroud (LS) are the changing Inner Diameters (ID's) from 50 to 65 and then to 75 mm at the bottom part, making it a diverging LS, to be called as such henceforward. The main goal of the LS design is to reduce the exiting flow velocity from the LS into the Tundish to reduce the incoming turbulence and therefore potential splashing, a less drastic design to the trumpet shape LS discussed by Zhang et. al., [31] and analyzed via mathematical modelling [37], which is becoming a common type of LS used in Steelmaking [31]. The other important feature of the present LS, shown in Figure 33, is the argon shrouding configuration, where the argon is injected through a nozzle and distributed in a 1.2 mm thick ring and then goes through a 10 mm thick, porous refractory for homogenous argon distribution. Due to the relevance of the LS design, during the development of its CAD geometry and details, it was decided to perform a comprehensive analysis of the current LS as a first step into modelling the sources of inclusions for the present project, and to be discussed in the next chapters.

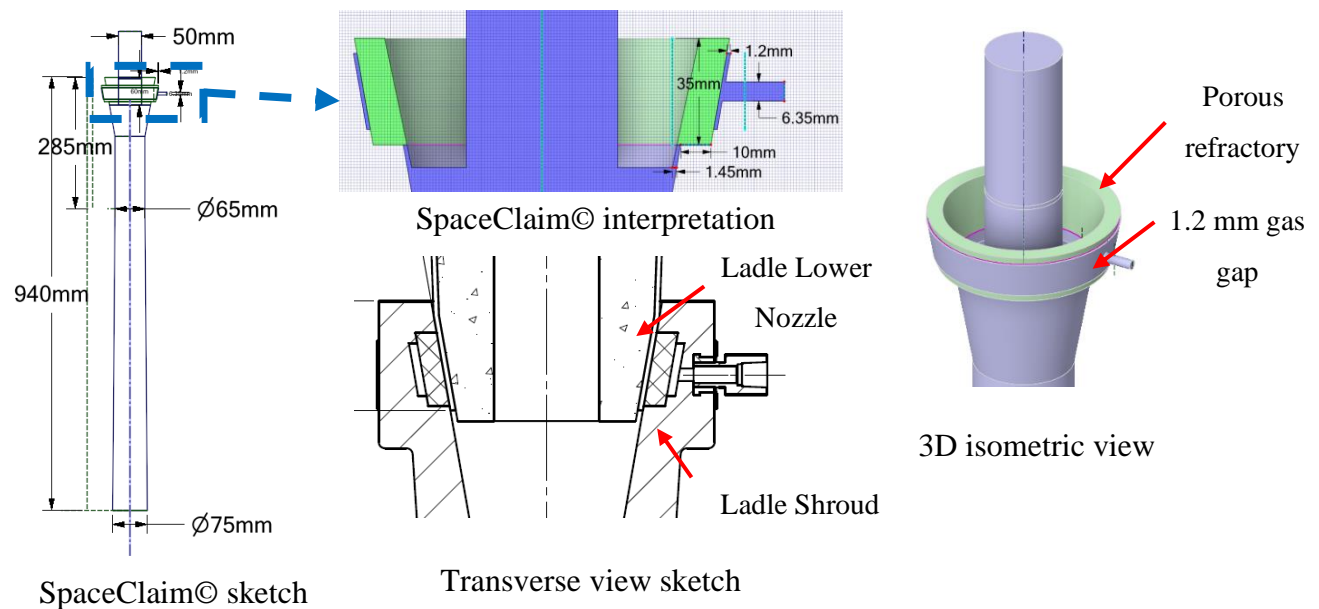


Figure 33. Ladle Shroud geometry generated in SpaceClaim.

The current turnflow being used at RTMP, is presented in Figure 34, and its main objective is to reduce the Tundish inner refractory erosion walls in the entering zone and to redirect the incoming flow to the surface to enhance the NMI's flotation and removal. In Figure 34 the generated geometry in SpaceClaim is depicted in a top and side view. The anti-vortex nozzle was generated similarly, and shown in Figure 35, its main feature being the ID of the bottom exiting zone, which can be of 18 and 16.5 mm depending on steel flow rate.

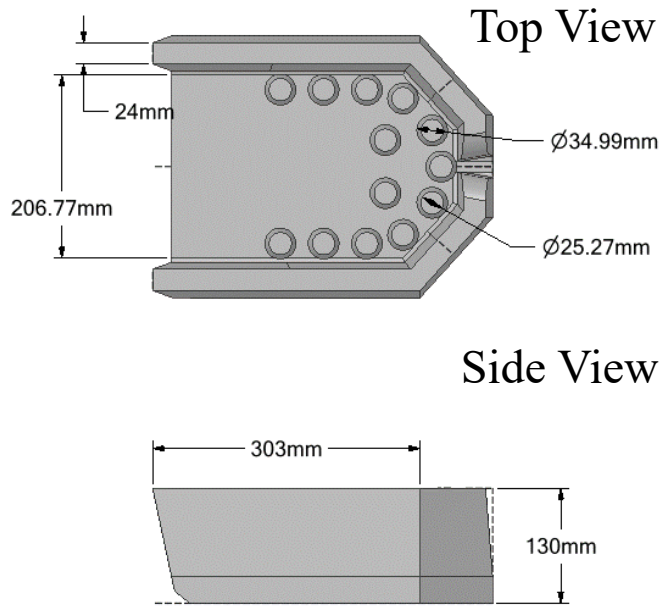


Figure 34. Turnflow geometry generated in SpaceClaim©. Side and Top view.

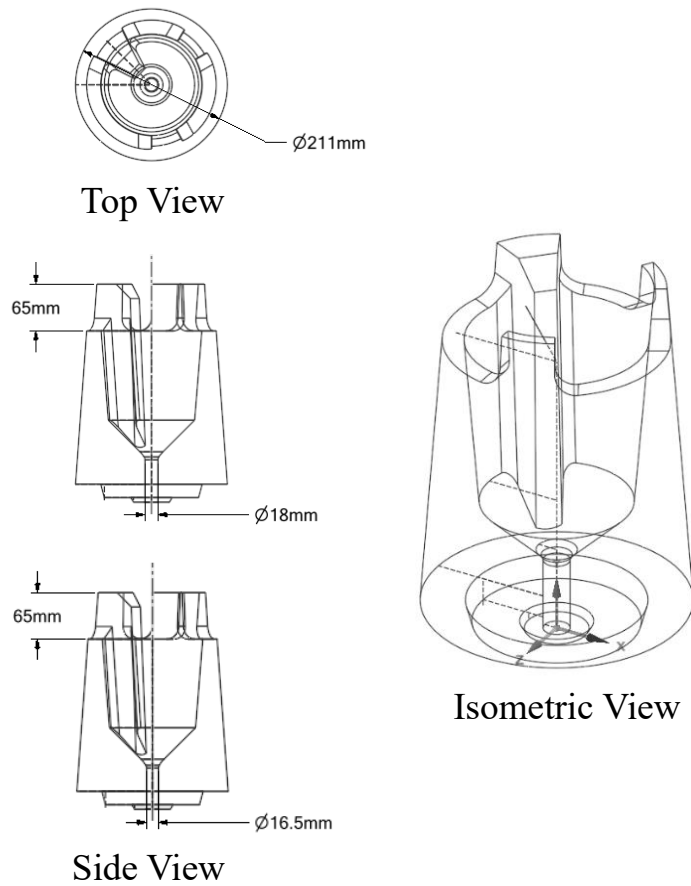


Figure 35. Anti-vortex nozzle geometry generated in SpaceClaim©.

After generating all the geometries for the process analysis separately and saved in different files, and assembly had to be done in SpaceClaim©, by specifying the location of the LS, Turnflow and anti-vortex nozzles within the Tundish. Figure 36 presents the exact position of the parts with respect to the Tundish. Afterwards, volume extractions were performed in the complete Tundish volume with the solid parts, the Turnflow, anti-vortex nozzles and LS walls to generate the final volume for subsequent meshing and mathematical modelling. The final volume is presented in Figure 37, where only half the system is observed since the system presents a symmetry plane, making it necessary to only solve half of the complete system.

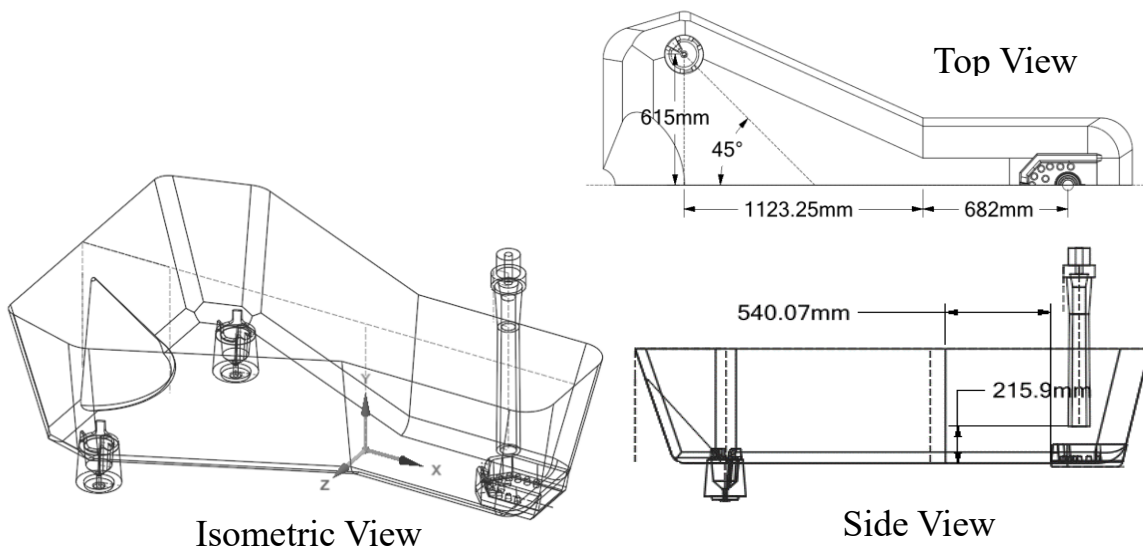


Figure 36. Position of the ladle shroud, turnflow and anti-vortex nozzles within the Tundish

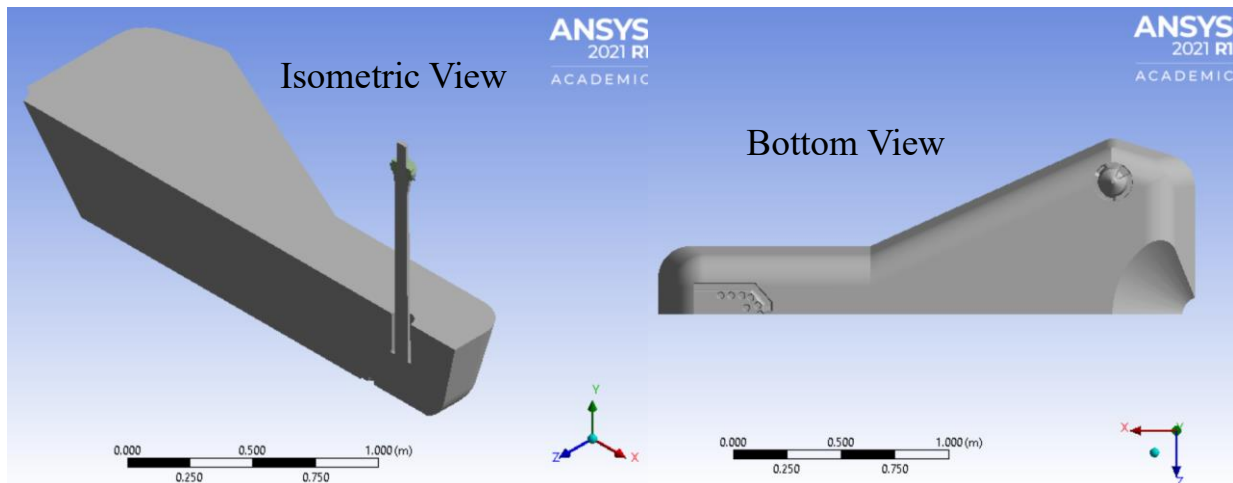


Figure 37. Final volume generated of the Ladle Shroud-Tundish system in SpaceClaim©.

As it was decided during the geometries development, that initially a detailed study of the Ladle Shroud was to be performed, 3 different reduced systems were generated and presented in Figure 38. Figure 38 (a) depicts the Ladle Shroud with argon injection and porous refractory and attached to a half cube volume as a simplification of the entry zone of the Tundish, this geometry is to be used to perform a baseline simulation and to observe the filling stage and argon injection phenomena in detail, a similar approach to that presented by Singh and Mazumdar [36], but this time including a third phase (air) and a transient start-up simulation. Figure 38 (b) shows the same system but without argon injection and porous refractory, the aim of this geometry is to calculate the expected pressure field, similarly to the work done in 1995 by Wang et al. [39], and try to simulate and quantify the air ingress through a 1.2 mm thick gap to exemplify an air ingress case. Figure 38 (c) shows a comprehensive geometry including the slide gate and the actual Tundish entry zone, including the Turnflow's walls. This geometry is to be applied for a comprehensive study and to obtain a close as possible approximation of the transient phenomena on the Ladle Shroud-Tundish system after analysis of the simplified cases. Details of the boundary conditions and mathematical modelling parameters will be presented in the subsequent sections.

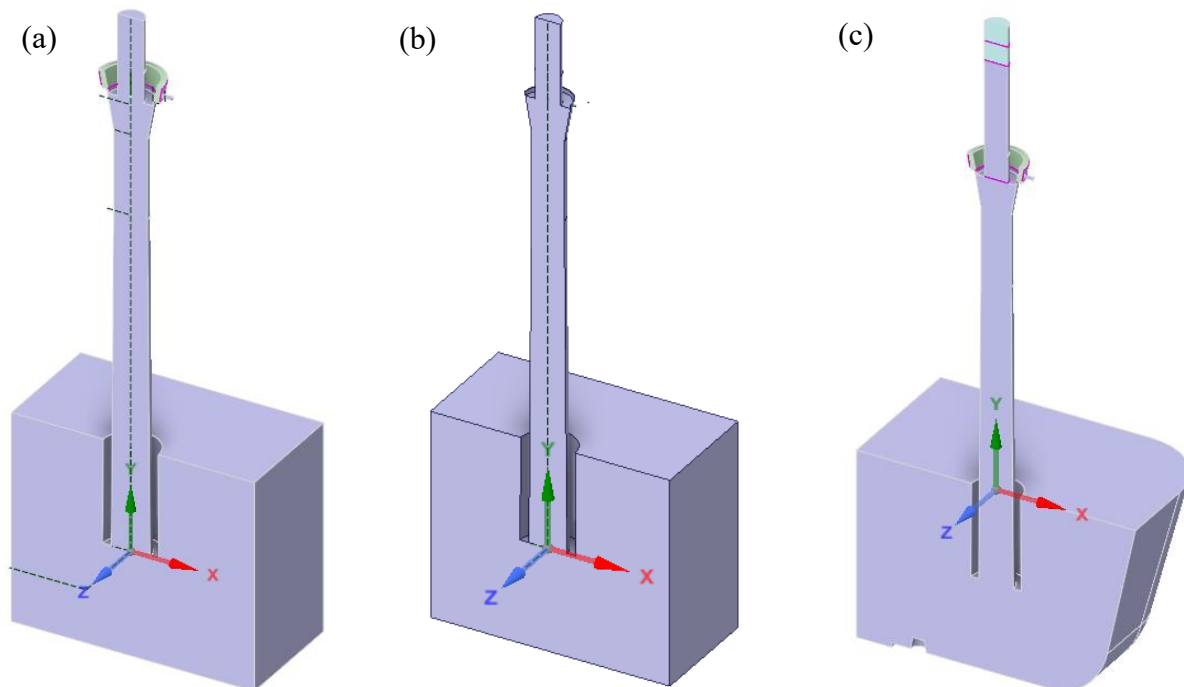


Figure 38. (a) Ladle Shroud geometry with simplified entry zone; (b) Ladle Shroud geometry without argon injection and 1.2 mm gap; (c) Ladle Shroud geometry with slide gate and actual Tundish entry zone with turnflow walls.

Additionally, a complete geometry of the Lade-Tundish system was generated with the Ladle geometry generated by co-worker Rohit Tiwari, to have a complete CAD representation of the process for a potential and future comprehensive study and as base for the physical models' construction at a later time. The commented geometry is presented in Figure 39.

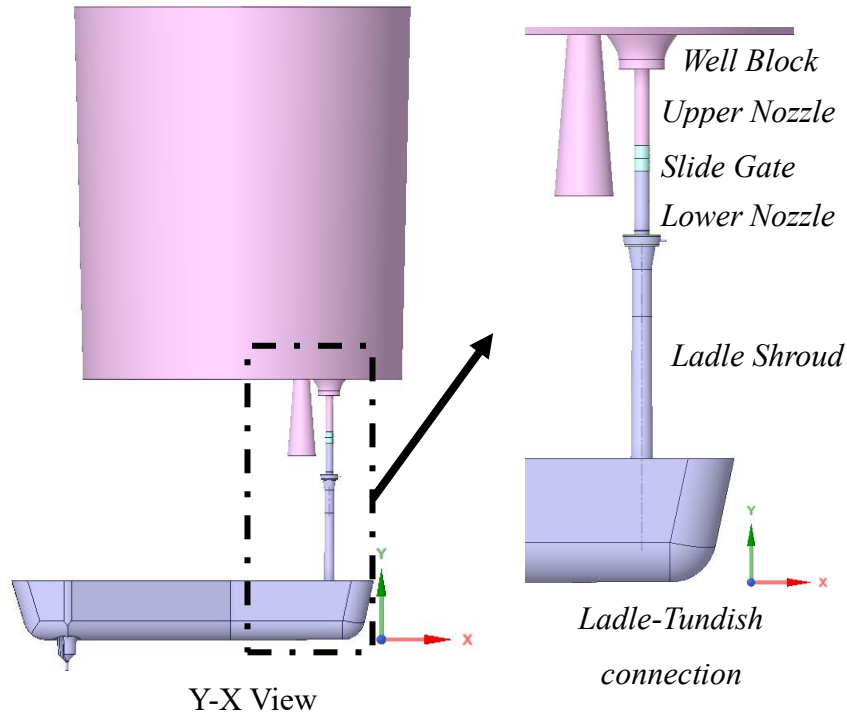


Figure 39. Ladle-Tundish system geometry generated in SpaceClaim© and details for the water model construction.

2.1.2 Meshing

After generating all the presented geometries, the files are exported to ANSYS Mesh©, part of the NAYS Workbench © software package, to perform the discretization/meshing. Due to the complexity of the geometries, a tetrahedral mesh method was used for all the cases. The number of elements ranged from around 150,000 to 650,000 for the different cases. An example mesh for the geometry of Figure 38 (c) is presented in Figure 39 with close ups of the argon injection zone and phases interfaces, where refinement was done for an accurate prediction of the interface tracking. In order to avoid numerical errors in ANSYS Fluent, the mesh quality for all the cases presented elements with a maximum skewness value of 0.75, skewness defined as: $\frac{[\text{optimal cell size}] - [\text{cell size}]}{[\text{optimal cell size}]}$, where a value of 0 represents a completely orthogonal element and 1 “the worst possible element” [38]. As common CFD practice, it is recommended to have a

maximum skewness between 0.80 to 0.94 [38], and histogram of the skewness metrics for the Figure 40 mesh is presented in Figure 41, where a maximum significant number of elements are observed with a skewness value of 0.63.

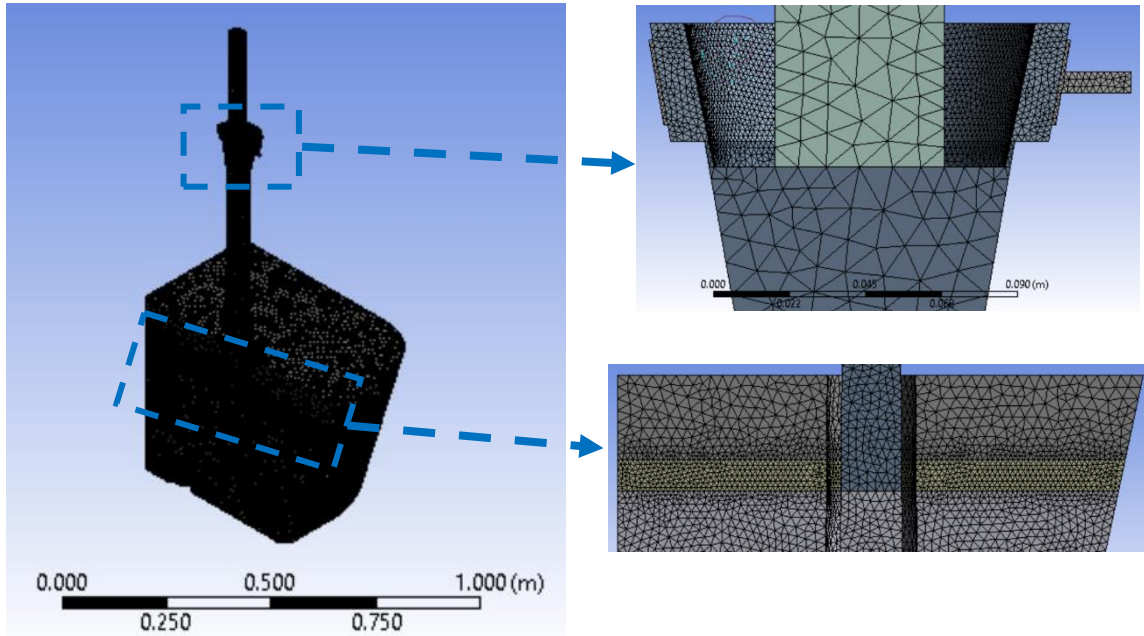


Figure 40. Mesh example with elements refinement examples generated in ANSYS Mesh ©.

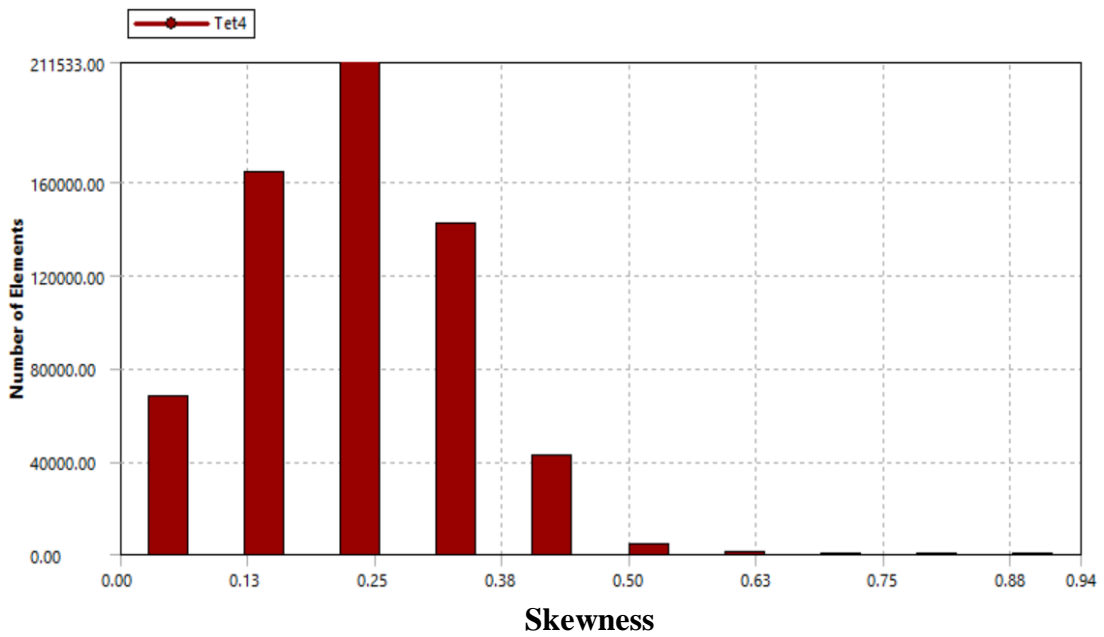


Figure 41. Skewness metric histogram for the Figure 40 mesh

The details of the mesh metrics (number of elements, average and maximum skewness) for each case will be presented separately in the following sections, as well as the Boundary conditions definition for each different, which is done in ANSYS Mesh©, but presented later individually for each case for clarity.

2.1.3 Governing Equations

The commercial CFD (Computational Fluid Dynamics) ANSYS Fluent 19.1 was used to solve the flow field based on the solution of the required governing equations via the Finite Volume Method (FVM) numerical method. The selection of the multi-phase model, interface interactions and turbulence model were done based on the literature review of the mathematical modelling of the Ladle Shroud system of the last 5 years. The equations applied which were solved are presented hereafter:

1. Volume of Fluid (VOF) multi-phase model continuity equation:

$$\frac{1}{\rho_q} \left[\frac{\partial}{\partial t} (\alpha_q \rho_q) + \nabla \cdot (\alpha_p \rho_p \vec{v}_q) \right] = \sum_{p=1}^n (\dot{m}_{pq} - \dot{m}_{qp}) \quad [1]$$

$$\sum_{q=1}^n \alpha_q = 1 \quad [2]$$

Where ρ , α , and \vec{u} correspond to the density, time, phase volume fraction and velocity, respectively for the q^{th} phase (steel, air, or argon), t corresponds to the time and \dot{m}_{pq} and \dot{m}_{qp} correspond to the mass flow from phase p to phase q and from phase q to phase p , respectively. Equation [2] indicates a constraint, where the sum of all the phase volume fractions is at all times equal to 1 and therefore the volume fraction of the phases is calculated via said constraint.

2. VOF Explicit formulation discretization equation:

$$\frac{\alpha_q^{n+1} \rho_q^{n+1} - \alpha_q^n \rho_q^n}{\Delta t} V + \sum_f (\rho_q U_f^n \alpha_{q,f}^n) = \left[\sum_{p=1}^n (\dot{m}_{pq} - \dot{m}_{qp}) \right] V \quad [3]$$

Equation [3] corresponds to the discretization of the volume fraction via the explicit formulation equation in a time dependent manner, where n , $\alpha_{q,f}^n$, V and U_f^n correspond to the index of a previous

time step, the face value of the q^{th} phase volume fraction, the volume of the cell and the normal volume flux through the face, respectively.

3. Momentum transport equation:

$$\rho \frac{\partial \vec{v}}{\partial t} + \rho(\vec{v} \cdot \nabla) \vec{v} = -\nabla p + \mu_{eff} \cdot \nabla^2 \vec{v} + \rho \vec{g} + F_\sigma \quad [4]$$

$$\rho = \sum \alpha_q \rho_q \quad [5]$$

$$\mu_{eff} = \mu_t + \sum \alpha_q \mu_q \quad [6]$$

$$F_\sigma = \sum_{i < j}^n 2\sigma_{ij} \frac{\alpha_i \rho_i \kappa_j \nabla \alpha_j + \alpha_j \rho_j \kappa_i \nabla \alpha_i}{\rho_i + \rho_j} \quad [7]$$

Equation [4] corresponds to a single momentum equation, which is solved and shared for all the phases. Equation [4] depends on the volume fractions of the phases via ρ and μ_{eff} which are calculated via equation [5] and [6] to obtain the volume fraction averaged density and effective viscosity, which includes μ_t , the turbulent viscosity calculated by the turbulence model. \vec{v} , p and \vec{g} correspond to the mixture velocity, pressure, and gravity, respectively.

F_σ corresponds to the surface tension force, where α_i , ρ_i and κ_i correspond to the volume fraction, density, and curvature, respectively. σ_{ij} corresponds to the surface tension between the phases. The surface tension force was only applied for one of the three cases, presented afterwards.

4. Standard k- ε Turbulence Model :

$$\mu_t = C_\mu \rho \frac{k^2}{\varepsilon} \quad [8]$$

$$\frac{\partial(\rho k)}{\partial t} + \nabla \cdot (\rho \vec{v} k) = \nabla \cdot \left[\left(\mu + \frac{\mu_t}{\sigma_k} \right) \nabla k \right] + G_k - \rho \varepsilon \quad [9]$$

$$\frac{\partial(\rho \varepsilon)}{\partial t} + \nabla \cdot (\rho \vec{v} \varepsilon) = \nabla \cdot \left[\left(\mu + \frac{\mu_t}{\sigma_\varepsilon} \right) \nabla \varepsilon \right] + C_1 \frac{\varepsilon}{k} G_k - C_2 \frac{\varepsilon^2}{k} \rho \quad [10]$$

Equation [8] corresponds to the definition of the turbulent viscosity, where C_μ is a model constant (0.09) and k corresponds to the turbulence kinetic energy and ε to the dissipation rate, and both terms are solved via equations [9] and [10] respectively. G_k corresponds to the generation of

turbulence kinetic energy due to shear work, and σ_k , σ_ε , C_1 and C_2 correspond to model constants, with values 1.0, 1.3, 1.43 and 1.92 respectively.

5. Porous media equations:

$$\frac{1}{\rho_q} \left[\frac{\partial}{\partial t} (\gamma \alpha_q \rho_q) + \nabla \cdot (\gamma \alpha_p \rho_p \vec{v}_q) = \gamma \sum_{p=1}^n (\dot{m}_{pq} - \dot{m}_{qp}) \right] \quad [11]$$

$$\gamma \rho \frac{\partial \vec{v}}{\partial t} + \gamma \rho (\vec{v} \cdot \nabla) \vec{v} = -\gamma \nabla p + \gamma \mu_{eff} \cdot \nabla^2 \vec{v} + \gamma \rho \vec{g} - \left(\frac{\gamma^2 \mu_{eff}}{K} \vec{v} + \frac{\gamma^3 \mu_{eff}}{2} \rho |\vec{v}| \vec{v} \right) \quad [12]$$

Where γ represents the media porosity. Equation [11] indicates the VOF continuity equation in the porous media and equation [12] represents the momentum transport equation in the porous media. The extra term on the right-hand side takes into account the viscous and drag forces imposed by the pore walls onto the fluid.

2.1.4 Operating conditions

All the relevant operating conditions were provided by the real industrial process to be applied as boundary conditions in the mathematical model. In the case of the inlet flows, (steel and argon shrouding), these were changed from volumetric flows to velocities. The most relevant operating conditions are presented below:

- Steel inlet velocity = **0.8 m/s**
- Argon inlet velocity= **0.526 m/s**
- Submerged depth of Ladle Shroud=7-8 inches (**203 mm**)
- Tundish liquid steel level= 16 inches (**406 mm**)
- Operating Pressure= **1 atm**
- Operating Temperature= **1873 K**

Additionally, the material properties are presented in Table 2.1.

Table 2.1. Materials properties

	Steel (liquid)	Water (liquid)	Air (gas)	Argon (gas)
Density, ρ [kg/m^3]	7000,[40]	1000, [41]	1.225, [41]	1.623, [41]
Dynamic viscosity, μ [Pa s]	0.0056, [40]	0.001001, [41]	1.78×10^{-5} , [41]	2.12×10^{-5} , [41]
Surface tension, σ [N/m]	-	0.073, [41]	1.7, [40]	1.6, [40]

2.1.5 ANSYS Fluent© Solution

After having generated the geometries, meshes and defining the governing equations, the mesh files are exported to ANSYS Fluent v19.0. In the *General* section, the solver is set up in general, a pressure-based type with an absolute velocity formulations solver is selected in transient state. The governing equations to solve, already presented, are enabled in the *Models* section, the materials properties are specified in the *Materials* section, where existing material can be imported from the ANSYS Fluent database or to create new material, like the case for the phase Steel. The *Boundary Conditions* are defined under the section with the same name, where the information of the boundary conditions is set. The *Cell Zone Conditions* can be used to define whether a volume is solid or fluid and define the material or to define the volume with a specified porosity, which will be the case for the argon shrouding porous refractory media. Details of the procedure for the ANSYS Fluent set up can be found in the ANSYS Fluent User Guide [38]. Figure 42 presents the ANSYS Fluent v19.0 tab with the described sections.

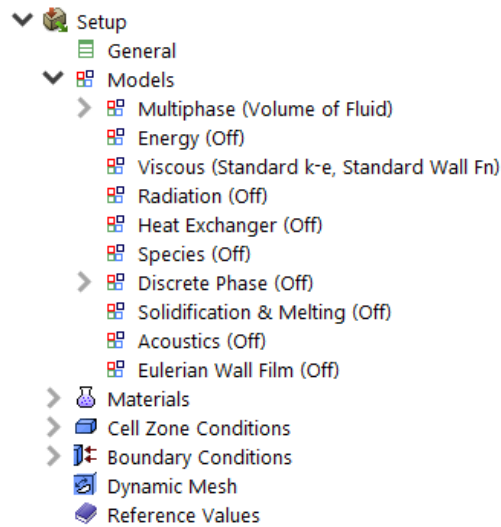


Figure 42. ANSYS Fluent v19.0 set up tab.

For the solution method, the Coupled scheme was selected, as it solves the pressure and momentum continuity equations together, which is essential for a gravity driven flow, like the a Ladle Shroud flow [42]. By using the usual SIMPLE and SIMPLEC solution method schemes, these were found to under-predict the absolute pressure field and the expected negative pressure at the top portion of the Ladle Shroud, to be commented later.

After having set up all the required information, the solution is initialized, with a standard initialization, where the initial variables values are set to 0, except for the initial phase volume fraction. For the transient calculation, convergence was defined when all the variables' residuals reached 1×10^{-4} and a maximum of 20 iterations were set per time step. As well, a variable time step size was set between 1×10^{-5} to 0.1 seconds, maintaining a Courant number of maximum 2.0. Then, the calculations are started, and animations are pre-defined to track the simulation progress in real time. The date files are saved automatically each 2000 iterations for every simulation for posterior visualization and analysis. The simulations were performed in the MMPC High Performance Computer (HPC) consisting of 6 independent nodes for parallel simulations, each with 16 GB of RAM.

2.1.6 Cases descriptions

For the study of the Ladle Shroud (LS), three different cases were developed and solved, which geometries are presented in Figure 38. First, a called “Simplified case” was developed to study the

argon shrouding distribution in a simplified vessel, similar to the study performed by Singh and Mazumdar [36], but now taking into account a third phase. Additionally, transient phenomena during the filling stage were studied to analyze the LS design and performance during a start-up operation for a first time in the research of said systems. The “Simplified case” was also developed as a reference and starting simulation to develop subsequent more comprehensive cases. Secondly, a called “Air suction case”, was done to try to simulate and quantify air ingress due to an expected negative pressure in the lower nozzle and LS joint. Thirdly, a named “Real case”, was developed to study the filling stage and steady state operation of the LS with the actual Tundish entry zone, including the Turnflow. Also, for the third case, the surface tensions forces were considered, as well as the argon shrouding flow effect on the slag layer during ladle change-over to perform a comprehensive study on the sources of inclusions and inclusions control in the LS-Tundish entry zone subsystem. Figure 43 depicts the summary of the developed cases for the study of the LS subsystem.

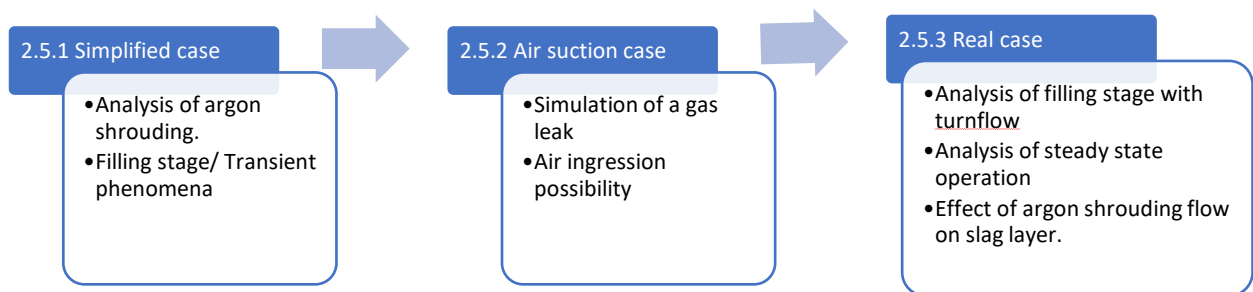


Figure 43. Summary of the case descriptions

In the following sections, each case details are presented with its boundary conditions, mesh information and governing equations details and the corresponding results are presented separately for each case.

2.1.7 Simplified Case

A simplified case was firstly developed, to try to simulate the filling stage of the LS and the argon shroud flow with a simplified vessel geometry, to optimize computational time and effort by generating a subsystem of the LS-Tundish system. Figure 44 presents the geometry and boundary conditions for the simplified case, where only half of the domain was generated, due to a symmetry

plane, making it necessary to only solve half of the system. The following are some details and model suppositions of the implemented mathematical model for the present case:

- 1 atm operating pressure and 9.81 m/s^2 gravity acceleration on the -y direction.
- Isothermal system.
- VOF Multi-phase model with sharp interface treatment consisting of 3 phases: steel (fluid), air (gas), and argon (gas).
- Transient state with adaptive time step (initial time step: 1×10^{-5} seconds), maintaining a global Courant number of 2.0.
- The porous refractory was simulated as porous media with a 0.5 porosity (γ), using Darcy's law and the superficial velocity calculation, where the continuity and momentum transport equations terms are multiplied by the porosity, to be presented in detail later, only in the defined media as porous and assumed with isotropic porosity. Details of the used Darcy's law in porous media model can be consulted in the ANSYS Fluent Theory Guide [42]
- Initially, at time=0, the system was assumed to be filled with air, meaning all the system has an air volume fraction of 1.
- Height of the vessel of 16 inches (406.4 mm)

The following boundary conditions were defined for the Simplified Case:

1. Steel Velocity Inlet: defined as a velocity inlet with a specified constant velocity of 0.800 m/s perpendicular to the surface and a gauge pressure of 1 atm to consider the above steel head pressure, and steel volume fraction of 1. The inlet turbulence kinetic energy in and turbulent dissipation rate are specified via $k_{in}=0.01v_{in}^2$ and $\epsilon_{in}=2k^{1.5}/d_{in}$, respectively [37].
2. Gas Velocity Inlet: defined as velocity inlet with a constant velocity of 0.526 m/s perpendicular to the surface and an argon volume fraction of 1. The inlet turbulence parameters k_{in} and ϵ_i are calculated similarly to the steel velocity inlet parameters.
3. Symmetry plane: defined as a symmetry boundary conditions, meaning no momentum transfer is allowed through the plane.
4. Pressure outlet: pressure outlet boundary condition to simulate a top free open surface with a gauge pressure of 0 atm and a specified backflow volume fraction of air equal to 1.
5. Walls: all the other surfaces are set as a wall boundary conditions, where a no-slip conditions is applied with a standard wall treatment function.

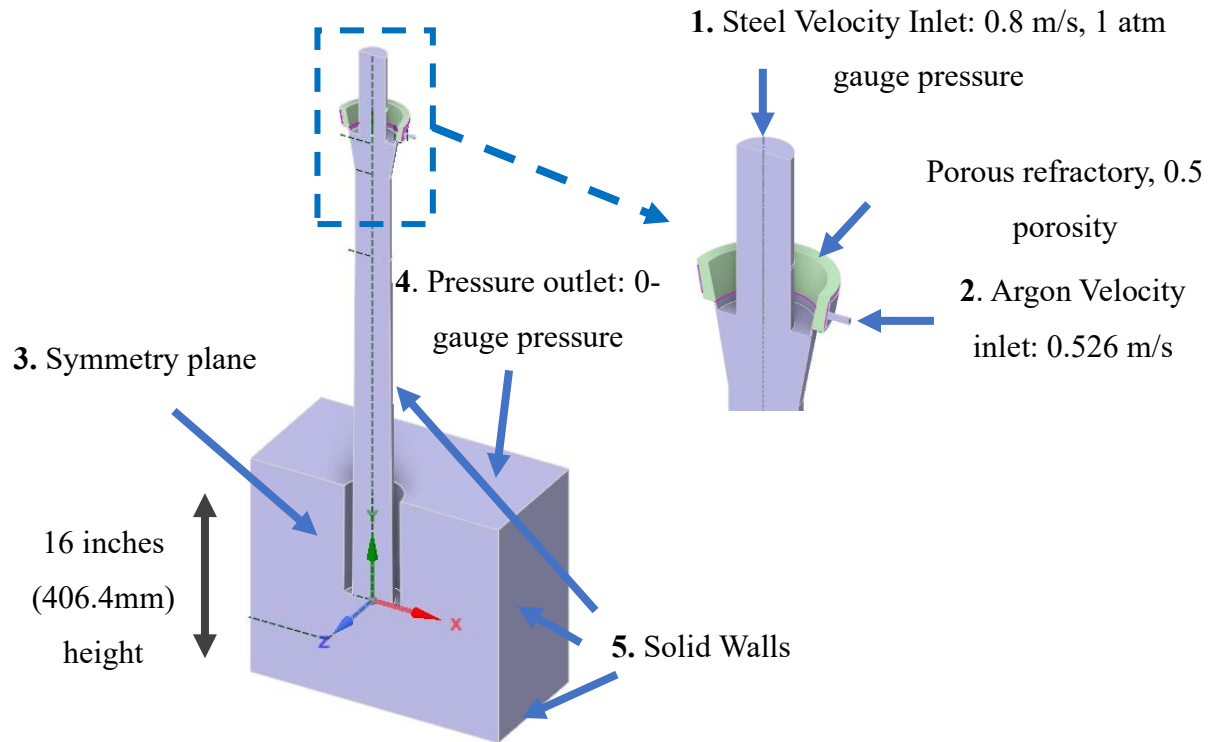


Figure 44. Geometry and Boundary Conditions for the Simplified case.

Figure 45 shows the generated mesh for the simplified case, consisting of a total of 500,000 elements with an average size of $9 \times 10^{-9} \text{ m}^3$ and an average skewness of 0.22 and a maximum skewness value of 0.82 presented by less than 20 elements. Mesh refinement was done in the argon shrouding media and the porous refractory for better accuracy of the argon distribution, as mentioned on Section 2.2.

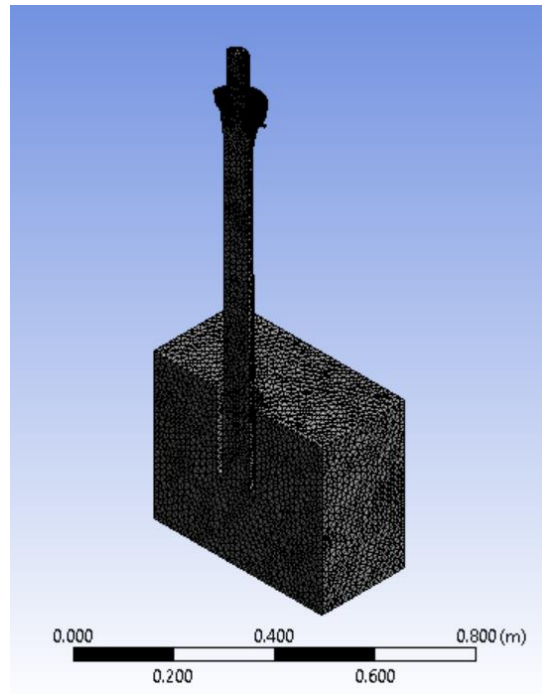


Figure 45. Mesh used for the Simplified Case.

2.1.8 Air Suction Case

After performing the simplified case simulation as an initial approximation of the filling stage and quasi-steady state ladle shroud operation and obtaining a negative pressure of around 0.60 atm at the lower nozzle-ladle shroud joint, and air suction case was then developed to try to simulate and quantify the expected air suction. Figure 46 presents the geometry and boundary conditions for the air suction case, where only half of the domain was considered, similarly to the simplified case. The following are some details and assumptions of the implemented mathematical model for the present case:

- 1 atm operating pressure and 9.81 m/s^2 gravity acceleration in the -y direction.
- Isothermal system.
- VOF Multi-phase model with 2 phases: steel (fluid) and air (gas).
- Transient state with adaptive time step (initial time step: 1×10^{-5} seconds), maintaining a global Courant number of 2.0.
- No argon shrouding injection.
- 1.2 mm thick wall/gap between the lower nozzle and ladle shroud joint.

- Initially, at time=0, the system was assumed to be filled with air, meaning all the system has an air volume fraction of 1.
- Height of the vessel of 16 inches (406.4 mm)

The following boundary conditions were defined for the Air Suction Case:

1. Steel Velocity Inlet: defined as a velocity inlet with a specified constant velocity of 0.800 m/s perpendicular to the surface and a gauge pressure of 1 atm to consider the above steel head pressure, and steel volume fraction of 1. The inlet turbulence kinetic energy in and turbulent dissipation rate are specified via $k_{in}=0.01v_{in}^2$ and $\epsilon_{in}=2k^{1.5}/d_{in}$, respectively [37].
2. Wall-Pressure outlet: defined initially as a wall boundary condition and the changed after 41.853 seconds, time when the Ladle Shroud is filled with the steel phase, to pressure outlet boundary condition with velocity equal to 0 m/s and 0 atm gauge pressure, where only the air phase is allowed to enter the system. With this change of boundary condition a air inflow or outflow is simulated based on the pressure difference between the Ladle Shroud inside and the exterior media at 1 atm absolute pressure.
3. Symmetry plane: defined as a symmetry boundary conditions, meaning no momentum transfer is allowed through the plane.
4. Pressure outlet: pressure outlet boundary condition to simulate a top free open surface with a gauge pressure of 0 atm and a specified backflow volume fraction of air equal to 1.
5. Walls: all the other surfaces are set as a wall boundary condition, where a no-slip conditions is applied with a standard wall treatment.

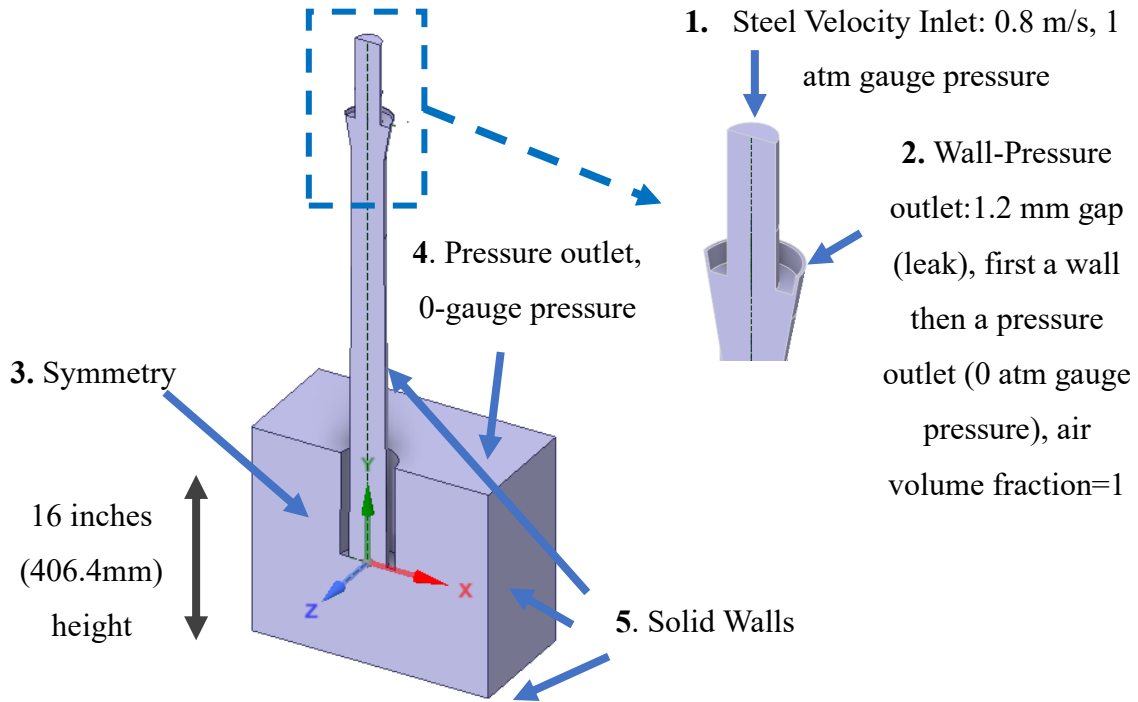


Figure 46. Geometry and Boundary Conditions for the Air Suction Case.

The mesh generated is the same as in the simplified case, however the argon shrouding media and the porous refractory are eliminated. Figure 47 shows the generated mesh for the air suction case, consisting of a total of 480,000 elements with an average size of $9 \times 10^{-9} \text{ m}^3$ and an average skewness of 0.22 and a maximum skewness value of 0.82 presented by less than 20 elements. Mesh refinement was done in gap zone and the porous refractory for better accuracy of air inflow.

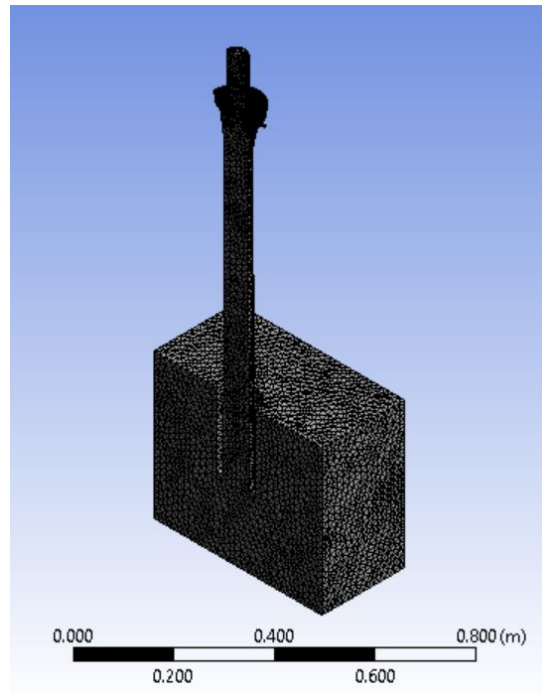


Figure 47. Mesh used for the Air suction case.

2.1.9 Real Case

A third case was developed, where the actual geometry of the Tundish entry zone is considered, including the Turnflow walls and the slide gate-lower nozzle parts. For this case, also a more refined mesh is generated, and the surface tension forces are taken into account for better model accuracy (F_σ term in equation [4] of section 2.3). As well, a stricter time step size criterion was applied for better capture of the time dependent interface due to the expected high turbulence and flow breakage due to the collision of the steel flow with the Turnflow's walls. Figure 48 presents the geometry and boundary conditions for the present real case. The following are some details of the implemented mathematical model for the present case:

- 1 atm operating pressure and 9.81 m/s^2 in the -y direction
- VOF Multi-phase model with 3 phases: steel (fluid), air (gas), and argon (gas).
- Transient state with adaptative time step (initial time step: 1×10^{-7} seconds), maintaining a global Courant number of 2.0.
- The porous refractory was simulated as porous media with a 0.5 porosity (γ), using Darcy's law and the superficial velocity calculation, where the continuity and momentum transport

equations terms are multiplied by the porosity, to be presented in detail later, only in the defined media as porous and assumed with isotropic porosity. Details of the used Darcy's law in porous media model can be consulted in the ANSYS Fluent Theory Guide [42].

- Initially, at time=0, the system was assumed to be filled with air, meaning all the system has an air volume fraction of 1.
- Height of the vessel of 16 inches (406.4 mm)
- System including Tundish entry zone real geometry with Turnflow walls and lower nozzle and slide gate volume.
- The domain considers ± 303 mm along the *x-axis* to only take into account the entering zone of the complete Ladle Shroud-Tundish system.

The following boundary conditions were defined for the Simplified case:

1. Steel Velocity Inlet: defined as a velocity inlet with a specified constant velocity of 0.800 m/s perpendicular to the surface and a gauge pressure of 1 atm to consider the above steel head pressure, and steel volume fraction of 1. The inlet turbulence kinetic energy in and turbulent dissipation rate are specified via $k_{in}=0.01v_{in}^2$ and $\epsilon_{in}=2k^{1.5}/d_{in}$, respectively [37].
2. Gas Velocity Inlet: defined as velocity inlet with a constant velocity of 0.526 m/s perpendicular to the surface and an argon volume fraction of 1. The inlet turbulence parameters k_{in} and ϵ_i are calculated similarly to the steel velocity inlet parameters.
3. Symmetry plane: defined as a symmetry boundary conditions, meaning no momentum transfer is allowed through the plane.
4. Pressure outlet: pressure outlet boundary condition to simulate a top free open surface with a gauge pressure of 0 atm and a specified backflow volume fraction of air equal to 1.
5. Walls: all the other surfaces are set as a wall boundary conditions, where a no-slip condition is applied with a standard wall treatment.

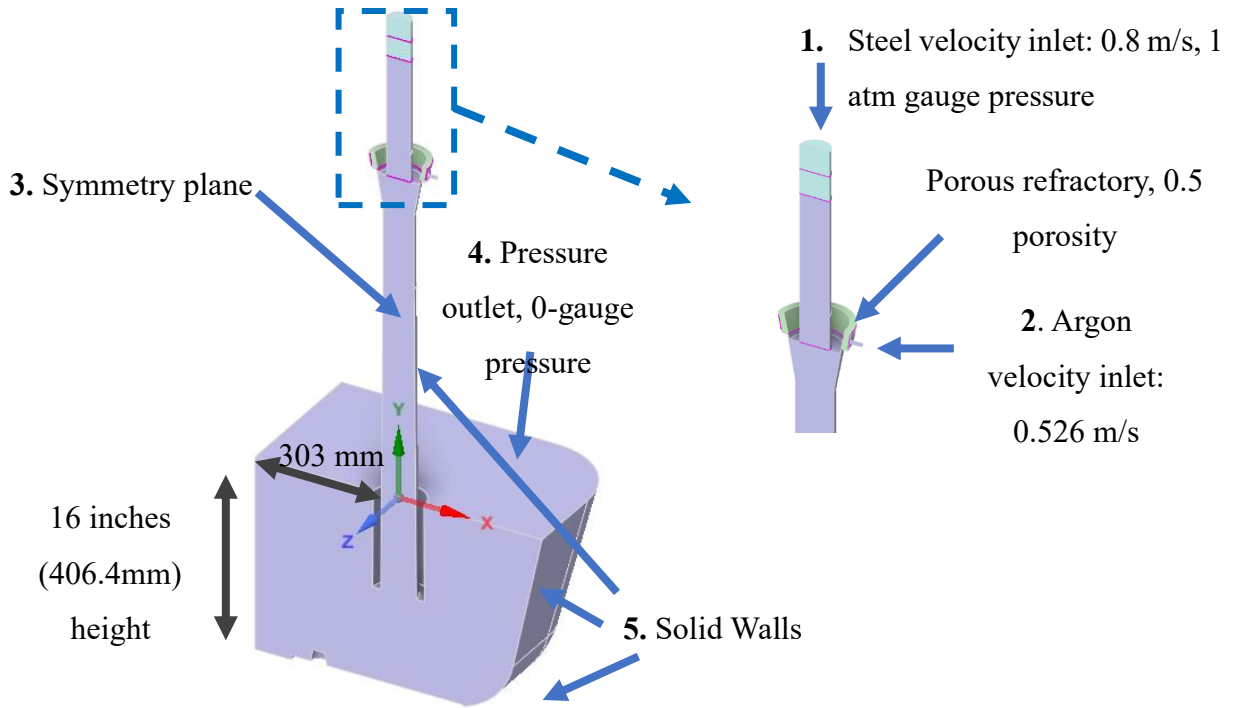


Figure 48. Geometry and Boundary Conditions for the Real Case.

Figure 49 shows the generated mesh for the real case, consisting of a total of 700,000 elements with an average size of $8.5 \times 10^{-9} \text{ m}^3$ and an average skewness of 0.22 and a maximum skewness value of 0.90 presented by less than 30 elements located in the bottom Turnflow's walls, after simulation tests, these elements did not generate errors in the simulation and solution reached convergence like the previous cases. Mesh refinement to $1.5 \times 10^{-9} \text{ m}^3$ was done in the argon shrouding media and the porous refractory for better accuracy of the argon distribution.

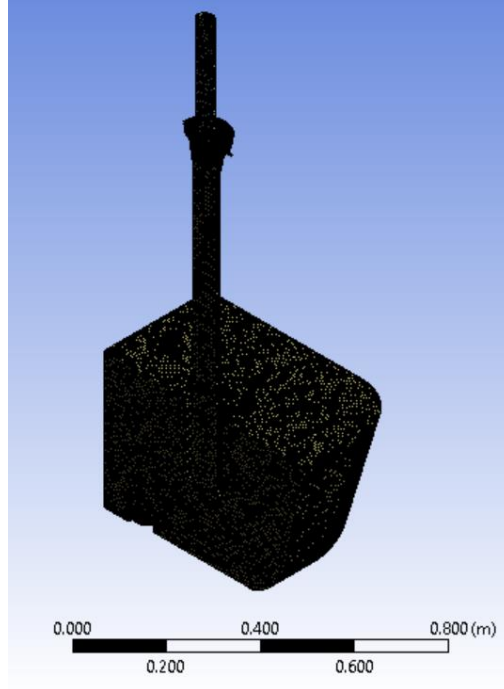


Figure 49 Mesh used for the Real case.

2.2 Physical Modelling

Physical modelling study of Ladle Shroud-Tundish multi-phase systems can be done with full-scale water models [34, 35], given that both Fr and Re dynamic similarities are conserved:

$$Fr_{model} \approx Fr_{full\ scale} \quad [13]$$

$$\frac{u_{model}}{\sqrt{gL}} = \frac{u_{full\ scale}}{\sqrt{gL}} \quad [14]$$

$$Re_{model} \approx Re_{full\ scale} \quad [15]$$

$$\frac{u_{model}L}{\nu_{water}} = \frac{u_{full\ scale}L}{\nu_{steel}} \quad [16]$$

Here, L corresponds to the characteristic length of the model, and in a full-case model, this length is the same in both the real model and the full-scale system. The velocity u is also preserved in the water model and since $\nu_{water} \approx \nu_{steel}$; $1 \times 10^{-6} \approx 0.916 \times 10^{-6} m^2/s$, both the Fr and Re dimensionless numbers can be practically exactly equalized, allowing for the exact replication of the fluid phenomena within the Ladle Shroud-Tundish system with the experimental practicality and visibility inherent to water models, that is widely used in the physical modelling of

Steelmaking Systems. For example, good correlations between experimental and mathematical results with full-scale water models in multi-phase analyses have all been obtained recently [30, 33, 34, 36].

For the construction of the full-scale model, diagrams and real parts provided by the industrial partner were used to replicate exactly the dimensions and intricacies (mainly the lower nozzle-Ladle Shroud connection) in the Ladle Shroud-Tundish system. It is important to mention that to focus on the Ladle Shroud design transient performance analysis, the complete Tundish water model has not been constructed, only part of the whole system was built, similar to the subsystem developed in the CAD geometry for the mathematical modelling. The steps of the adaptation process of the real industrial model for the water model construction will be discussed in the following sections and then the results visualization is presented for comparison with the mathematical modelling results.

2.2.1 Real dimensions and details

Figure 50 presents a CAD visualization of the complete Ladle-Tundish system inner volume and a corresponding close-up of the detail of the part of study in the present work, the connection between the ladle and the Tundish, consisting of the well block, upper nozzle, slide gate, lower nozzle, and Ladle Shroud. The CAD geometry was generated to have all the internal and necessary dimensions for the volume used for the mathematical modelling, as well as to be replicated in the water model of the system obtained from the provided diagrams and parts of the real industrial system. Figure 51 depicts the dimensions (diameters and heights) of the different parts to be built for the water model in transparent plastic (PVC or Plexiglas). The dimensions were respected as much as possible, with some minor adjustments being necessary during the construction and assembly of the parts. Figure 52 shows a real lower nozzle and Ladle Shroud made of MnO-Graphite refractory with details of the overlapping connection and the argon injection location and detail. It can be observed in the same Figure, that the connection is just an overlap between a male-female connection and a soft gasket, shown in Figure 53, and no extra seal or protection is used. As such, there is an absolute need for the injection of argon to be able to expel any ingress of air, as previously commented upon.

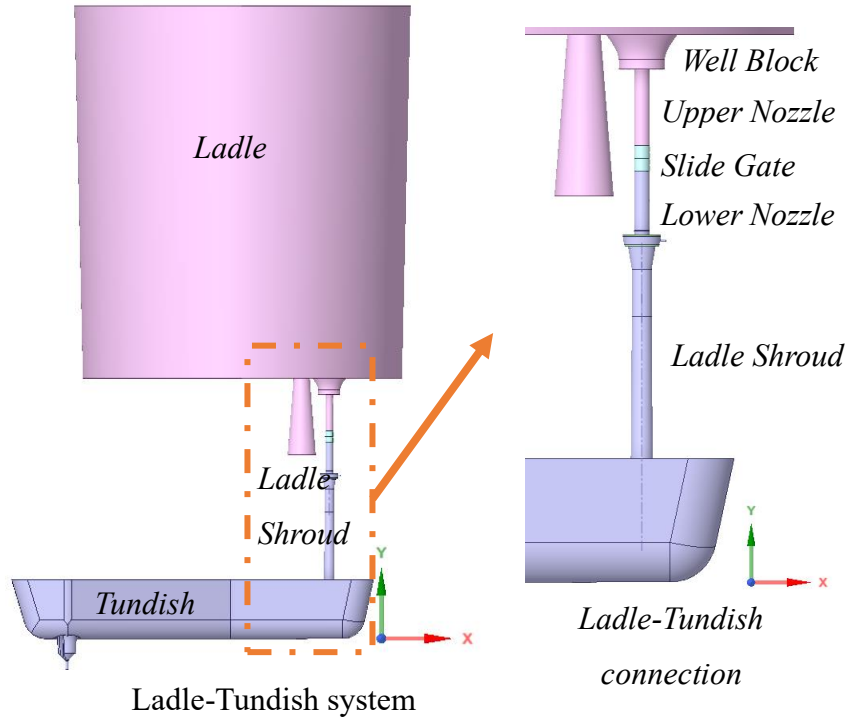


Figure 50. Diagram of the Ladle-Tundish system and close-up of the Ladle-Tundish connection

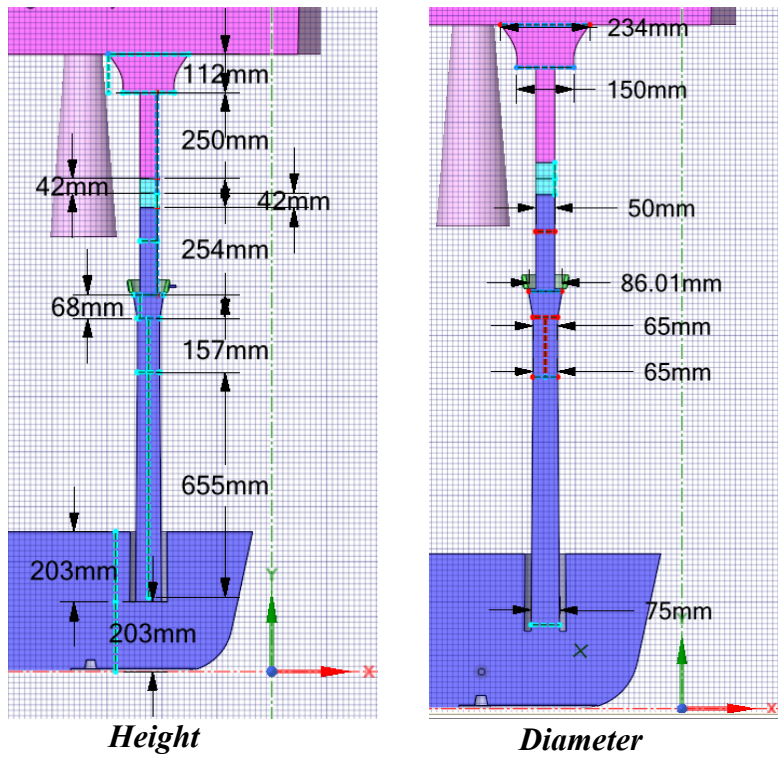


Figure 51. Dimensions of the Ladle-Tundish connection

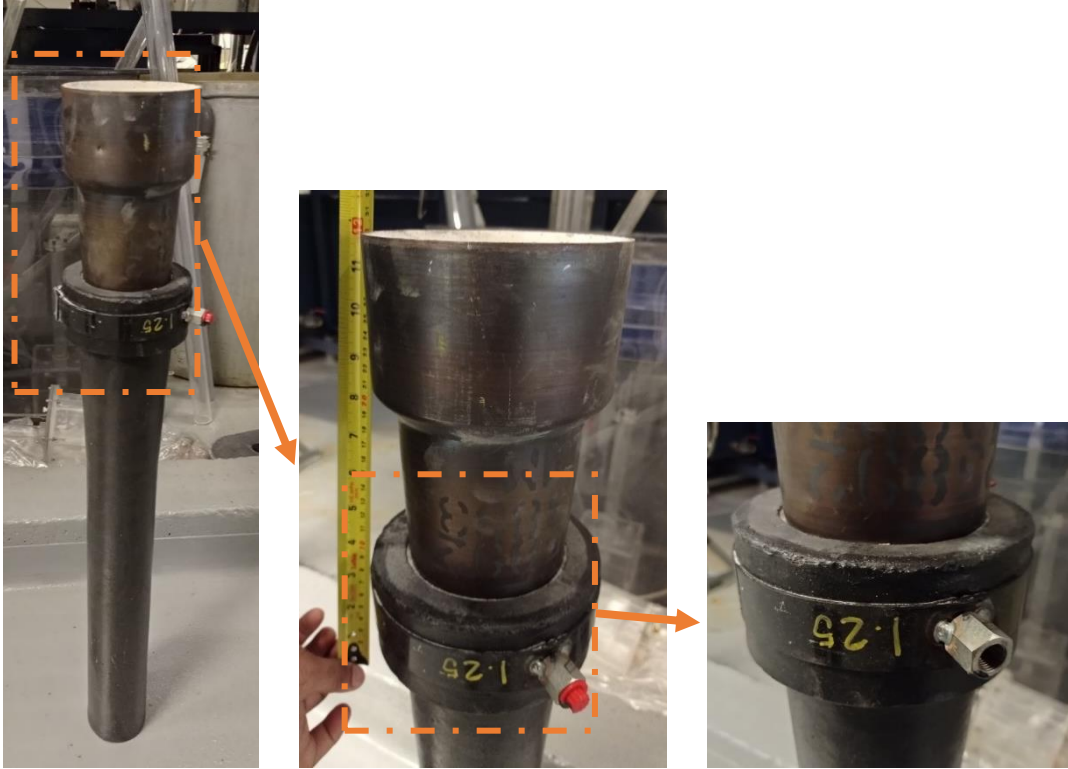


Figure 52. Real lower nozzle and Ladle Shroud and detail of overlapping connection and argon injection.



Figure 53. Gasket between the Ladle Shroud and lower nozzle

2.2.2 Construction of the full-scale Ladle Shroud system for water modelling research

For the construction of the water model, only the parts below the slide gate, meaning the lower nozzle and Ladle Shroud, were built, as a previous full-scale ladle slide-gate water model set-up was already in place within the MMPC's water modeling laboratory, with very similar dimensions. A height adjustment to the lower nozzle, from 254 to 215 mm was performed, to compensate for the height of the parts already in place and respect the total height of 1580 mm between the bottom of the ladle and the bottom of the Ladle Shroud, in the corresponding industrial set-up. That adjustment allowed one to maintain the full-scale Re and Fr numbers in dynamic similarity, as per Figure 51.

Similarly, the total height of the Ladle Shroud was set equal to that of the industrial set-up: i.e., 880 mm. Similarly, to construct this transparent (Ladle Shroud), and respect the changes in different inner diameters in the real system, this was divided into three segments (A), (B) and (C), presented in Figure 54. These parts were constructed, separately. The lower nozzle was replicated with a 155 mm height and 50.8 mm (2 inches) ID transparent PVC pipe, glued to a truncated hollow cone with a 50.8 mm ID and variable thickness, according to Figure 55. This said part was specially manufactured to exactly replicate the already commented overlapping connection between the lower nozzle and Ladle Shroud. The Ladle Shroud (A) was manufactured similarly to the bottom part of the lower nozzle, but with a variable ID from 104.54 to 62 mm for the lower nozzle to have a 60 mm penetration into the Ladle Shroud like that shown in Figure 52. Figure 55 depicts sketch with the dimensions used for the construction of the bottom part of the lower nozzle and the Ladle Shroud (A). The Ladle Shroud (B) had to be adapted from a 65 mm ID to a 63.5 mm ID (2.5 inches) transparent PVC pipe, due to the unavailability of a standard pipe size of 65 and the availability of a 63.5 mm (2.5 inches) pipe.

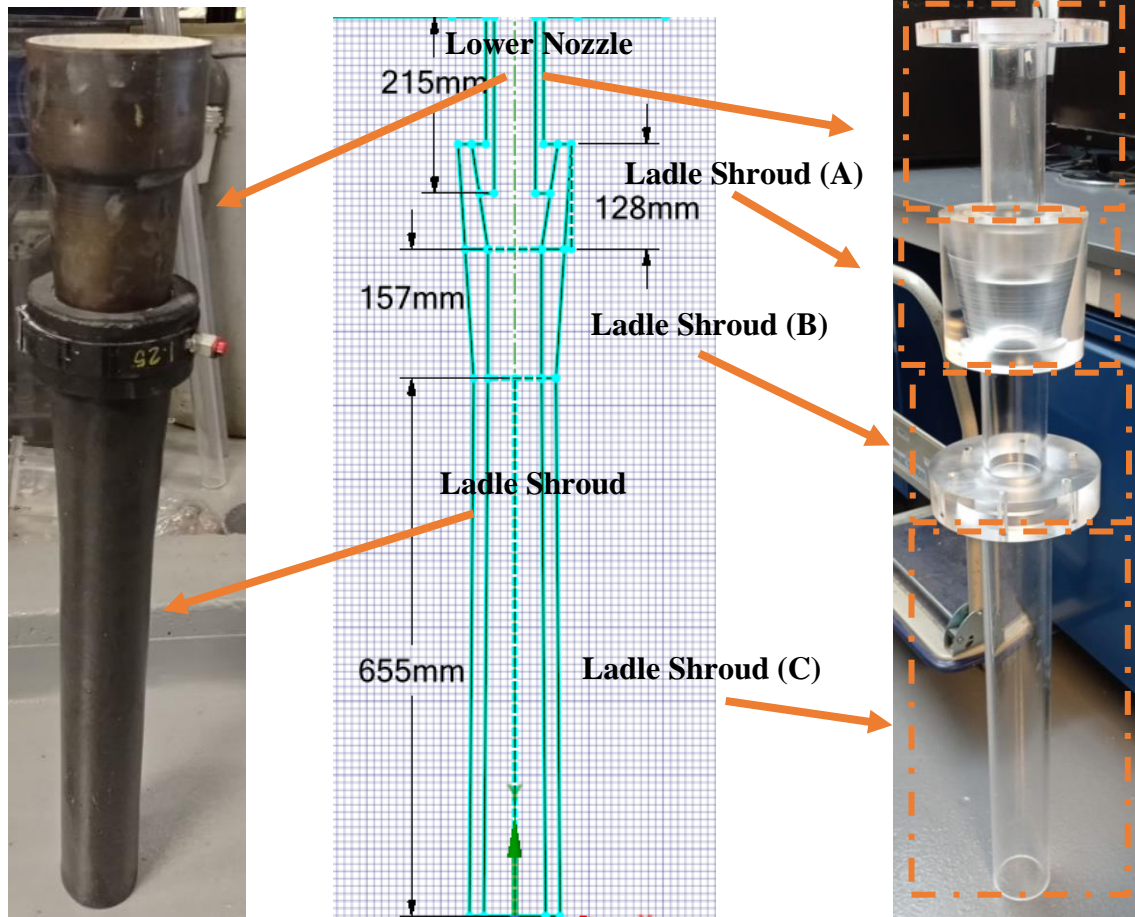


Figure 54. Actual Ladle Shroud, schematic, and final water model.

The Ladle Shroud (C) part, according to the corresponding industrial set-up, presents a diverging ID from 65 to 75 mm in a 655 mm height. Due to the complexities and unavailability of a transparent plastic to be manufactured with said dimensions, it was decided to use instead a 70 mm ID (2 $\frac{3}{4}$ inches) with a 655 mm height transparent PVC pipe, being 70 mm the average diameter of the real diverging Ladle Shroud. This adaptation is considered to not affect considerably the sought similarity between the industrial process and the water model. The three parts of the Ladle Shroud were glued together, and a connecting flange was used between the part (B) and (C), and to be attached to the slide gate, subsequently. The resulted assembled plastic model of the Ladle Shroud is seen in Figure 54 whilst, Figure 56 shows the dimensions of the used transparent PVC pipes for the water model construction.

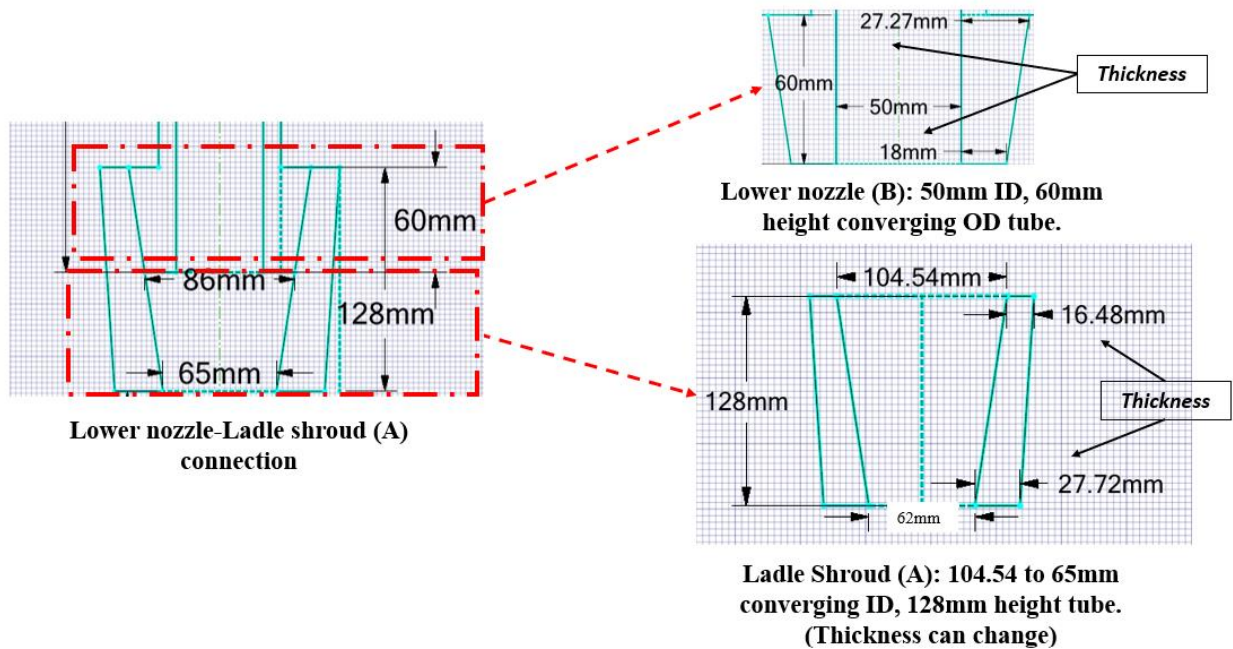


Figure 55. Lower nozzle and Ladle Shroud (A) schematic for model construction.

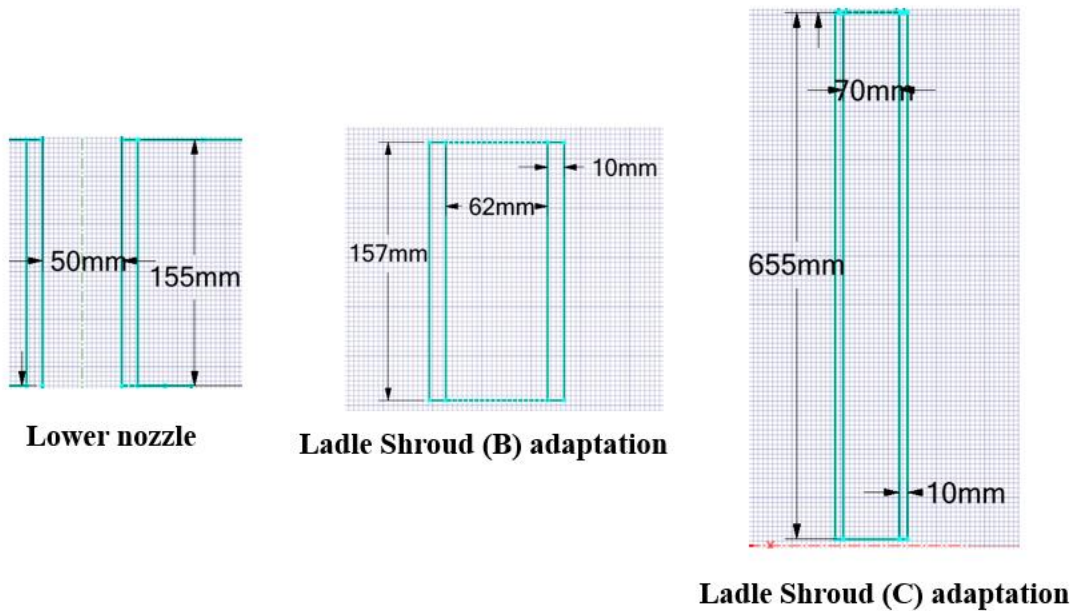


Figure 56. Parts adaptation for model construction

For the construction of the Tundish model for the water modelling research, it was decided to adapt and construct the first portion of the Tundish, meaning the first 1041 mm, as per Figure 57. This is due the fact that for the present work, only the flow phenomena in the Ladle Shroud and Tundish entry zone were to be studied. Similarly, the rounded edges were also not replicated, due to the

complexity of the manufacturing requirements. Figure 57 presents the adaption of the industrial set-up Tundish, to a truncated water modelling tundish. The physical model reproduces the first 1041 mm of the volume of the tundish, without the rounded edges, and using 12.7 mm (1/2 inch) thick Plexiglas sheets. Figure 58 depicts the details and dimensions for the construction of the Tundish-tank Plexiglas model from different views. It can be observed in the left view, that the tank presents the same height as the industrial Tundish of 670 mm. An inner dam (which can be removed) was located at 80 mm from the left-hand side wall to maintain a quiescent quasi-steady state flow at 406.4 mm (16 inches), being the operational steel level height. The inner dam acts to always maintain the maximum level of steel in the tundish. The overflow of water pours over the dam, and this output of water flows down to drain through a 76.2 mm (3 inches) hole, set at the bottom of the exit port. The Plexiglas 17" inch sheets were cut and assembled per Figure 58.

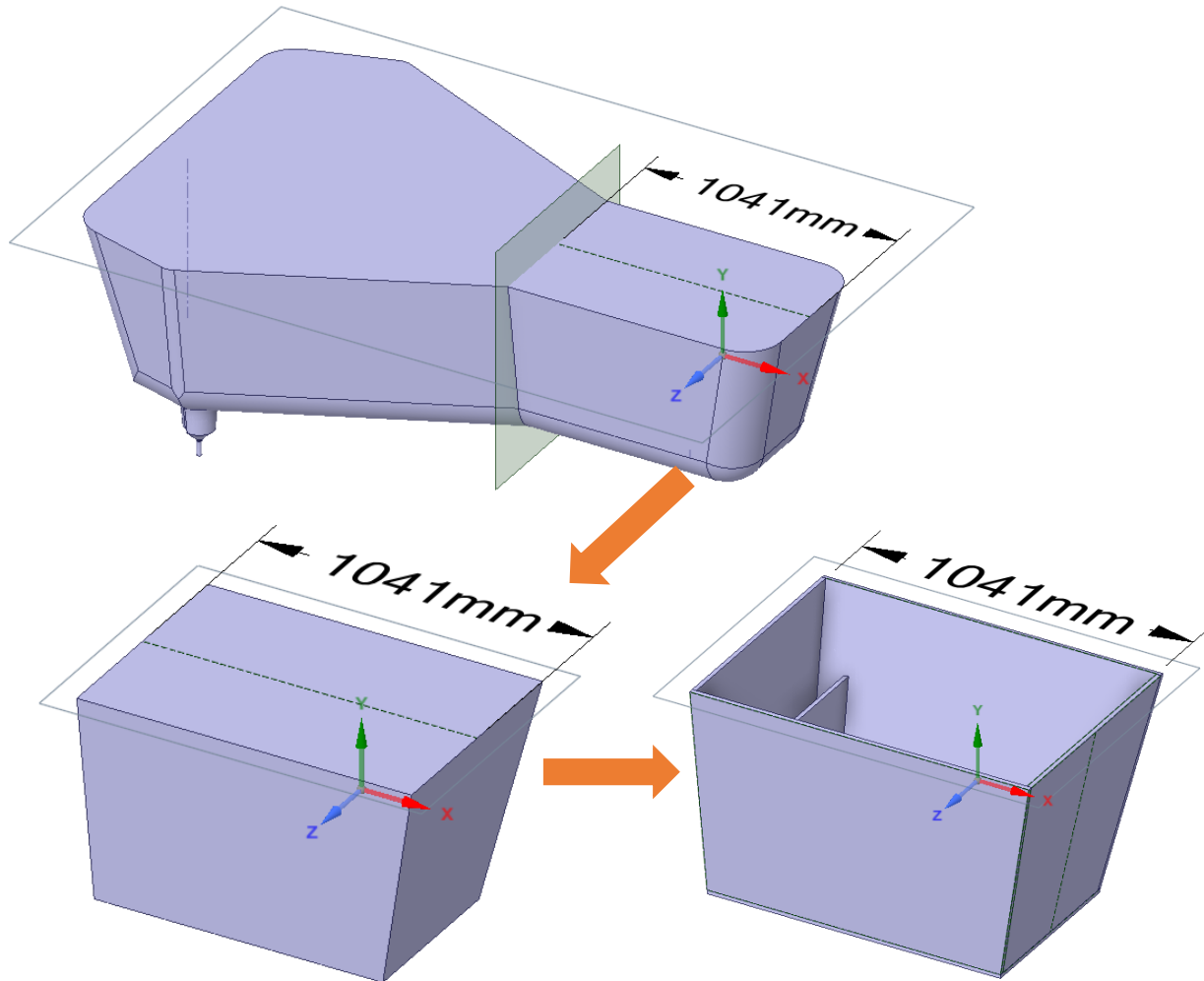
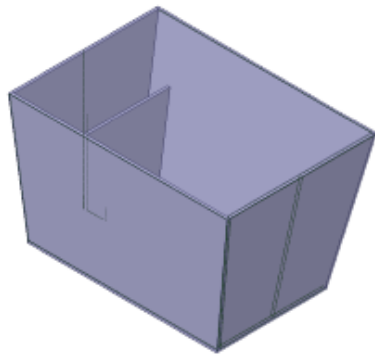
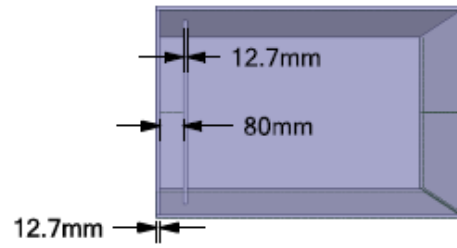


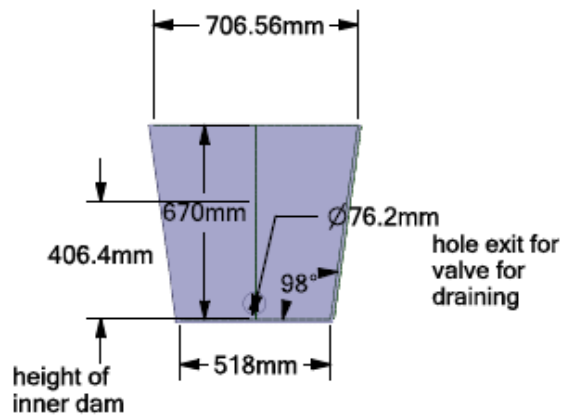
Figure 57. Development and adaptation of Tundish-tank for water model.



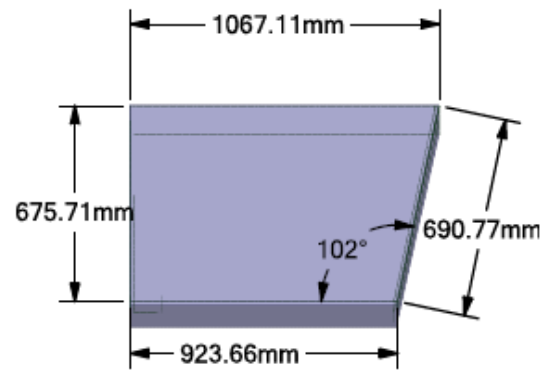
Isometric view



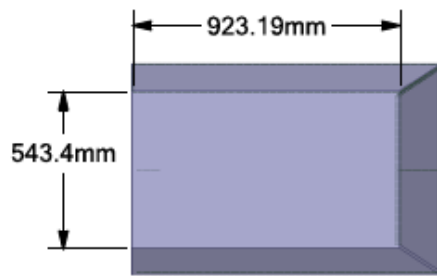
Top view



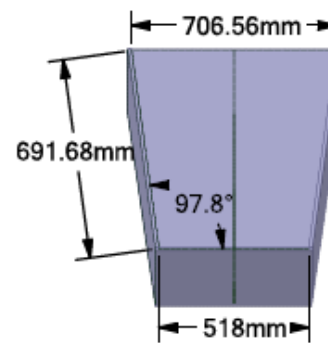
Left view



Side view



Bottom view



Right view

Figure 58. Tundish water model diagram at different views for Plexiglas model construction.

2.2.4 Visualization of the filling stage in the water model

Once the parts of the physical model were constructed, namely the Ladle Shroud and water modelling Tundish-tank, the parts were put in place. The Ladle Shroud model was attached with three steel arms to the existing slide gate in the MMPC laboratory, as per Figure 59. To respect the distance between the ladle shroud and the Tundish's bottom of 8 inches the Tundish is sitting on an aluminum support. This construction was made to respect the industrial distance between the Tundish-tank bottom and at the Ladle Shroud's exit. The aluminum support frame is sitting on an existing large Tundish tank from a previous setup in the MMPC water modelling laboratory. Before the experiments, water tests were carried out to determine the inlet flow, based on the existing slide gate aperture. The slide gate opening for a 0.8 m/s inlet velocity (1.6 L/s) was determined to be approximately equal to a quarter opening of the slide gate nozzle.



Figure 59. Ladle Shroud physical model attached to slide gate at the MMPC laboratory.

Video recordings of the filling stage of the system with water was done, to analyze and compare with the mathematical predictions: i. e. the multi-phase flow generated within the Ladle Shroud, steel-argon/air in the industrial set-up system and water-air in the physical model. Additionally, a two-phase (water-air) mathematical model of the filling stage of the physical model with water was performed to validate the qualitative similitudes of the filling stage between the mathematical predictions and water physical model. The mathematical water model was developed using equivalent flow conditions to those developed for the mathematical model of the real process, using the same boundary conditions, except that the tundish geometry was based on Figures 55, 56 and 58; i. e. the inner diameter of the ladle shroud was averaged at 70mm, vs flaring from 65 to 75 mm. in practice. The argon injection was omitted in said mathematical modelling as in the current physical model experiment. Figure 60 depicts the geometry generated and used for the exact simulation of the present water physical model. By comparing the “Real Case” mathematical model, the water mathematical model and the experimental water modelling, we confirmed the validity of the mathematical model. We also provide a baseline for future qualitative and quantitative analyses of the flow behavior in the present Ladle-Shroud system; such as, argon shroud physical analysis, inclusions and bubbles tracking, together with measurements with LiMCA and its water analogue system APS III (Aqueous Particle System) [43].

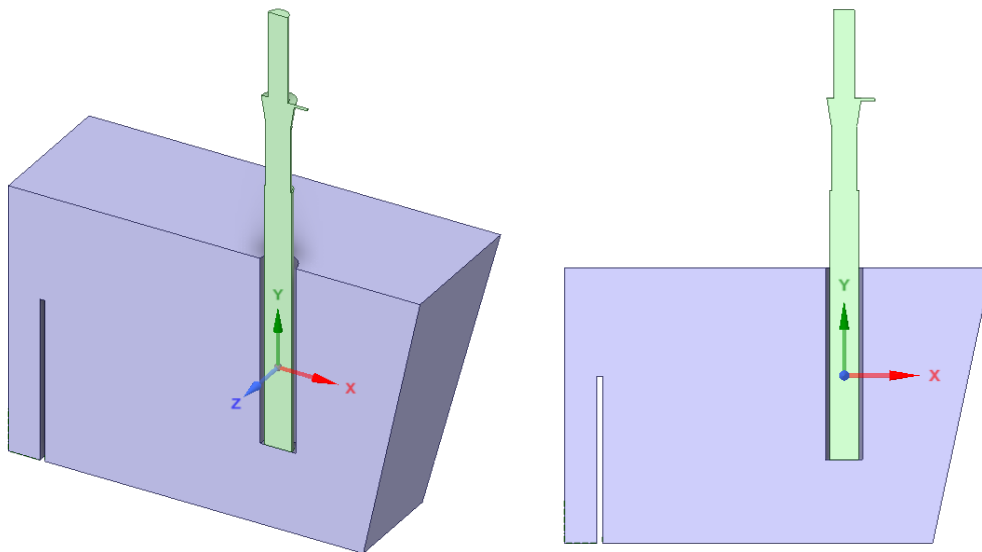


Figure 60. Geometry generated in SpaceClaim © for the water-air mathematical model.

Figure 61 depicts the complete experimental set-up, where the slide gate, Ladle Shroud and Tundish-tank are observed in place for experimentation. The position of the Ladle Shroud was adjusted with respect to the Tundish-tank based on Figure 36. One experiment case was performed 3 different times as baseline, using the inlet water flow of 1.6 L/s without gas shrouding and with an airtight seal between the lower nozzle and Ladle Shroud parts. Video recording was taken, with a GoPro Hero 6 © video camara with a 1080p resolution and 40 frames per second, from several views for subsequent analysis. The following procedure was followed to perform the experiment:

1. Fill with water the Ladle-tank reservoir below the slide gate (not shown in the present work) with the slide gate completely closed (0% aperture).
2. Open the slide gate to an approximate 25% aperture and start recording the filling stages of the tank until the 16 inches level is reached when the excessive water will start overflow above the 16 inches tall dam.
3. 20 seconds after the 16 inches level is reached, close the slide gate completely (% aperture) and remove the sliding dam to allow all the water in the tank to exit.

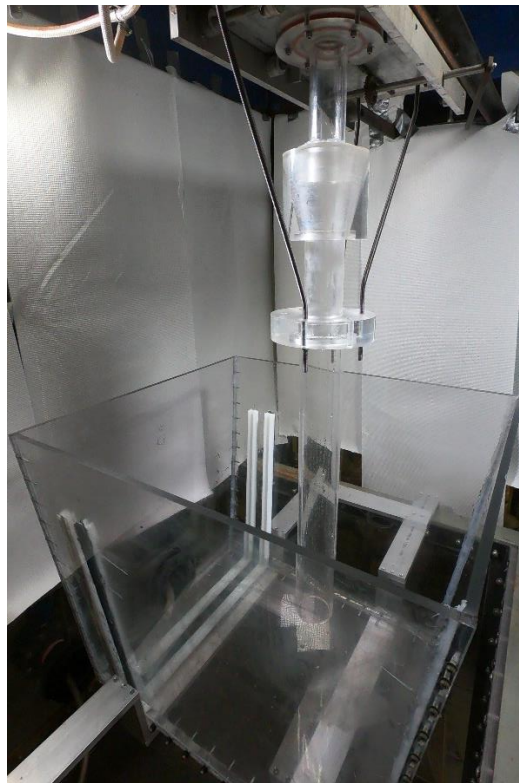


Figure 61. Experimental set-up with water model Ladle Shroud and Tundish-tank

Chapter 3: Results and Discussion

3.1 Mathematical Modelling Results

3.1.1 Simplified case

For the predicted phenomena in the Simplified case analysis, phase volume fraction contours were obtained for the three different phases, at three different stages. Figures 62, 63 and 64 present the predicted volume fraction contours for the three different phases (steel, air, and argon) at the three different times, along the plane of symmetry, during the filling of liquid steel entering the system. Initially, the system is filled with air, air volume fraction=1, but after 0.944 seconds, the falling steel stream reaches the bottom wall of the Tundish. The predicted falling stream thins itself out when accelerating under gravity. As a result, it does not completely fill the Ladle Shroud, whilst the air fraction predominates near the shroud's sidewall. The steel falling stream is preserved throughout the following time steps to 14.452 seconds. There, one sees that argon begins to displace some of the air within the Ladle Shroud. At the same time, as seen on the steel Volume Fraction (VF) contour, the interface between the steel and air, near the bottom wall, has become diffuse. This is due to the continuing acceleration of the steel and the high kinetic energy of turbulence predicted for the system. This promotes breakup of the steel jet. At 29.675 seconds, the predicted steel VF contour, shows that the Ladle Shroud starts to fill with liquid steel near the walls, at the same time the steel level reaches the Ladle Shroud bottom part (around 8 inches steel level). The interface between the steel and air shows a high degree of intermixing between phases. This generated air entrainment (air bubbles) in the steel below the Ladle Shroud, as predicted by its corresponding air VF contour. The predicted argon VF contour at the same time, shows that the argon flow starts to displace the air near the top walls of the Ladle Shroud, however, the argon has still not reached the opposite side of the argon injection port, as observed on the corresponding porous refractory part. At 32.172 seconds, a more quiescent steel fluid is predicted where some gas bubbles are seen floating up, as they reach the bottom part of the Ladle Shroud, per the steel VF contours. However, within the Ladle Shroud, the intermixing between the phases persists. On the corresponding air VF contour, it can be observed that there is still some air, as air bubbles, present in the middle portion of the Ladle Shroud, near its walls. The corresponding argon VF contours predicts that the argon shrouding effect has been achieved at the top part of the Ladle

Shroud, although some air persists near the wall opposite to the point of argon injection. At 37.303, in Figure 64, the different phase volume contours predict big gas bubbles (in the range of 20 mm) within the complete Ladle Shroud, the biggest bubbles being of air, as per the predicted air VF contour. This predicted bubbly regimes progressively diminishes, and at 58.285 seconds, when the steel level has reached its steady operation height (16 inches). A quasi-single-phase flow can be observed with only a few gas bubbles within the system. The argon VF contour at the same time, predicts that as the liquid steel practically fills completely the Ladle Shroud, the argon shrouding effect diminishes as the steel opposes high resistance to the gas injection. Per the predicted results, it can be said, that during the filling stage, a turbulent steel falling stream is generated, promoting the entrainment of air bubbles initially. Afterwards, a turbulent multiphase flow is generating within the Ladle Shroud, where bubbles of around 20 mm are predicted. By quasi-steady state operation, a single-phase flow is predicted, but the argon shrouding effect diminishes. The previous observations will lead to the re-oxidization of the liquid steel, in contact with air bubbles during the filling stage, due to the predicted turbulent multi-phase flow. Additionally, these observations can be attributed to the design of the Ladle Shroud, where a diverging ID design is present. This design is reducing the flow velocity turbulence in the process, compromising the liquid steel quality, during the initial operation stages.

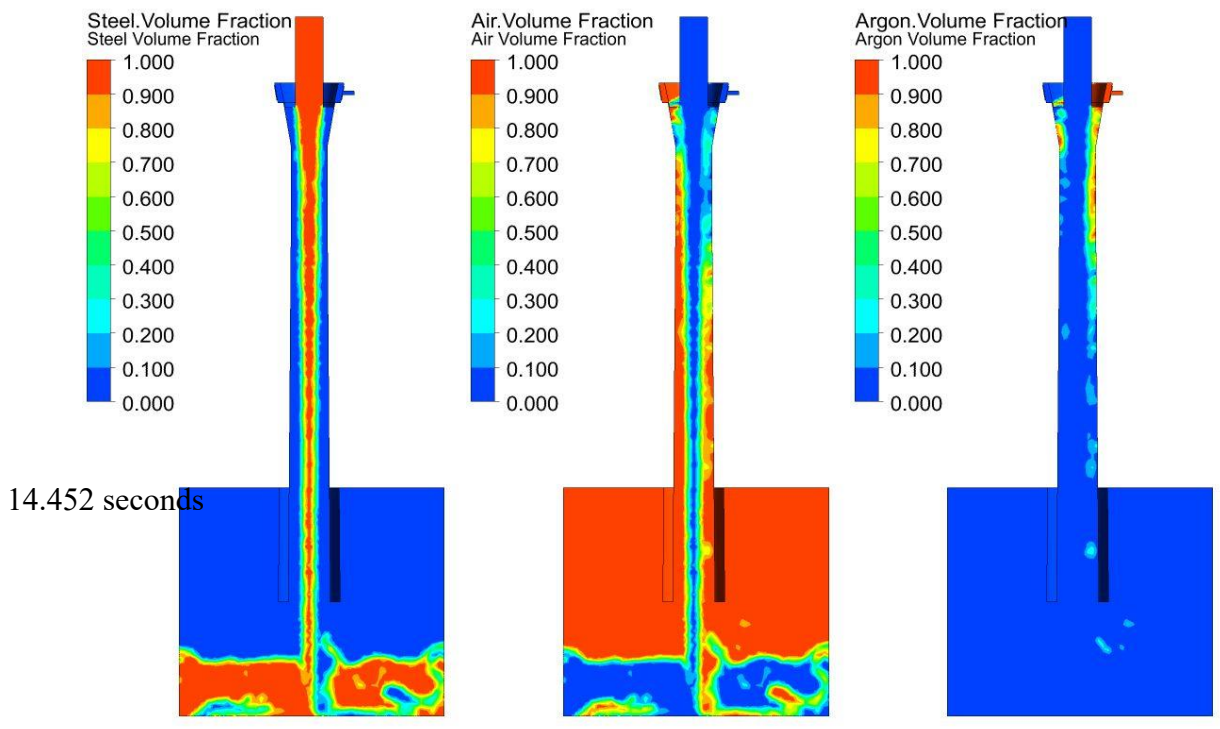
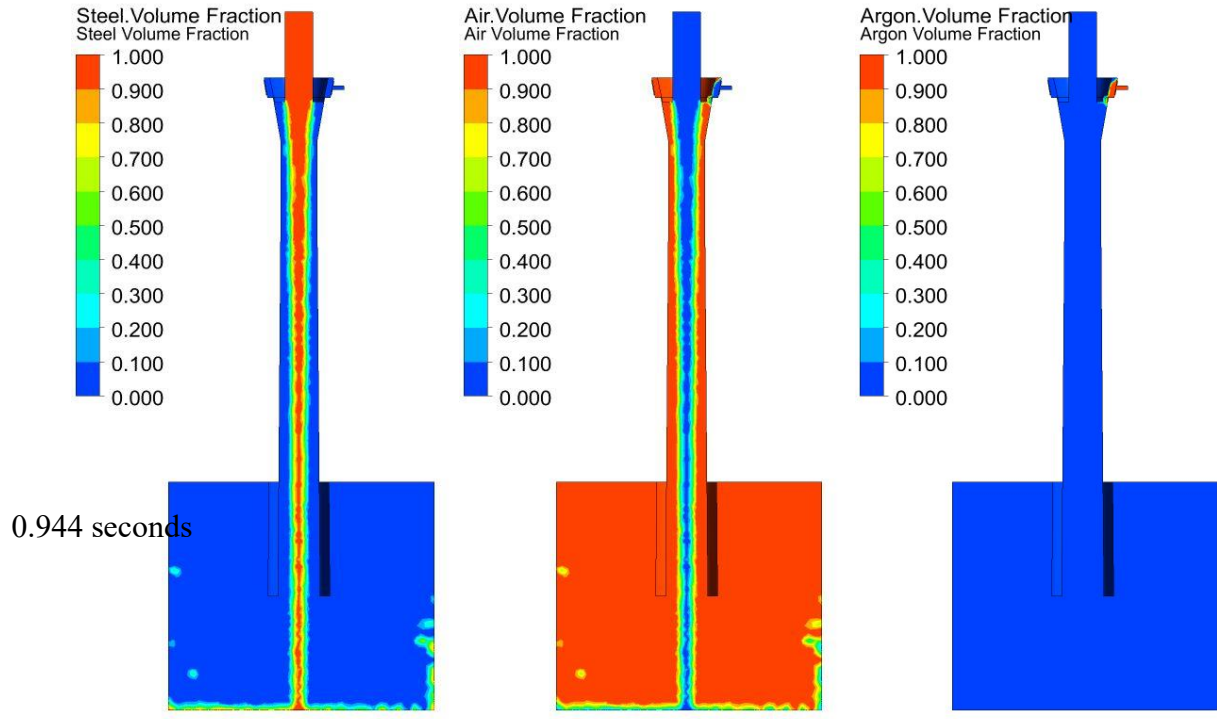


Figure 62. Predicted phase volume fraction contours for steel, air, and argon phases at 0.944 and 14.452 seconds on the symmetry plane.

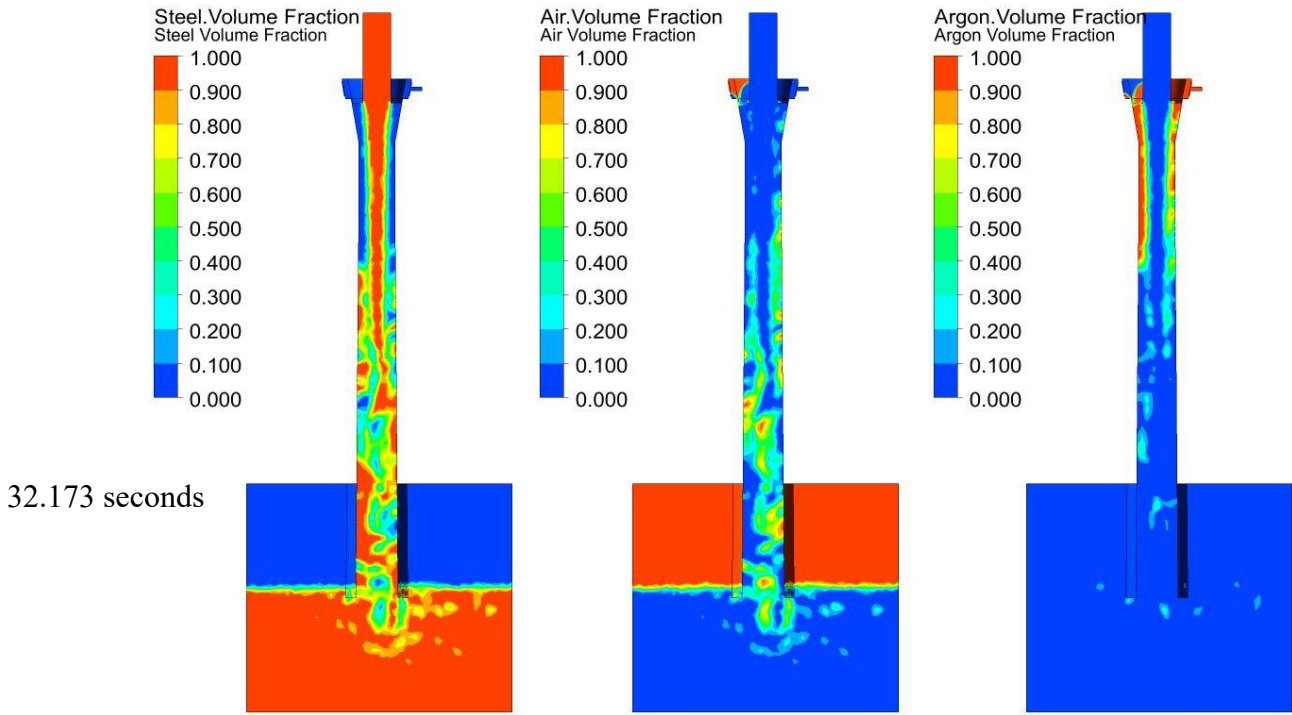
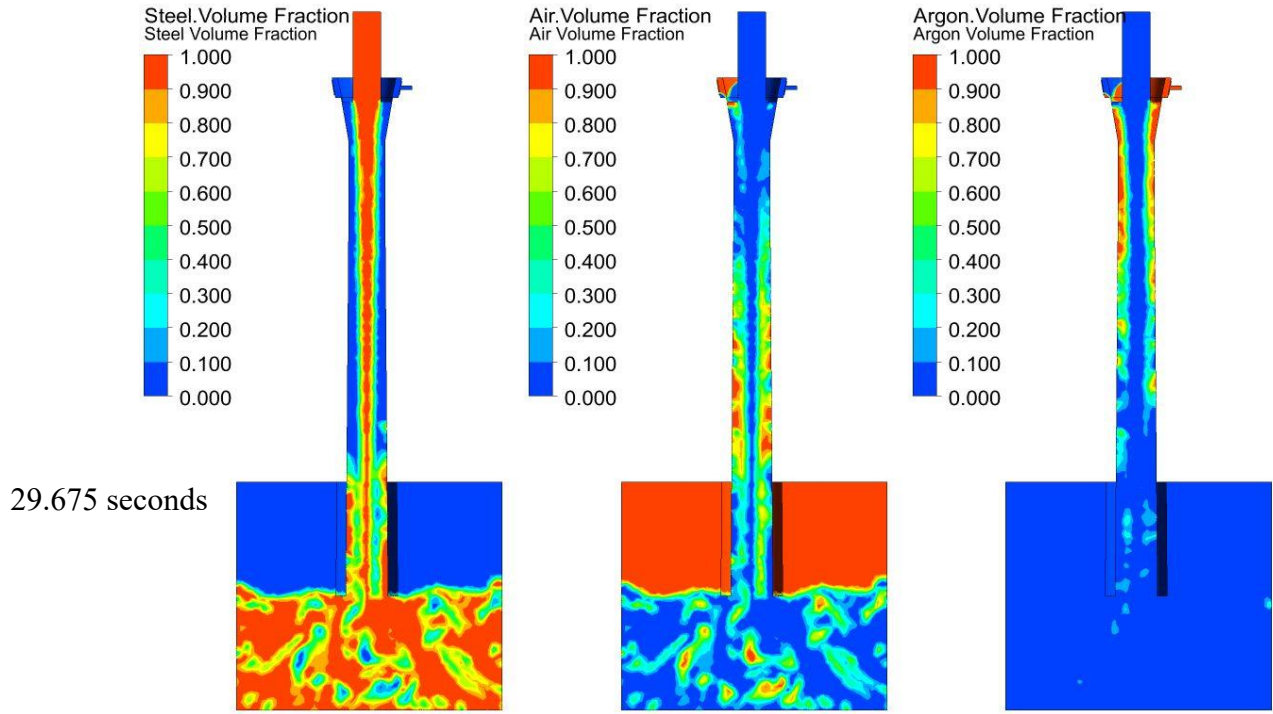


Figure 63. Predicted phase volume fraction contours for steel, air, and argon phases at 29.675 and 32.173 seconds on the symmetry plane.

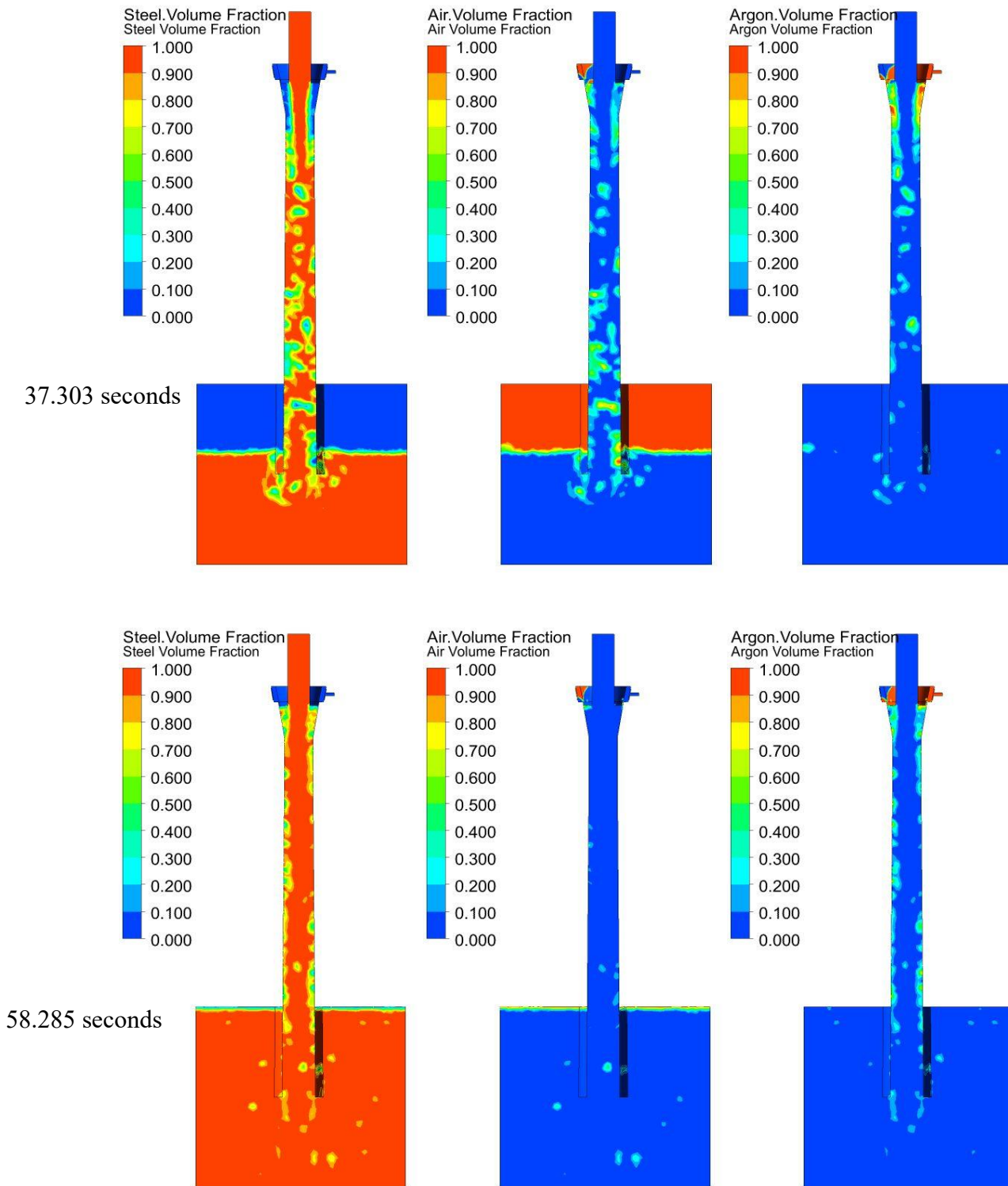


Figure 64. Predicted phase volume fraction contours for steel, air, and argon phases at 37.303 and 58.285 seconds on the symmetry plane.

Figure 65 presents the predicted contours for the absolute pressure, velocity, and kinetic energy of turbulence in quasi-steady state operation, at 58.285 seconds from “start pour”. On the absolute pressure contour, Figure 65 (a), as expected, the absolute pressure is lower in the top portion of the Ladle Shroud, ranging from 0.465 atm, at the top, to 1 atm, at the free surface part, and finally to 1.278 atm, at the bottom wall part of the system. The negative pressure (less than 1 atm) at the top part of the system, namely the lower nozzle-Ladle Shroud overlapped joint, will promote air suction, if a perfect seal is not achieved. This absolute pressure prediction correlates well with the Bernoulli equation, with the following reduced form according to Wang et al. [39]:

$$P = P_0 - \rho_{steel}gh; (0 < h < H) \quad [17]$$

where H , corresponds to the height at the top of the Ladle Shroud system. Table 3.1 presents a comparison between the predicted absolute pressure and the theoretical pressure, according to equation [17]. Similarly, Figure 66 shows the graphic comparisons between both values, and a practically perfect fit can be seen, with a % error maximum of 5.65 % at the top part of the system. Said discrepancy might be related to the high turbulence generated due to the incoming turbulence of the flow, making an over prediction of the pressure. The comparison with equation [17] was made to confirm that the mathematical model developed agrees well with previous single-phase theoretical formulations, but now considering multi-phase interactions, as well as to make sure that the model can adequately describe a gravity driven flow and can follow the Bernoulli equation for a single phase flow system. During the initial development of the model, some difficulties were encountered to accurately reflect the development of a negative pressure predicted by equation [17]. Regarding the predicted velocity contours, Figure 65(b), it can be observed that initial entering flow at 0.8 m/s accelerates at the lower nozzle-Ladle Shroud joint, possibly due to the gas injection contribution. Then deaccelerate progressively forward down to around 0.473 m/s at the exit zone of the Ladle Shroud, which is the main purpose of the present Ladle Shroud diverging ID design. The relative inhomogeneity of the predicted velocity field is attributed to the high turbulence and phase interactions within the Ladle Shroud, making the velocity field highly time dependent. Regarding the predicted turbulence kinetic energy contour, presented in Figure 65(c), high turbulence zones (around $0.045 \text{ m}^2/\text{s}^2$) are observed near the Ladle Shroud walls, due to the turbulence contribution of the lateral gas injection.

The previous results and analysis confirm the negative pressure at the lower nozzle-Ladle Shroud design, predicting an absolute pressure of 0.627 atm, which will generate air suction if a perfect seal is not present. The purpose of the following simulation case, air suction case, is to try to simulate mathematically and quantify the air inflow through a 1.2 mm gap, between the lower nozzle and the Ladle Shroud.

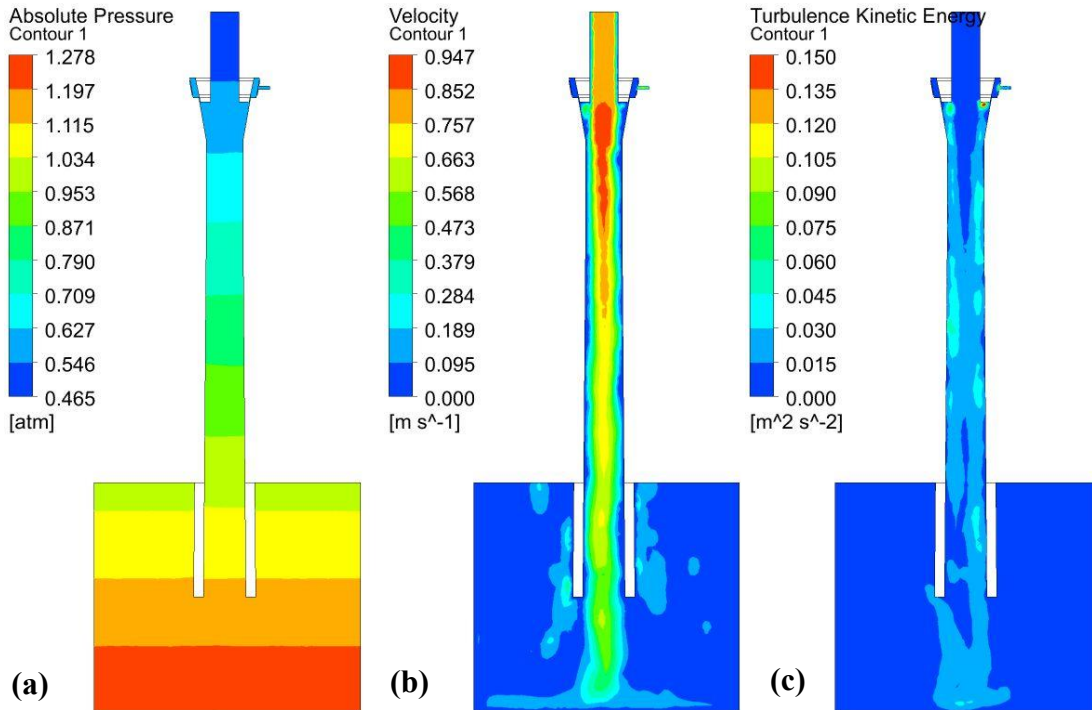


Figure 65. Predicted contours for (a) absolute pressure, (b) velocity, and (c) turbulence kinetic energy at 58.285 seconds (quasi-steady state operation) on the symmetry plane.

Table 3.1: Predicted and theoretical absolute pressure values along the Ladle Shroud system.

<i>h</i> (m)	Pressure (atm)		% Error
	Fluent	Theoretical	
-0.406	1.263	1.275	-0.939
-0.27233	1.168	1.185	-1.390
-0.13867	1.080	1.094	-1.253
-0.005	0.993	1.003	-1.019
0.128667	0.908	0.913	-0.518
0.262333	0.825	0.822	0.285
0.396	0.744	0.732	1.682
0.529667	0.657	0.641	2.496

0.663333	0.571	0.550	3.767
0.797	0.486	0.460	5.647

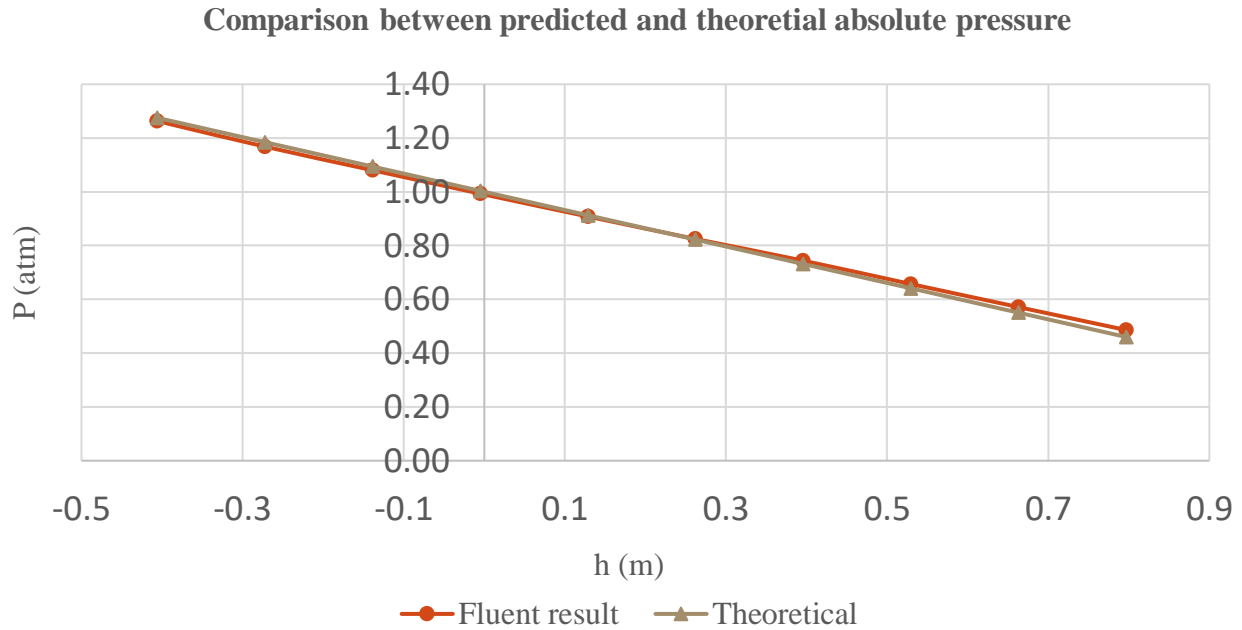


Figure 66. Comparisons between predicted and theoretical absolute pressure along the Ladle Shroud

A summary of the results of the first case, the simplified case, is presented below:

- A turbulent multiphase flow is generated during the initial filling stage of the system.
- Gas bubbles of around 20mm are generated within the Ladle Shroud, air bubbles will promote re-oxidation at the filling stage.
- The argon shrouding flow is not efficient in displacing readily the initial air in the system.
- A negative absolute pressure is predicted at the lower nozzle-Ladle Shroud joint, which will generate an inward air flow if leaks are present.

3.1.2 Air suction case

As explained previously, the process followed to simulate the present air suction case is similar to the predictions performed for the simplified case. Therefore, the steel volume fraction contours during the filling stage are practically the same, since the argon flow only affects slightly the velocity field, in general. Figure 67(a) depicts the steel volume fraction contour at 41.853 seconds, where the Ladle Shroud can be seen practically filled with liquid steel and with some air bubbles

present along the Ladle Shroud. The corresponding absolute pressure contour, Figure 67(b), presents a negative pressure field at the top part, where the absolute pressure at the top portion ranges from 0.416 to 0.582 atm, very similar values to the results already presented in Figure 65(a). The simulation was stopped at said time, 41.853 seconds, to perform the commented boundary condition change from wall to a pressure outlet, to try to obtain an air inflow. Figure 68 shows the predicted steel volume fraction and absolute pressure contours at 42.154 seconds, 0.301 seconds after the boundary condition change. A dramatic change can be appreciated on Figure 68(a), where the steel volume fraction contour shows the zones near the Ladle Shroud walls with a steel volume fraction equal to 0 (blue color), meaning an air volume fraction equal to 1, being a two-phase system. The previous indicates a drastic air inflow in only 0.301 seconds and confirmed with Figure 69, where the velocity contour is presented at the same time of 42.154 seconds. These indicating zones with air velocities higher than 5.0 m/s near the Ladle Shroud walls and an instantaneous air flow of 314.75 L/min of air is predicted through the 1.2 mm gap surface. The absolute pressure contour changed from Figure 67(b) to Figure 68(b) in 0.301 seconds after the boundary condition change, the predicted values within the Ladle Shroud changed to a 1 atm absolute pressure nearly along of its height, since the system is then “opened” to atmospheric pressure (1 atm). The previous computations, prove that the pressure difference between the Ladle Shroud and the atmosphere will generate an important air inflow into the system unless a perfect seal between the mating parts (lower nozzle and Ladle Shroud) cannot be adequately accomplished. This will compromise the quality of the liquid steel, showing the risks of leaks in the system, which will lead to high re-oxidation, and inherently to an important amount of steel reoxidation inclusions. The previous results, additionally, show and quantify for the first time ever, the potential air suction in the Ladle Shrouds via mathematical modelling.

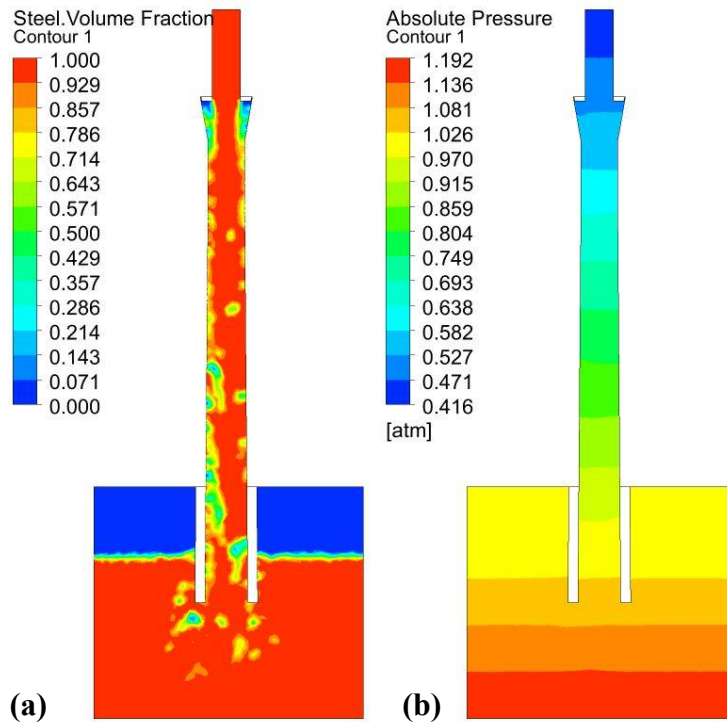


Figure 67. Predicted contours for (a) steel volume fraction and (b) absolute pressure at 41.853 seconds on the symmetry plane.

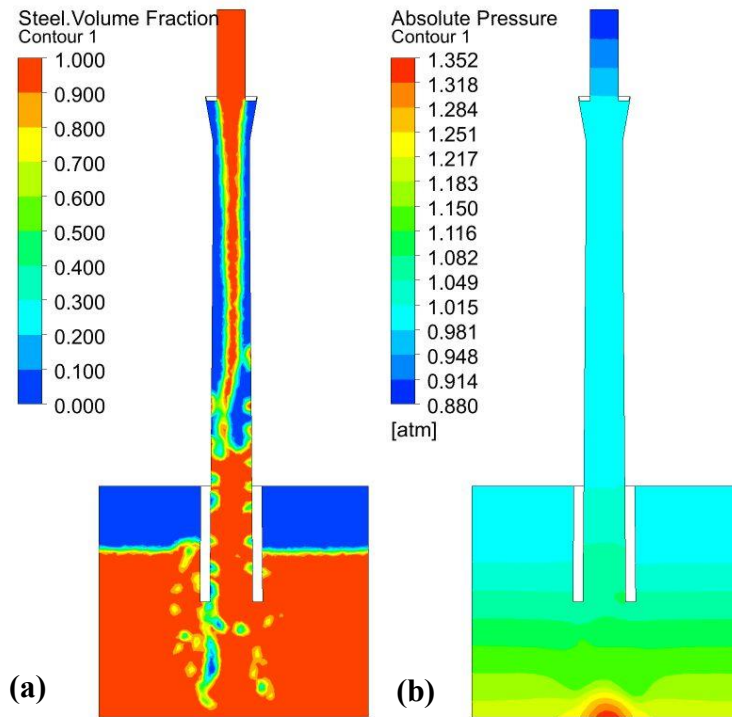


Figure 68. Predicted contours for (a) steel volume fraction and (b) absolute pressure at 42.154 seconds, after change of 1.2 mm gap boundary condition from wall to pressure outlet on the symmetry plane.

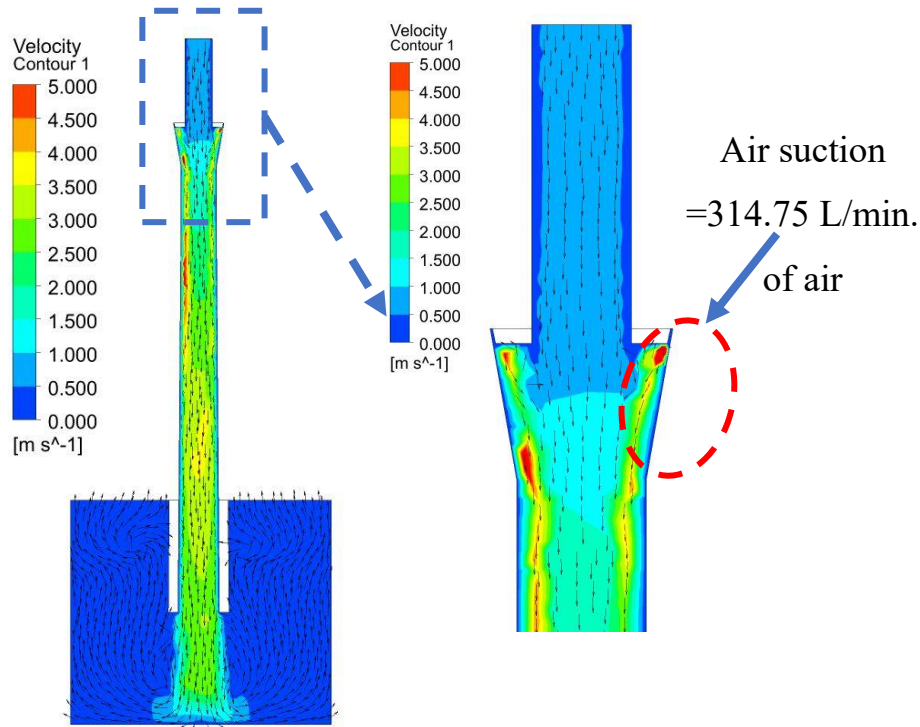


Figure 69. Predicted velocity contour with vectors and detail at the lower nozzle-Ladle Shroud joint at 42.154 seconds on the symmetry plane.

3.1.3 Real case

Similarly, to the simplified case, time dependent phase volume fraction contours for the three phases were calculated for the Real case, and are presented on the symmetry plane in Figure 70, Figure 71 and Figure 72, ranging over timeframes from 0.574s to 77.788 seconds. At 0.574 seconds, the predicted steel volume fraction contour shows that initially the falling steel stream breaks into two streams when reaching the bottom part of the lower nozzle at the joint with the Ladle Shroud, as the ID changes from 50 to around 80 mm. The stream on the right-hand side breaks into steel droplets, due to rapid acceleration, and possibly cross-flow impingement of the transverse flow of argon. However, this effect was not observed in the previous simulations, and it can be assumed that the surface tension forces contributed to the prediction of the initially observed falling steel droplets. At 4.018 seconds, the falling steel stream stabilizes into one single stream, similar to results predicted from previous cases. The stream then collides with the Turnflow at the bottom, generating splashing. One can observe steel droplets ejected to considerable heights near the curved wall, on the right-hand side of the tundish. The corresponding argon volume fraction contour, at the same time, shows that the argon shrouding effect is more

distinct on the side of its injection, whilst the argon barely reaches the opposite left side at 4.018 seconds. Figure 71 presents the predicted phase volume fraction contours at 13.249 and 30.057 seconds. The steel and air volume fraction contours predict that some air entrainment at the right-hand side near the Turnflow walls will be produced due to the high incoming turbulence of the steel stream at 13.249 seconds. Said gas bubbles will be consistent throughout the filling stage. The corresponding argon volume fraction contour, at the same time, predicts a more even and symmetrical gas distribution in the top part of the Ladle Shroud, reaching almost half of the Ladle Shroud height. At 30.057 seconds, when the steel level is about to reach the bottom of the Ladle Shroud, air bubbles can be observed within the liquid steel, practically all along the domain width, according to the steel and air contours. The maximum size of the air bubbles is around 20 mm diameter. The corresponding predicted argon volume fraction contour shows an asymmetrical argon distribution along the Ladle Shroud, probably due to the complexity of the phase interactions and the need of the argon flow to overcome the steel surface tension force to maintain a constant flow along the Ladle Shroud. Additionally, few argon bubbles can be observed on the symmetry plane, but predominantly the present gas bubble correspond to air at 30.057 seconds. Figure 72 shows the phase contours at 35.364 and 77.788 seconds, at the final stages of the filling process. At 35.364 seconds, the Ladle Shroud starts to fill inside with steel, according to the steel phase contour, generating a highly multi-phase turbulent flow inside, as seen for the simplified case. The corresponding air volume fraction contour shows that there still remains air within the Ladle Shroud, that has not been eliminated from the system at 77.788 seconds. At that moment in time, the steel height reaches its steady-state operating level of 16 inches. However, the predicted steel and argon contours present gas bubbles, within the Ladle Shroud and some bubbles on the liquid steel in the Tundish. The predicted sizes of the argon bubbles are similar to those for the previously observed air bubbles. The argon shroud distribution at the top part of the Ladle Shroud, now presents a stable and symmetrical distribution under quasi-steady state operation, presenting a *partial liquid free jet* regime, as defined by the work of Singh *et al.* [35, 36].

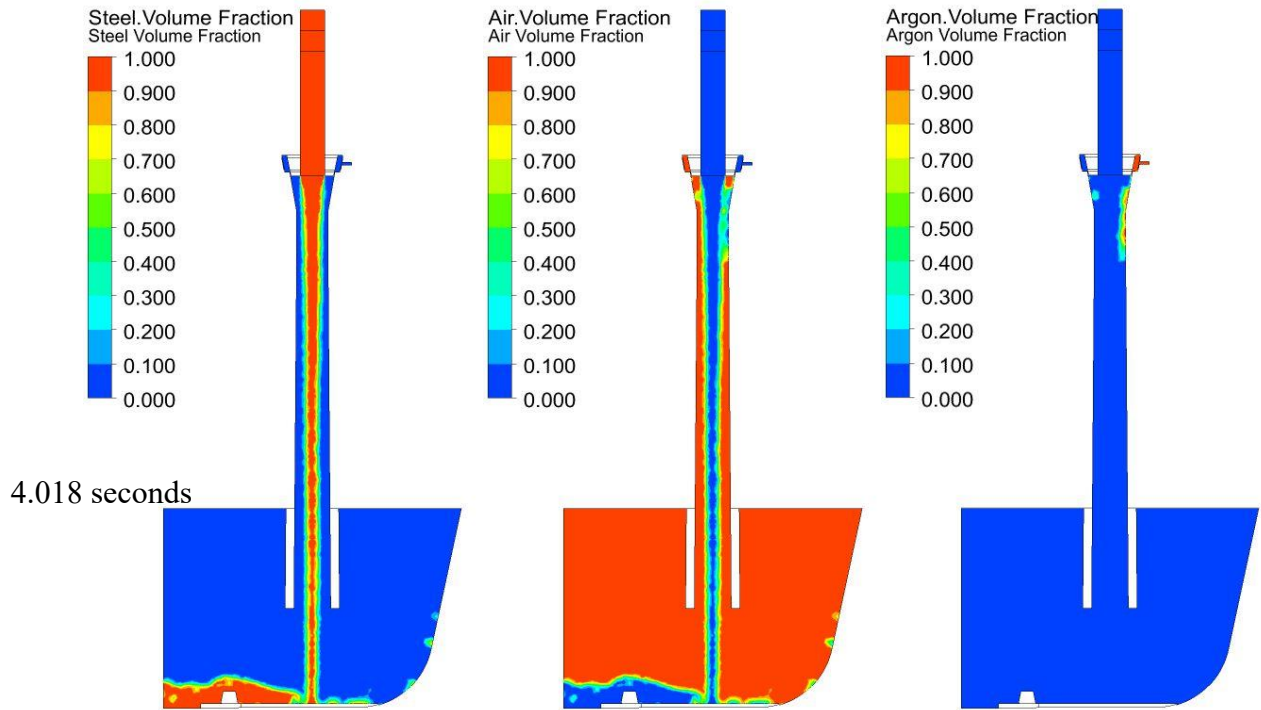
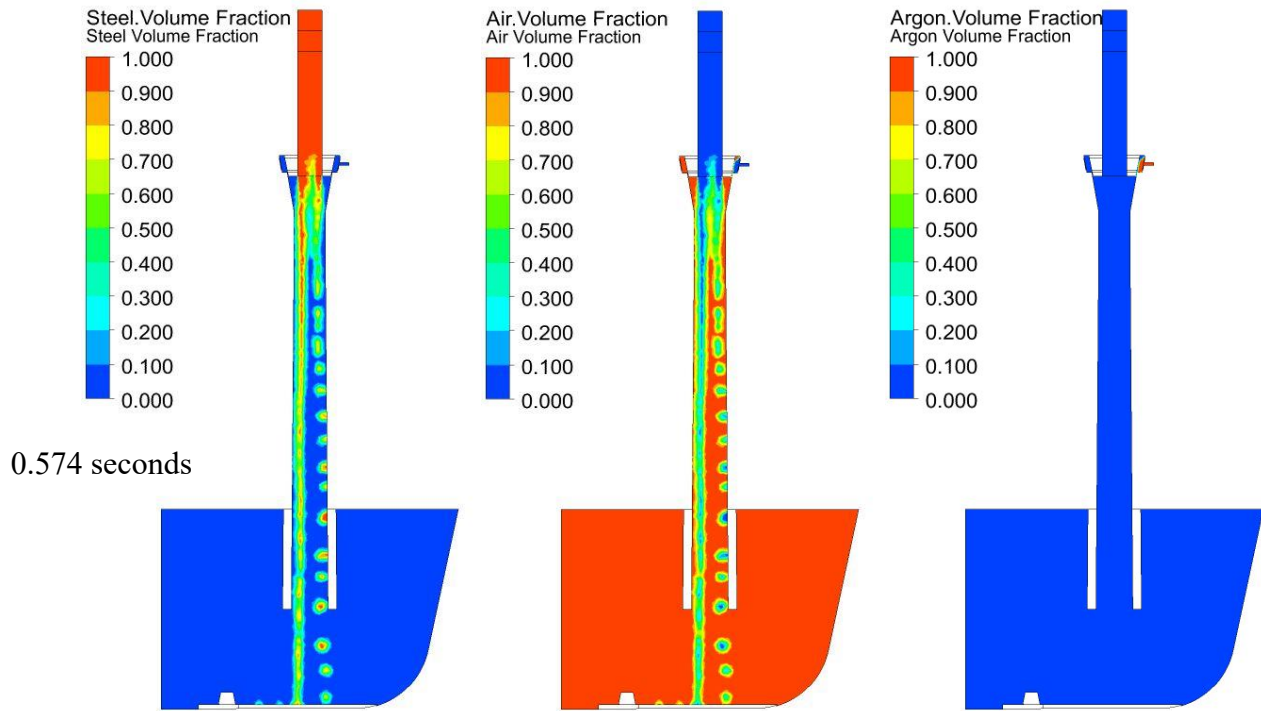


Figure 70. Predicted phase volume fraction contours for steel, air, and argon phases at 0.574 and 4.018 seconds on the symmetry plane.

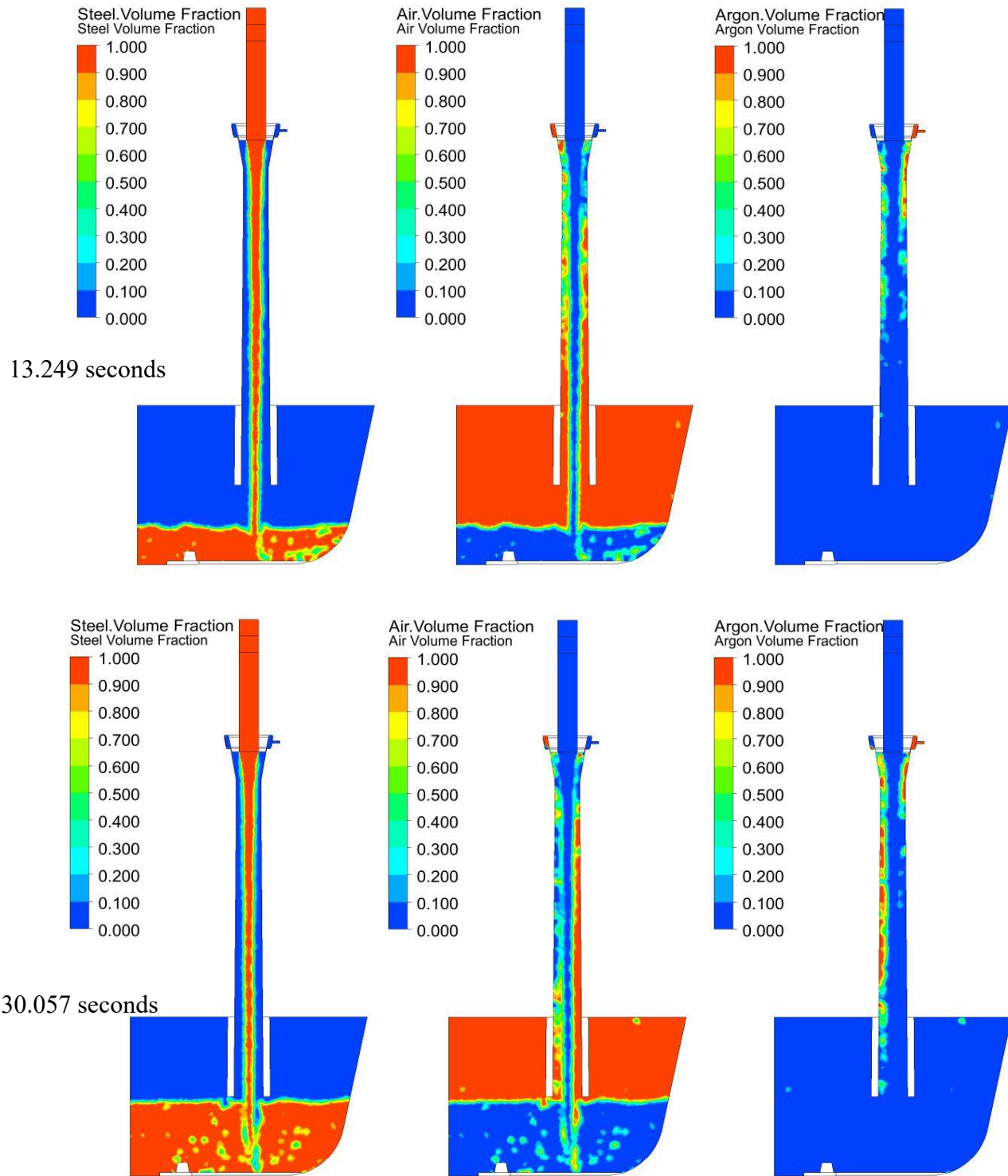


Figure 71. Predicted phase volume fraction contours for steel, air, and argon phases at 13.249 and 30.057 seconds on the symmetry plane.

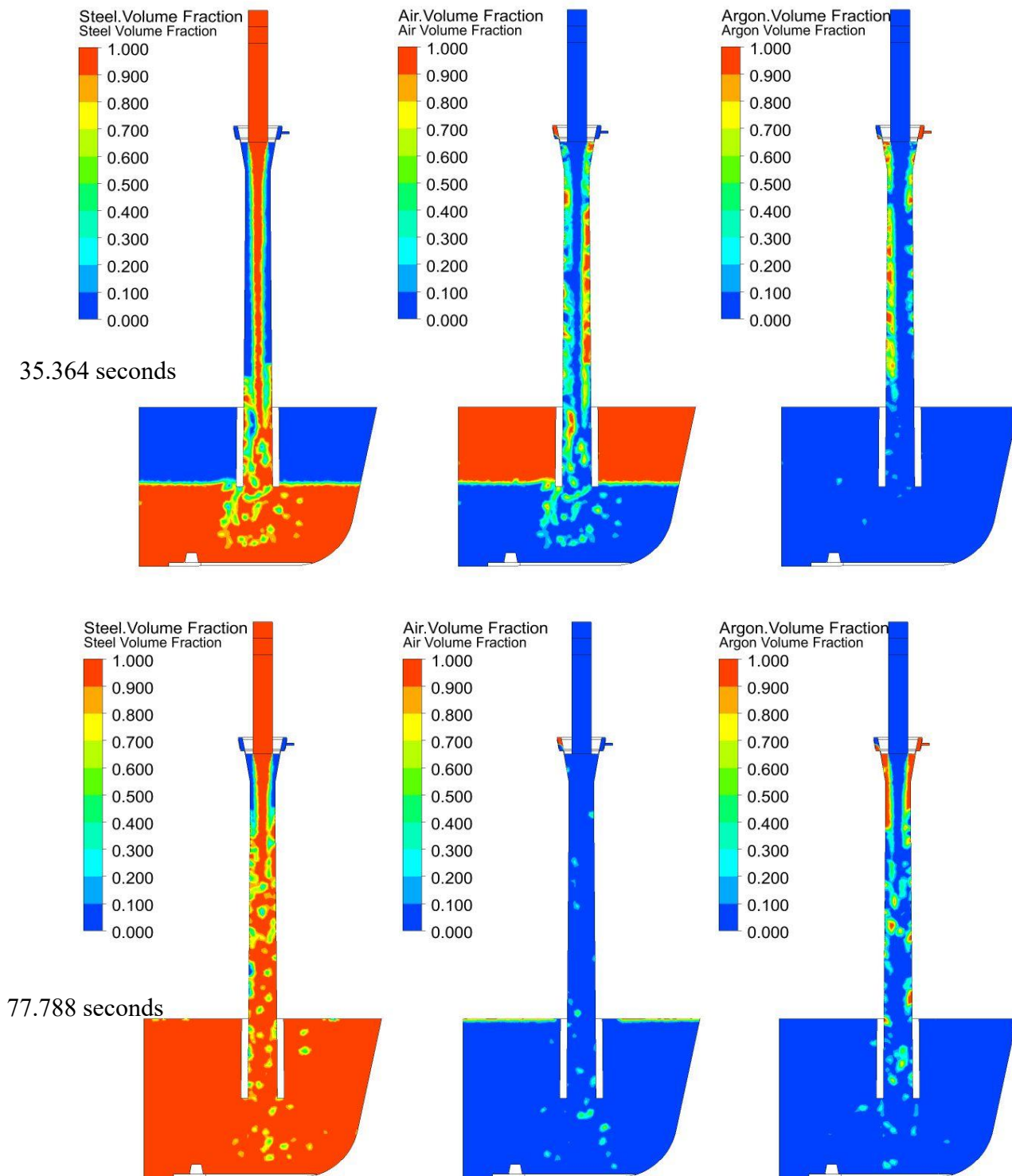


Figure 72. Predicted phase volume fraction contours for steel, air, and argon phases at 35.364 and 77.788 seconds on the symmetry plane.

To complement the previous results for the different phases on the symmetry plane, 3D visualizations of the simulation were generated via Volume Rendering, where the volume is split in 100 planes parallel to the symmetry plane to obtain an inner view of the filling stage at different time steps for the steel volume fraction only. Figure 73 and Figure 74 present said results in an isometric view towards the inside of the system, from 0.574 to 80.011 seconds. At 0.574 seconds, the two diverging streams can be observed again, which then stabilize into a single stream at 3.276 seconds. At that moment, the splashing is readily evident and dramatic, with steel droplets reaching almost to the end of the calculation zone on the vertical +y axis. This can partly be attributed to the effect of the turnflow during the initial time steps, as its walls redirect the liquid steel into the back part of the entering zone, generating splashing mainly on the right-hand side. Afterwards, at 4.993 seconds, the splashing height diminishes, as the flow then becomes more quiescent at 7.202 seconds, where gas (air) bubbles start to become present within the liquid steel. At 17.299 seconds, the presence of gas bubbles is more evident and at 32.506 seconds, the gas bubbles are extended widely throughout the liquid steel in the Tundish entry zone, with some bubbles even reaching the back wall of the Tundish. At the same time, the single falling steel stream “breaks”, generating turbulent intermixing of the phases inside the Ladle Shroud. Figure 74 presents the predicted 3D steel volume fraction volume rendering at 35.364, 40.110 and 80.011 seconds. As the steel level keeps rising within the Ladle Shroud, (around 8.5 inches height at 35.364 seconds), the gas bubbles start to be confined near the exit zone and are less extended within the liquid steel, as the flow within the Ladle Shroud starts to present high intermixing between the three phases, confining the gas bubbles mainly within the Ladle Shroud. Then at 40.110 seconds, this effect increases as a highly turbulent flow is appreciated along the Ladle Shroud. At 80 seconds, when the steel level reaches 16 inches, a predominantly bubbly argon flow regime is predicted, with the presence of argon bubbles along the Ladle Shroud in a quasi-steady state operation. The size of said argon bubbles is around 15 mm diameter, which when reaching the surface, can be expected to disturb the overlaying 1.5-inch slag layer, and promote slag carry-over in the form of small inclusions.

A four-phase study, adding the slag phase to the simulation, is necessary to address the effect of the argon injection on the Tundish Open Eye (TOE) and potential slag entrainment, using completely the VOF multi-phase instead of a DPM-VOF models combination [17], where the argon bubble size is pre-assumed and homogenous. However, as observed by the present result, this might be an important under-estimation of the phenomena occurring within the Ladle Shroud.

Figure 75 shows the predicted velocity and turbulence kinetic energy contours at 80.011 seconds on the symmetry plane, under quasi-steady state operation. The velocity field, Figure 75 (a), predicts an important acceleration of the flow in the zone where the falling steel stream encounters the perpendicular argon injection. The stream then progressively slows, until reaching an exit velocity from the Ladle Shroud of around 0.5 m/s. Therefore, the Ladle Shroud design fails to decelerate the steel flow considerably from 0.8 to 0.5 m/s, that being the main purpose of the diverging ID Ladle Shroud design. The turbulence kinetic energy contour, Figure 75 (b), shows a high turbulence zone at the top part of the Ladle Shroud (maximum values of $0.5 \text{ m}^2/\text{s}^2$), due to the interaction between the liquid steel and the argon injection. That will lead to wall shear stress values of around 15-30 Pa on the Ladle Shroud wall, according to Figure 76, generating higher wall shear stress on the Ladle Shroud walls than on the Turnflow walls, where values of 3 to 6 Pa are predicted.

Through the analysis of the results of the real case, the following summary can be extracted:

- A highly turbulent multiphase flow is generated during the initial filling stage of the system, generated by the collision of the falling steel stream with the walls of the Turnflow.
- Steel stream “breakage” is observed when the steel level reaches the bottom part of the Ladle Shroud, promoting the generation of air bubbles (~20 mm).
- The total volume of air bubbles within the liquid steel in the Tundish decreases with time, meaning that at a higher level of steel in the Tundish, the air fraction within the bubbles will gradually decrease within the steel.
- The effective displacement of the initial air in the system, effected by the injection of liquid steel, and argon into the shroud, is a relatively slow process (33 to 70 seconds), making the steel very prone to reoxidation during that period.

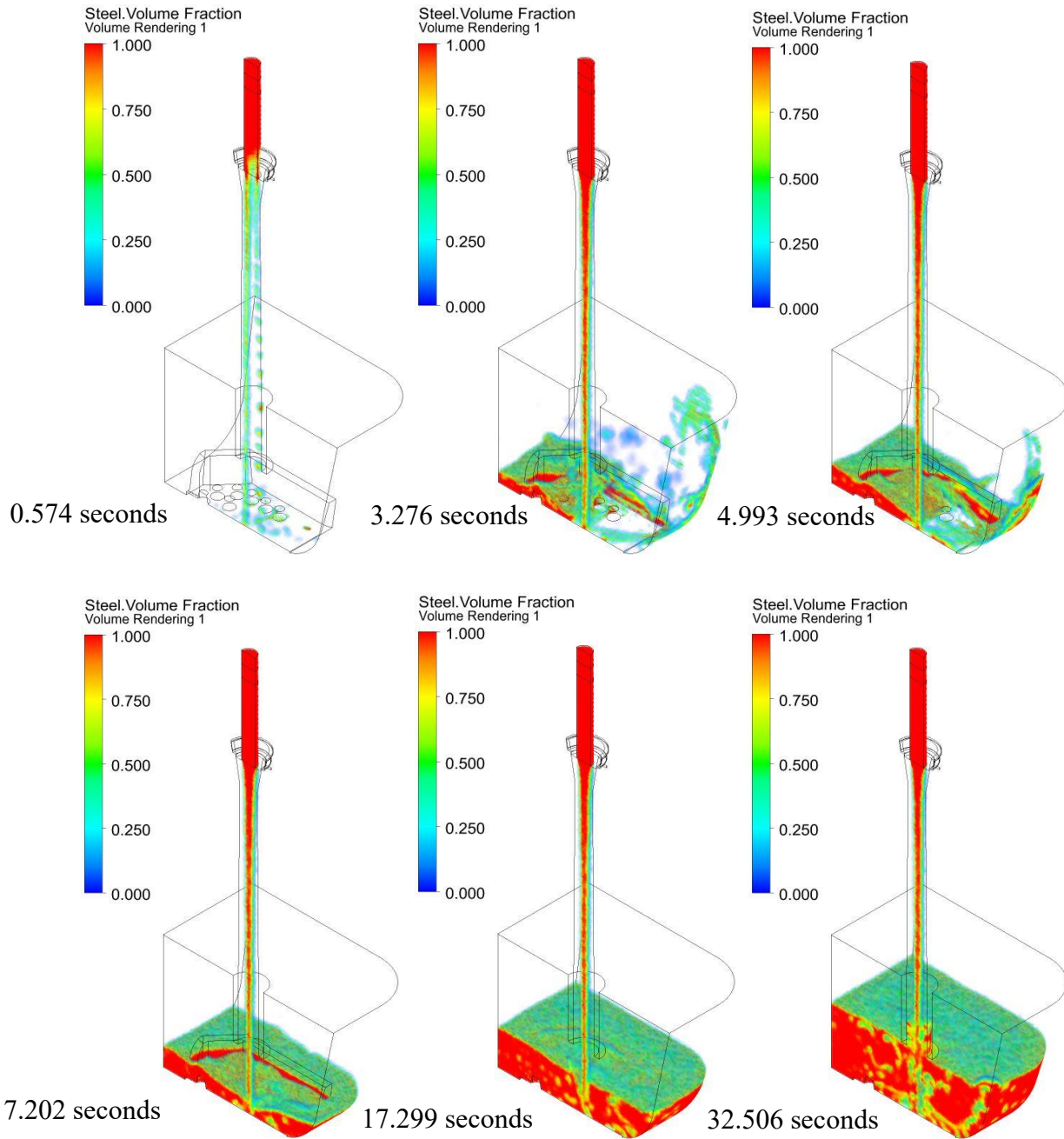


Figure 73. Predicted steel volume fraction 3D contours at different times in isometric view.

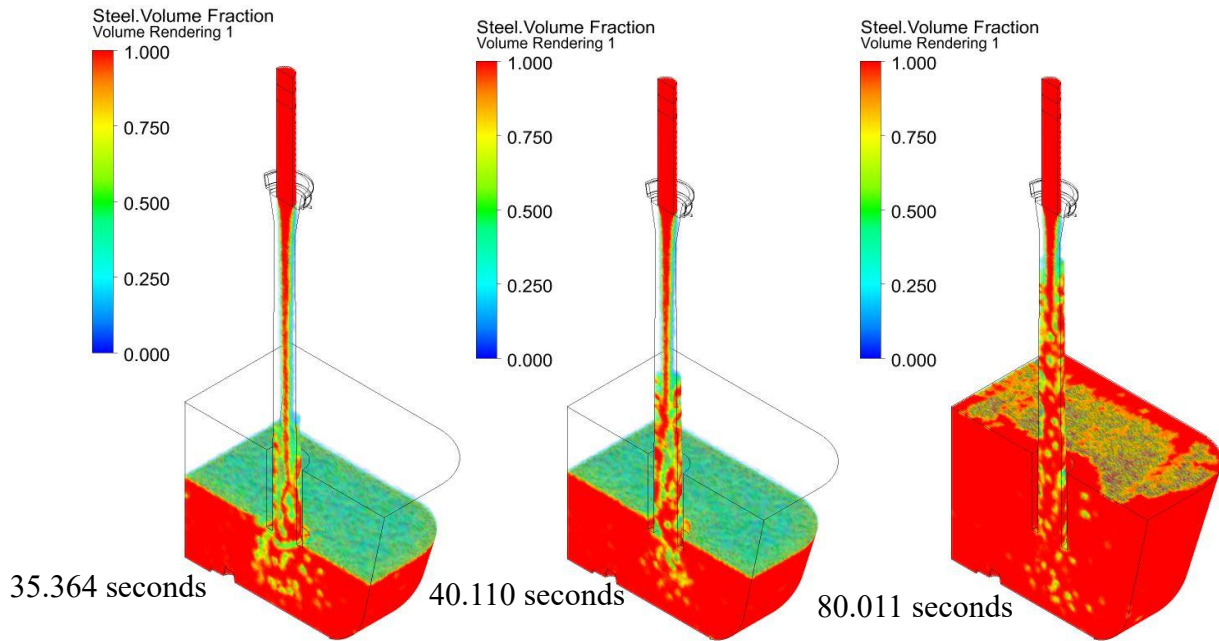


Figure 74. Predicted steel volume fraction 3D contours at different times in isometric view.

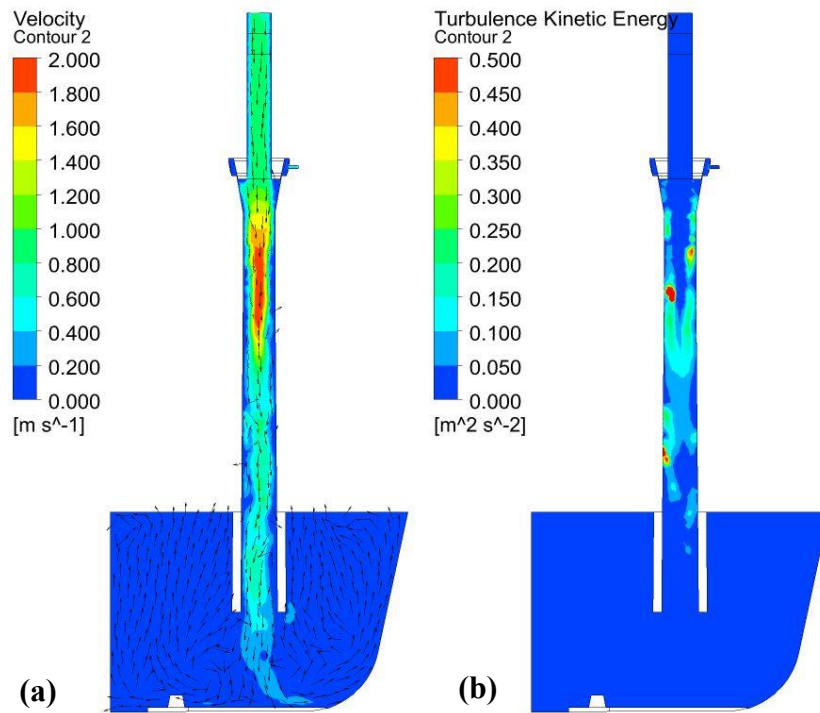


Figure 75. Predicted velocity and turbulence kinetic energy contours at 80.011 seconds on the symmetry plane.

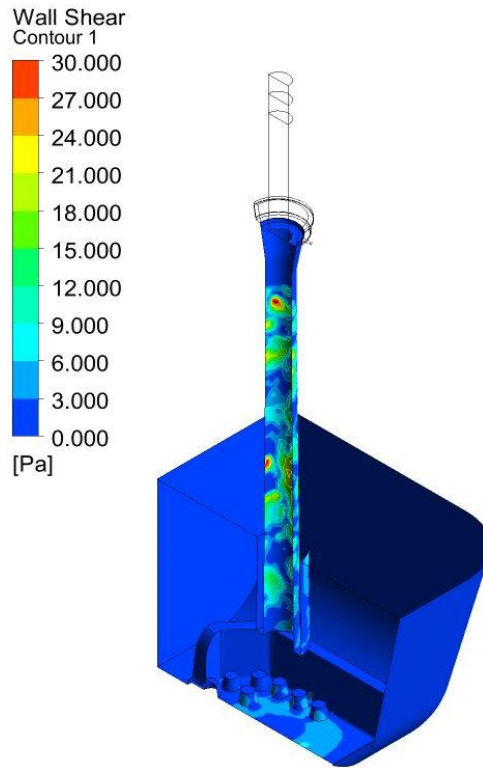


Figure 76. Predicted wall shear stress on the Ladle Shroud walls and Tundish at 80.011 seconds in isometric view.

3.2 Physical Modelling results

As commented in the Physical Model Methodology, Section 2.2, three experiments were performed with an inlet flow of 1.6 L/s and video recordings were captured for different views. Figure 77 shows frames at different times from the slide gate opening in an isometric right-hand top view of the water model experiment. Figure 78 presents similar results, but in a front view. In the three different frames, at 5, 30 and 60 seconds, it can be observed that regardless of the filling stage, the Ladle Shroud is never completely full of water. Rather, a highly turbulent two-phase flow develops within the ladle shroud. Additionally, in Figure 78 (c), a high number of bubbles in the water can be observed, encompassing almost all the zone adjacent to the Ladle Shroud exit zone again due to the turbulent flow presented within the Ladle Shroud. Figure 79 presents a closer view of the air bubbles emerging to the liquid surface in the Tundish-tank, encompassing almost completely the water surface during quasi-steady state operation and reaching all the depth of the liquid

These experimental observations confirm the mathematical results, which correctly predicted a multi-phase turbulent flow inside the Ladle Shroud, promoted by the diverging ID design, where a falling liquid stream is generated in the lower nozzle-ladle shroud connection.

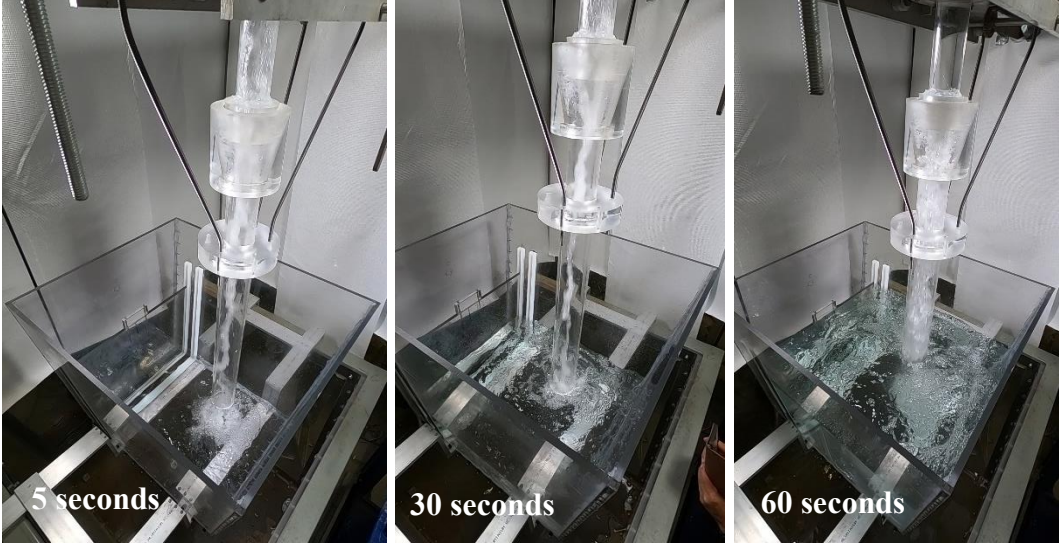


Figure 77. Filling stages of the Ladle Shroud-Tundish-tank water model at (at different times from an isometric right-hand top view).

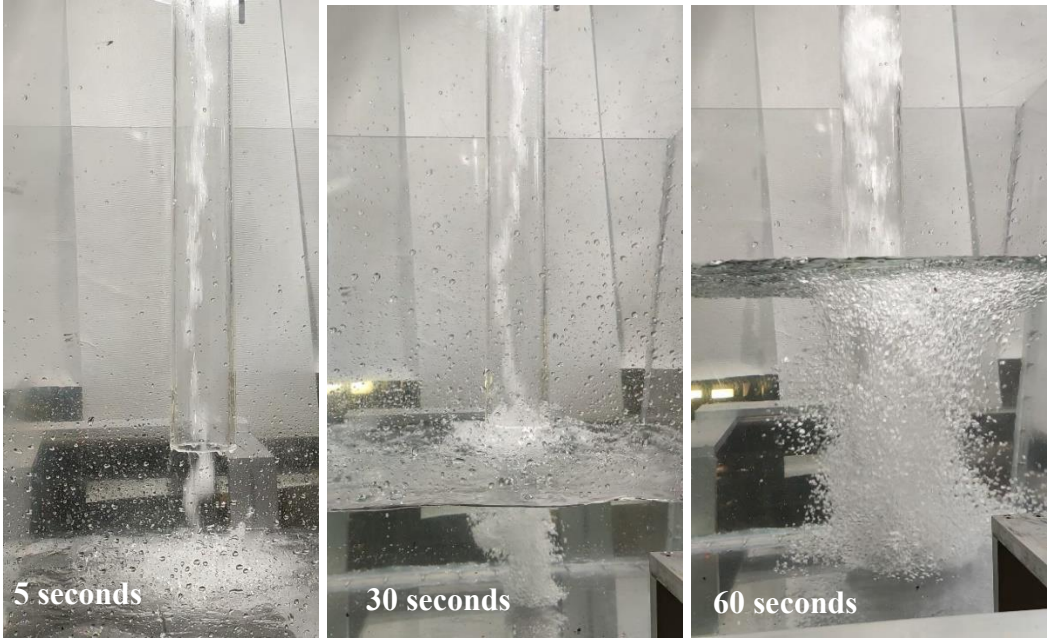


Figure 78. Filling stages of the Ladle Shroud-Tundish-tank water model at different times from front view.



Figure 79. Air bubbles generated in the liquid in the Tundish-tank surface in (a) front view and (b) isometric view.

To assess the qualitative validity of the mathematical model results, a comparison of the obtained liquid phase volume fraction volume contours of the Real Case results (Section 2.1.9) and the described mathematical and water model results (Section 2.2.4) is presented in Figures 80, 81 and 82. There, it can be observed that the predicted behavior of the falling stream (steel or water) is confirmed by the experimental results. Initially, the falling stream collides with the Tundish floor to generate liquid splashing. This is more pronounced at the curved edges, as per the Real Case result, Figure 80 (a). Under half-filled, and fully filled, conditions, it is evident that more gas bubbles are predicted in the Real Case Scenario. However, the amount of air bubbles generated is remarkable. A quantitative validation will be made by measuring the velocities in the physical model to compare with the mathematical predictions. The air suction phenomenon can be quantified by generating a 1.2 mm gap at the lower nozzle-Ladle Shroud connection, in order to measure the air suction, similar to the work of Singh and Mazumdar [35]. This can then be compared with the value obtained in for the Air Suction case of the mathematical model. This quantitative validation is expected to be part of future projects.

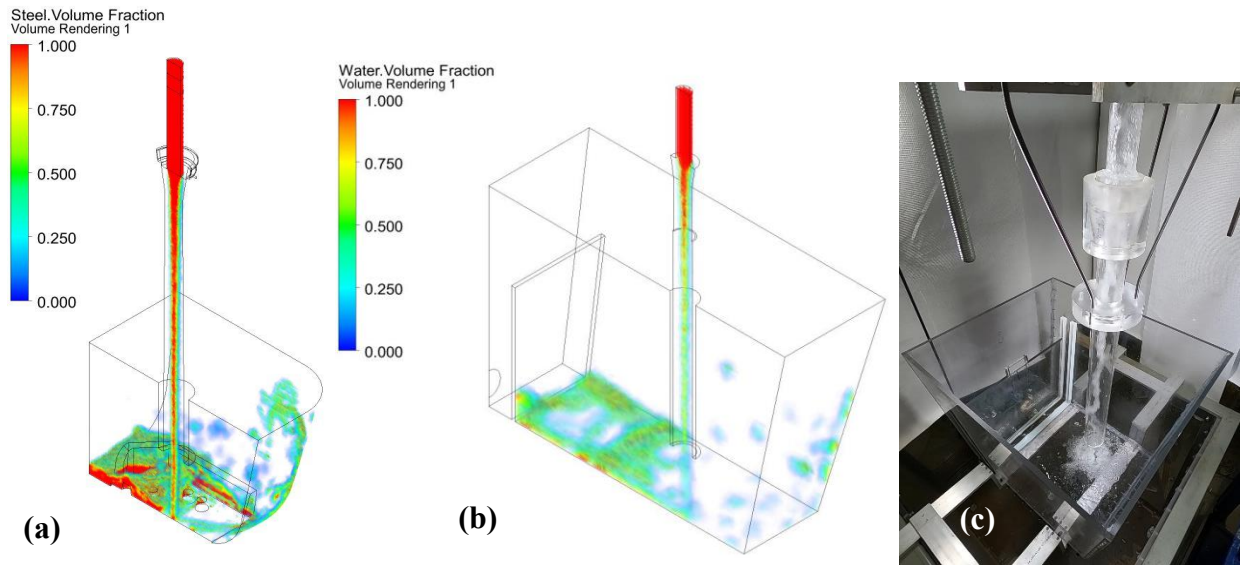


Figure 80. Comparison of the filling stage of the ladle shroud-tundish system at the start of the filling stage. (a) Real Case, (b) Mathematical water model and (c) Water model experiment results

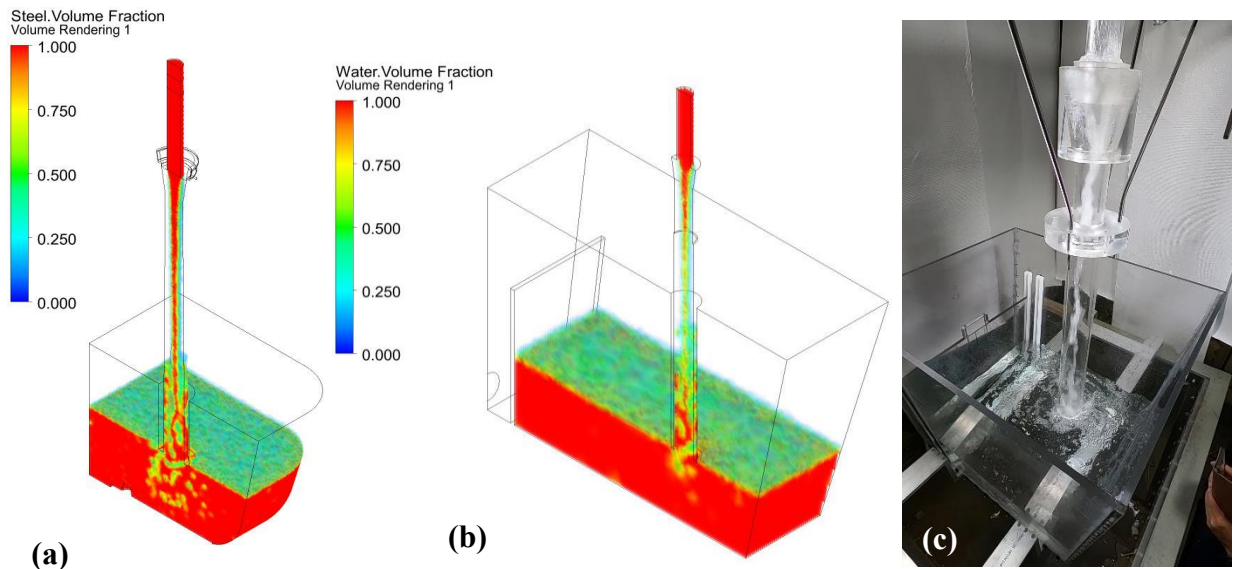


Figure 81. Comparison of the filling stage of the ladle shroud-tundish system at half the time of the filling stage. (a) Real Case, (b) Mathematical water model and (c) Water model experiment results

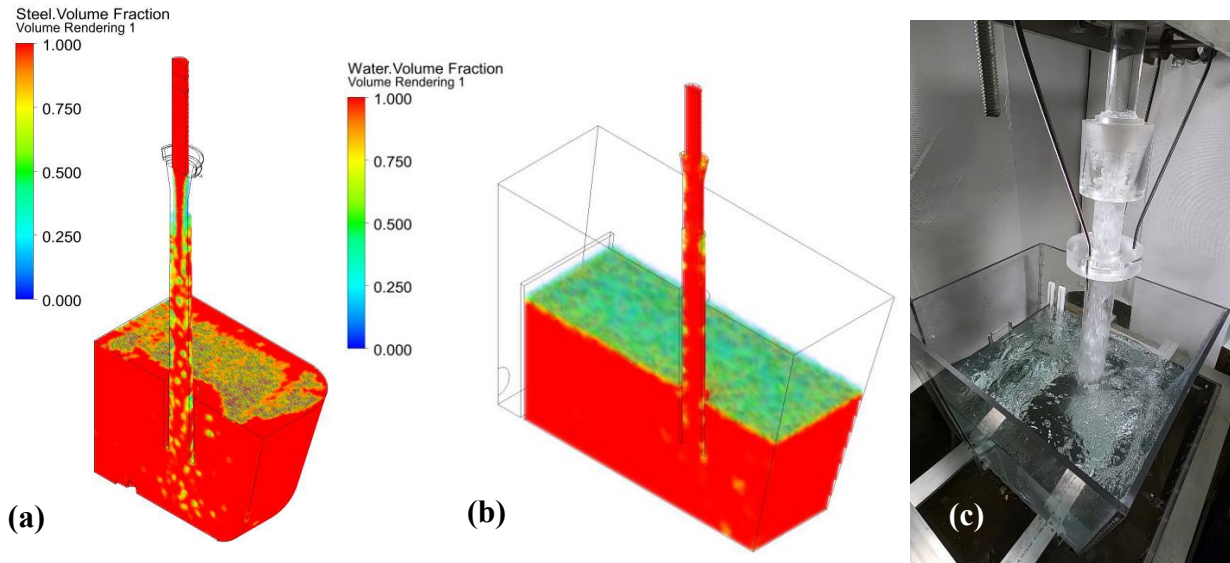


Figure 82. Comparison of the filling stage of the ladle shroud-tundish system at the end of the filling stage. (a) Real Case, (b) Mathematical water model and (c) Water model experiment results

From the previous discussion, it can be said, based on the comparison of the mathematical results and the water model experiments and summarized in Figure 83, that the multi-phase flow within a diverging, or a tapered, ladle shroud involves the following sequence in development: the incoming liquid fills the lower nozzle with liquid, then the falling turbulent liquid stream forms in the lower nozzle-ladle shroud connection/joint to form a multi-phase turbulent flow within the ladle shroud, which subsequently exits the and then finally evacuate the ladle shroud, to form gas bubbles which rise through the liquid surface in the tundish. The previous summary is valid for a no gas shrouding system as well as for gas shrouding system, where an uncontrolled multi-phase flow regime will be present during the filling stage, forming air bubbles of different, uncontrolled sizes. These will promote the reoxidation of the liquid steel, thereby forming oxide inclusions and contaminating the liquid teel in a tundish. For a gas shrouding system, after the filling stage, argon bubbles varying in size will exit through the surface and will perturb the overlaying slag, promoting the formation of slag inclusions.

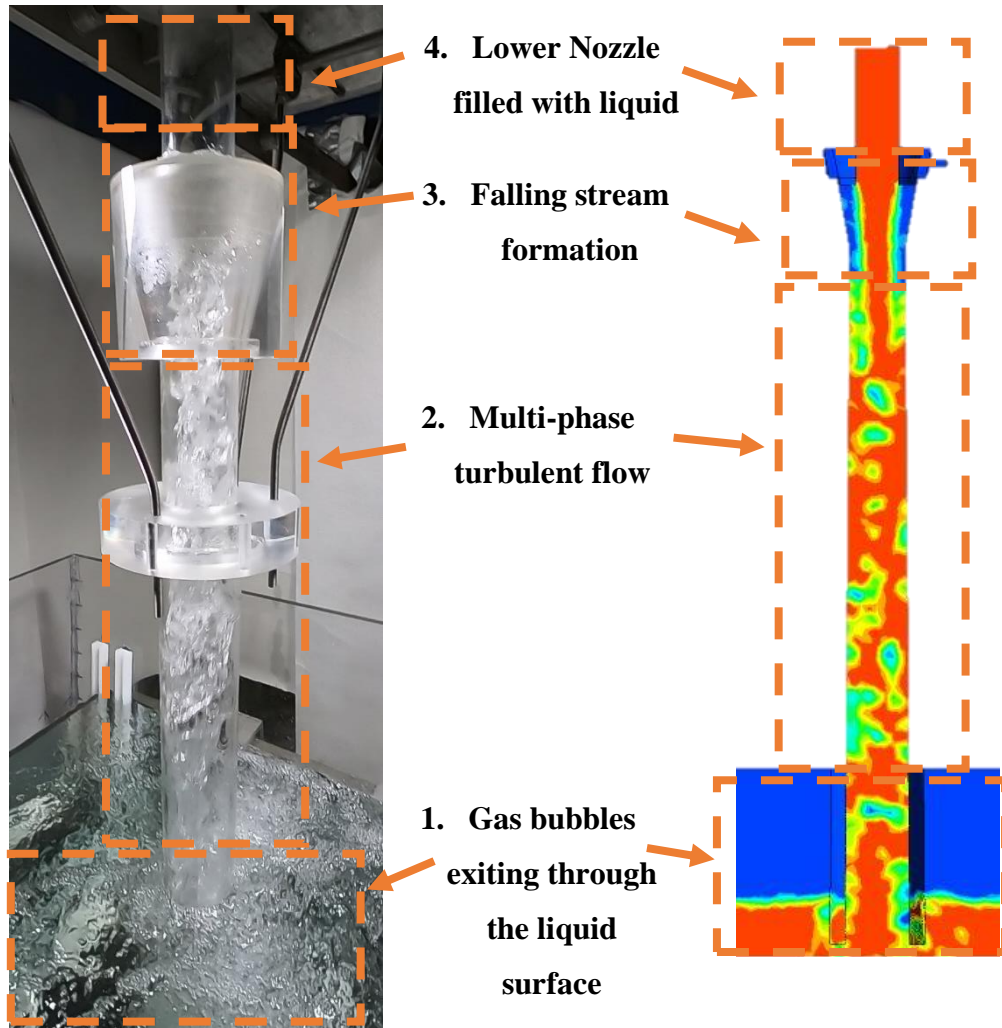


Figure 83. Multi-phase flow development inside a diverging ID ladle shroud in physical and mathematical modelling.

Conclusions

1. A novel transient flow visualization of the filling stage of a tapered Ladle Shroud has been mathematically modeled. This enabled one to create a multi-phase flow visualization of the transient phenomena occurring within the Ladle Shroud-Tundish system, from the start of pouring steel into a tundish, until reaching steady-state conditions. This allowed one to predict, for the first-time ever, phenomena such as steel splashing and time-dependent steel-air-argon interactions.
2. In the multi-phase flow visualization, no chemical interactions were included in these results. However, it is known that liquid steel is prone to re-oxidation during the filling stage of a tundish if liquid steel is in contact with air. This is exacerbated by a diverging design of ladle shroud, which effectively reduces the incoming steel velocity, but will compromise the steel's quality.
3. For a well-sealed ladle shroud, a negative absolute pressure is predicted at the lower nozzle-ladle shroud joint. Otherwise, if leaks are present, this will generate an inward flow of air in the absence of effective argon sealing. This was simulated and quantified for the first time ever, showing that it's possible to have an instantaneous air suction flow of 314.75 L/min for the case modeled.
4. In steady state operation, the two-phase flow (steel-argon) will generate gas bubbles of around 20 mm diameter, exiting the Ladle Shroud, which will most likely perturb the slag layer, generating a Slag Open Eye (SOE), and entrained slag inclusions.
5. The sources of some inclusions can be attributed to the current design and operation the Ladle Shroud and possible solutions will be considered in future research.
6. A full-scale physical model of a Tundish-Ladle Shroud system was successfully built for qualitative validation of the mathematical model and for further experimental and CFD research.

Future Work

The present work, being part of a collaborative project with an industrial partner, has served as a basis for future research work, including:

- The development of a mathematical model including the slag phase to assess the effect of the argon injection on slag entrainment.
- Perform a quantitative validation of the mathematical model via physical modelling or industrial tests.
- A mathematical model of the complete Tundish will be developed to address the effect of different variables on the actual tracking of inclusions and their effective elimination from the steel in the tundish, to an upper slag phase.
- With the water model now constructed, the predicted air suction will be replicated experimentally, and measured.
- Air bubble measurements will be performed with the APS III system in the future water model experiments
- Solutions to the current Ladle Shroud design will be proposed and their impact on the inclusions' formation and elimination based on the presented methodology will be carried out, prior to confirmatory tests in industry.

Bibliography

1. Costa e Silva, A.L.V.d., *Non-metallic inclusions in steels – origin and control*. Journal of Materials Research and Technology, 2018. **7**(3): p. 283-299.
2. Wang, L., H.-G. Lee, and P. Hayes, *Prediction of the Optimum Bubble Size for Inclusion Removal from Molten Steel by Flotation*. ISIJ International, 1996. **36**(1): p. 7-16.
3. Chang, S., et al., *Removal of inclusions using micro-bubble swarms in a four-strand, full-scale, water model tundish*. ISIJ International, 2016. **56**(7): p. 1188-1197.
4. Faraji, M., et al., *Effect of early stages of thermomechanical processing on inclusions in high carbon steel*. Materials science and technology : MST : a publication of the Institute of Metals., 2014. **30**(10): p. 1177-1188.

5. Guthrie, R.I.L., Isac, M., *The Science and Practice of Steelmaking and Steel Processing*, ed. I. Press. 2018.
6. Isa, S., H. Iwai, and B. Tsujino, *Behavior of Oxide Inclusions in Steel during Hot Rolling*. Tetsu-to-Hagane, 1967. **53**(7): p. 870-873.
7. Nakai, Y., et al., *Effects of inclusion size and orientation on rolling contact fatigue crack initiation observed by laminography using ultra-bright synchrotron radiation*. Procedia Structural Integrity, 2016. **2**: p. 3117-3124.
8. Zhang, L. and B.G. Thomas, *State of the Art in Evaluation and Control of Steel Cleanliness*. ISIJ International, 2003. **43**(3): p. 271-291.
9. Sahai, Y., *Tundish Technology for Casting Clean Steel: A Review*. Metallurgical and Materials Transactions B, 2016. **47**(4): p. 2095-2106.
10. Mazumdar, D. and R.I.L. Guthrie, *Physical and mathematical modelling of continuous casting tundish systems*. ISIJ INTERNATIONAL, 1999. **39**(6): p. 524-547.
11. Chattopadhyay, K., M. Isac, and R.I.L. Guthrie, *Physical and mathematical modelling of steelmaking tundish operations: A review of the last decade (1999-2009)*. ISIJ International, 2010. **50**(3): p. 331-348.
12. Mazumdar, D., *Review, Analysis, and Modeling of Continuous Casting Tundish Systems*. steel research international, 2019. **90**(4).
13. Chen, C., et al., *A Model Study of Inclusions Deposition, Macroscopic Transport, and Dynamic Removal at Steel-Slag Interface for Different Tundish Designs*. Metallurgical and Materials Transactions B, 2016. **47**(3): p. 1916-1932.
14. Ni, P., et al., *Non-Metallic Inclusion Behaviors in a New Tundish and SEN Design Using a Swirling Flow during Continuous Casting of Steel*. steel research international, 2017. **88**(3).
15. Cwudziński, A., *Numerical and Physical Modeling of Liquid Steel Flow Structure for One Strand Tundish with Modern System of Argon Injection*. steel research international, 2017. **88**(9).
16. Aguilar-Rodriguez, C.E., et al., *Flow Characterization and Inclusions Removal in a Slab Tundish Equipped with Bottom Argon Gas Feeding*. Metallurgist, 2018. **61**(11-12): p. 1055-1066.

17. Chatterjee, S., D. Li, and K. Chattopadhyay, *Modeling of liquid steel/slag/argon gas multiphase flow during tundish open eye formation in a two-strand Tundish*. Metallurgical and Materials Transactions B: Process Metallurgy and Materials Processing Science, 2018. **49**(2): p. 756-766.
18. Mishra, R. and D. Mazumdar, *Numerical Analysis of Turbulence Inhibitor Toward Inclusion Separation Efficiency in Tundish*. Transactions of the Indian Institute of Metals, 2019. **72**(4): p. 889-898.
19. Neumann, S., et al., *Numerical Simulation of Metal Melt Flow in a One-Strand Tundish Regarding Active Filtration and Reactive Cleaning*. Metallurgical and Materials Transactions. B, Process Metallurgy and Materials Processing Science, 2019. **50**(5).
20. Neumann, S., A. Asad, and R. Schwarze, *Numerical Simulation of an Industrial-Scale Prototypical Steel Melt Tundish Considering Flow Control and Cleaning Strategies*. Advanced Engineering Materials, 2020. **22**(2).
21. de Souza, G., A. Freitas, and R. Tavares, *Physical and mathematical modeling of inclusion behavior in a tundish with gas curtain*. REM - International Engineering Journal, 2020. **73**: p. 531-538.
22. Chang, S., et al., *Modeling Slag Behavior When Using Micro-Bubble Swarms for the Deep Cleaning of Liquid Steel in Tundishes*. steel research international, 2017. **88**(6).
23. Chang, S., et al., *Study on the slag-metal interfacial behavior under the impact of bubbles in different sizes*. Powder Technology, 2021. **387**: p. 125-135.
24. Sheng, D.-Y. and D. Chen, *Comparison of Fluid Flow and Temperature Distribution in a Single-Strand Tundish with Different Flow Control Devices*. Metals, 2021. **11**(5): p. 796.
25. Gupta, V.K., P.K. Jha, and P.K. Jain, *Modeling of Wall Shear Stress Induced Inclusion Transport and Removal in Multi-Strand Tundish*. ISIJ International, 2021. **61**(9): p. 2445-2456.
26. Gupta, A., R. Kumar, and R.K. Singh, *Modeling Study for Understanding of Fluid Dynamics of Vortex Formation in Tundish Operation*. Transactions of the Indian Institute of Metals, 2021. **74**(8): p. 1895-1905.

27. Huang, W., et al., *Modeling of Flow Behaviors in a Swirling Flow Tundish for the Deep Cleaning of Molten Steel*. Steel research international, 2021. **92**(10): p. n/a-n/a.
28. Merder, T., et al., *Evolution of the Numerical Model Describing the Distribution of Non-Metallic Inclusions in the Tundish*. Materials (Basel, Switzerland), 2021. **14**(9).
29. Patil, S.P. and N.N. Viswanathan, *Numerical Investigation of Single-Strand Slab Casting Tundish Flow with Heat Transfer and Inclusion Transport*. Transactions of the Indian Institute of Metals, 2021. **74**(2): p. 369-379.
30. Xu, R., et al., *Investigation on the Effects of Ladle Change Operation and Tundish Cover Powder on Steel Cleanliness in a Continuous Casting Tundish*. Steel research international, 2021. **92**(10): p. n/a-n/a.
31. Zhang, J., et al., *Advances in Ladle shroud as a functional device in tundish metallurgy: A review*. ISIJ International, 2019. **59**(7): p. 1167-1177.
32. Mazumdar, D., P.K. Singh, and R.K. Tiwari, *Shrouded transfer of molten steel from ladle to tundish: Current understanding, mathematical modelling and new insight*. ISIJ International, 2018. **58**(8): p. 1545-1547.
33. Singh, P.K., Tiwari, R., Mazumdar, D., Dutta, A. *Modeling of two phase, gas-liquid flows in a ladle shroud*. in *Int. Cong. on Science and Technology of Steelmaking*. 2018. Milano.
34. Zhang, J., et al., *The Effect of a Dissipative Ladle Shroud on Mixing in Tundish: Mathematical and Experimental Modelling*. High Temperature Materials and Processes, 2018. **37**(1): p. 25-32.
35. Singh, P.K.E., Mazumdar, Dipak, *A Physical Model Study of Two-Phase Gas-Liquid Flows in a Ladle Shroud*. Metallurgical and Materials Transactions. B, Process Metallurgy and Materials Processing Science, 2018. **49**(4).
36. Singh, P.K.E., Mazumdar, Dipak, *Mathematical Modelling of Gas-Liquid, Two-Phase Flows in a Ladle Shroud*. Metallurgical and Materials Transactions. B, Process Metallurgy and Materials Processing Science, 2019. **50**(2).

37. Zhang, H., et al., *Multiphase Flow in a Five-Strand Tundish Using Trumpet Ladle Shroud during Steady-State Casting and Ladle Change-Over*. *steel research international*, 2019. **90**(3): p. 1800497.
38. *ANSYS Fluent Users Guide*. 2021.
39. Wang, L., H.-G. Lee, and P. Hayes, *Modelling of air ingress and pressure distribution in ladle shroud system for continuous casting of steel*. *Steel Research*, 1995. **66**(7): p. 279-286.
40. Iida, T. and R.I.L. Guthrie, *The Thermophysical Properties of Metallic Liquids: Volume 1 — Fundamentals*. 2015, Oxford: Oxford University Press. 384.
41. Poling, B.E., J. O'Connell, and J.M. Prausnitz, *Properties of Gases and Liquids*. 2000, New York, USA, UNITED STATES: McGraw-Hill Professional Publishing.
42. *ANSYS Fluent Theory Guide*. 2021.
43. Guthrie, R. and M. Isac, *In-Situ Sensors for Liquid Metal Quality*, in *Sensors, Sampling, and Simulation for Process Control*. 2011. p. 1-14.